UNIVERSITÀ DI PARMA

UNIVERSITA' DEGLI STUDI DI PARMA

DOTTORATO DI RICERCA IN FISICA

XXXIII CICLO

Towards a solution for the sign problem via complexification: Lefschetz thimbles and Taylor expansions.

Coordinatore:
Prof. Stefano Carretta

Supervisore:
Prof. Francesco Di Renzo

Dottorando:
Dott. Kevin Zambello

Anni 2017/2020

Contents

List of Figures

List of Tables

Introduction

In many branches of physics, from particle and nuclear physics to condensed matter physics, one cannot always find analytical solutions to physical problems. Monte Carlo methods have proved to be an invaluable tool in such cases, as they provide an efficient way to numerically estimate physical quantities that would otherwise remain inaccessible. The case we are most concerned with in this dissertation is that of a quantum field theory formulated on a lattice. On the lattice, observables are expressed as

$$\langle O \rangle = \frac{1}{Z} \int d^n\phi \; O[\{\phi_i\}] \; e^{-S_E[\{\phi_i\}]} \; ,$$

$$\text{with } Z = \int d^n\phi \; e^{-S_E[\{\phi_i\}]} \; .$$

Here ϕ_i is a short-hand notation for the value of the field at the i-th site of the lattice and S_E is the Euclidean action of the system. These expectation values are usually high-dimensional integrals and a direct numerical solution by quadratures would be impractical. In such cases a sensible approach is to evaluate the integrals stochastically, by interpreting the Boltzmannian weight as a probability distribution. Specifically one would like to sample field configurations

$$\{\phi_i\} \propto \frac{e^{-S_E[\{\phi_i\}]}}{Z}$$

and then estimate the value of the integral by the sample mean.

However when S_E is complex-valued we don't have a well-defined (real and positive) probability distribution for importance sampling. This issue is known as the sign problem and unfortunately it affects various theories such as QCD at finite baryon density, QCD with a θ-term or the Hubbard model. In particular the sign problem hinders the exploration by lattice simulations of the T-μ_B phase diagram of QCD, where μ_B is the baryochemical potential. The partition function of QCD has the form

$$Z(\mu_B) = \int [dU_{\mu,x}] \; e^{-S_{YM} \; + \; ln \; det \; M_f(\mu_B)} \; ,$$

where $U_{\mu,x}$ are the gauge variables, S_{YM} is the gauge action and $det \; M_f$ is the fermionic determinant. Due to γ_5-hermitianicity, the fermionic determinant is real at zero (or purely imaginary) chemical potentials, but at finite chemical potentials γ_5-hermitianicity is lost and the fermionic determinant becomes complex-valued. Therefore at finite density the theory has a sign problem.

Some methods have been proposed to work around the sign problem such as reweighting [1, 2], Taylor expansion [3, 4] and analytic continuation from imaginary μ [5, 6]. The idea behind these methods is to restrict oneself to a region of the parameters where there is no sign problem (either zero o purely imaginary chemical

potentials) and then extrapolate information outside that region. A recent review of the state-of-the-art results can be found in ref. [7]. Unfortunately these methods are by no means a complete solution to the sign problem and their application is limited to the region of the phase diagram where $\frac{\mu}{T} \lesssim 1$.

Indeed a general solution for the sign problem is to date still missing and for this reason the search for alternative methods is a very active area of research. Some alternative approaches that are being explored are the density of states [8], the canonical ensemble [9] and the complex Langevin methods [10].

Another approach is the one in which one complexifies the degrees of freedom of the theory and deforms the contour of integration in such a way that the sign problem disappears completely or is alleviated (the reader can find a recent review in ref. [11]). Thimble regularization provides a way to put into practice this idea. Proposed in refs. [12, 13], following the work by Witten [14, 15], the method is an application of the Picard-Lefschetz theory: the original integrals are rewritten as sums of integrals over manifolds (the thimbles) attached to the stationary points of the complexified theory. On each thimble there is no sign problem, because the imaginary part of the action is constant and e^{-iS_I} factorizes out of the integrals.

Calculating the contribution from any single thimble is in principle relatively straightforward, however putting together the contributions from different thimbles is tricky since one has to compute the weight of each contribution and computing these weights has proven to be a challenging task. Of course if only one thimble would contribute to the observables this would pose no problem. However many counter-examples are now known where taking into account more than one thimble is necessary in order to fully capture the content of the theory [37, 41, 42, 45].

In this work we discuss how one can perform multi-thimble calculations and we apply our proposals to two use cases, the one-dimensional Thirring model and (a simple version of) heavy-dense QCD. Performing multi-thimble simulations is a theoretically sound approach when the one-thimble approximation fails. In practice however it is a difficult way to go for theories having a non trivial number of degrees of freedom. This motivated us to explore a different approach which we think is more suited to investigate realistic theories. In this approach one carries out Taylor expansions on thimbles. We show that by making use of a Padé interpolation of multiple Taylor expansions one may exploit the richness of the thimble structure of a theory in order to bypass the need to perform multi-thimble calculations. After having successfully applied this method to the two aforementioned use cases, the Thirring model and heavy-dense QCD, we wanted to see whether a Padé interpolation of Taylor coefficients could be useful also for more traditional calculation methods. We show that this is indeed the case by investigating the QCD phase diagram using Padé approximants and Taylor series calculated at purely imaginary chemical potentials.

The dissertation is composed of five chapters. In the first chapter we give an introduction to the sign problem in the context of lattice field theories. In the second chapter we review the Lefschetz thimble regularization method, we show how one can implement a Monte Carlo integration on thimbles and we discuss some numerical algorithms. In the third chapter we discuss how to collect the contributions from more than one thimble by multi-thimble simulations and, as an application, we apply our proposals to the one-dimensional Thirring model and to (a simple version of) heavy-dense QCD. In the fourth chapter we discuss how to bypass the need to perform multi-thimble simulations using a Padé interpolation of multiple Taylor

expansions, whose coefficients are to be computed via one-thimble simulations. In the fifth chapter we report some results obtained from the study of the QCD phase diagram at imaginary μ by a Padé interpolation of Taylor coefficients.

The results presented in this dissertation are the subject of the following publications and conference proceedings:

- F. Di Renzo and K. Zambello, *Towards Lefschetz thimbles regularization of heavy-dense QCD*, PoS LATTICE2018 (2018) 148 [arXiv:1811.03605 [hep-lat]].
- F. Di Renzo and K. Zambello, *On the Lefschetz thimbles structure of the Thirring model*, PoS LATTICE2019 (2020) 211 [arXiv:1912.11380 [hep-lat]].
- F. Di Renzo, S. Singh and K. Zambello, *One-thimble regularisation of lattice field theories: is it only a dream?*, PoS LATTICE2019 (2020) 105 [arXiv:2002.00472 [hep-lat]].
- C. Schmidt, J. Goswami, G. Nicotra, F. Ziesché, P. Dimopoulos, F. Di Renzo, S. Singh and K. Zambello, *Net-baryon number fluctuations*, Acta Phys. Pol. B Proc. Suppl. 14, 241 (2021) [arXiv:2101.02254 [hep-lat]].
- F. Di Renzo, S. Singh and K. Zambello, *Taylor expansions on Lefschetz thimbles*, Phys. Rev. D 103 (2021) no. 3, 034513 [arXiv:2008.01622 [hep-lat]].
- F. Di Renzo and K. Zambello, *Settling an old story: solution of the Thirring model in thimble regularization*, in preparation.

Moreover another article is currently in preparation, whose subject is the work reported in chapter 5 and carried out in collaboration with the Bielefeld University.

Chapter 1

The sign problem

In this chapter we give an introduction to the sign problem. Firstly we summarize how a quantum field theory can be formulated on a lattice, then we discuss the specific case of QCD and finally we show how a sign problem emerges when studying the thermodynamics of QCD at finite density.

1.1 Quantum field theories on a lattice

For weakly interacting theories the perturbative expansion in the coupling α is a powerful method to calculate physical observables. If we consider for instance the case of QED, where $\alpha \approx \frac{1}{137}$, perturbative calculations of the anomalous magnetic dipole moment of the electron are the most precise prediction in physics, being accurate up to one part in a trillion [16] [17]. However for strongly interacting theories, like Quantum Chromodynamics, the applicability of perturbative techniques is limited. While many calculations can be carried out by perturbative methods, many other require non-perturbative methods. In 1974 Wilson introduced lattice QCD, namely a formulation of QCD on a discrete space-time lattice that preserves gauge invariance [18]. This formulation is one of the possible approaches to investigate QCD non-perturbatively. Some important applications of lattice QCD are the ab-initio determination of hadron masses [19] or the study of the confined-deconfined phase transition [20–24].

But before delving into QCD, let's consider the case of a generic field theory. Lattice regularization starts from the formulation of the theory via Feynman's path integrals. In this formulation the v.e.v. are expressed as a functional integral

$$\langle O \rangle = \frac{\int [D\phi]\ O[\phi]\ e^{iS[\phi]}}{\int [D\phi]\ e^{iS[\phi]}}\ .$$

One switches from the Minkowski space-time to the Euclidean space-time by a Wick rotation $t \mapsto -i\tau$. After the Wick rotation the v.e.v. take the form

$$\langle O \rangle = \frac{\int [D\phi]\ O[\phi]\ e^{-S_E[\phi]}}{\int [D\phi]\ e^{-S_E[\phi]}}\ ,$$

where S_E is the Euclidean action. In the lattice formulation of the theory, the Euclidean space-time is then replaced by an hypercubic $N_s^3 \times N_t$ lattice with spacing a and all the integrals are discretized accordingly,

$$\int [D\phi]\ \bullet \mapsto \int \left(\prod_i d\phi_i \right)\ \bullet\ .$$

The functional integral is now a definite integral in the variables ϕ_i. These are the values of the field at the i-th site of the lattice. In particular, expectation values are now integrals of the form

$$\langle O \rangle = \frac{1}{Z} \int \left(\prod_i d\phi_i \right) O[\{\phi_i\}] \; e^{-S_E(\{\phi_i\})} \; ,$$

where $S_E = \sum_i a^4 \mathcal{L}_E(\{\phi_i\})$ is the discretized Euclidean action and $\mathcal{L}_E$ is the Euclidean Lagrangian density.

The Euclidean action is usually real (but not always, as we shall see later) and such integrals can be calculated by Monte Carlo methods, sampling field configurations from the Boltzmannian weight that we interpret as a probability distribution for importance sampling,

$$\{\phi_i\} \propto \frac{e^{-S_E(\{\phi_i\})}}{Z} \; .$$

Here we also note that the lattice introduces a cut-off for the momenta. This can be seen by looking at the Fourier transform of a function f,

$$\hat{f}(p) = a^4 \sum_x e^{ip_\mu x_\mu} \; f(x) = a^4 \sum_x e^{i(p_\mu + \frac{2\pi}{a})x_\mu} \; f(x) \; .$$

Recalling that on the lattice $x_\mu = a n_\mu$, where n_μ are integer numbers, and that the exponential is 2π-periodic, the last step follows from $i(p_\mu + 2\frac{\pi}{a})x_\mu = ip_\mu x_\mu + 2\pi n_\mu$. Therefore we can see that momenta are restricted to the first Brillouin zone $[-\frac{\pi}{a}, \frac{\pi}{a}]$.

All in all the lattice formulation of a field theory provides a natural regularization for the theory that is numerically tractable by Monte Carlo methods. Moreover gauge symmetries, if any, can be preserved.

As a first example, consider the ϕ^4 theory. The Euclidean Lagrangian density is

$$\mathcal{L}_E = \frac{1}{2} \partial_\mu^E \partial_\mu^E \phi(x) + \frac{m^2}{2} \phi^2(x) + \frac{g}{4!} \phi^4(x) \; .$$

After having discretized the space-time integral as a sum over the sites of the lattice and after replacing the derivatives by central finite differences, we obtain the lattice action

$$S_E = a^4 \sum_i \left(\frac{1}{2} \sum_\mu \left(\frac{\phi(i + a\epsilon_\mu) - \phi(i - a\epsilon_\mu)}{2a} \right)^2 + \frac{m^2}{2} \phi^2(i) + \frac{g}{4!} \phi^4(i) \right) \; .$$

The scalar field ϕ can be rescaled to the dimensionless field $\hat{\phi} = a^2 \phi$. Similarly, one can express the mass as a dimensionless quantity by introducing the mass in lattice units $\hat{m} = am$. In term of $\hat{\phi}$ and $\hat{m}$, the action becomes

$$S_E = \sum_i \left(\frac{1}{2} \sum_\mu \left(\frac{\hat{\phi}(i + a\epsilon_\mu) - \hat{\phi}(i - a\epsilon_\mu)}{2} \right)^2 + \frac{\hat{m}^2}{2} \hat{\phi}^2(i) + \frac{g}{4!} \hat{\phi}^4(i) \right)$$

and the explicit dependence on the lattice spacing a disappears.

The ϕ^4 model is a theory for scalar bosons, but in Nature we mostly have fermions and we would like to put fermions on the lattice as well. The case of fermions is more subtle, even for free fermions. The Euclidean Lagrangian density for free fermions is

$$\mathcal{L}_E^F = \bar{\psi} (\gamma_\mu^E \partial_\mu^E + m) \psi \; ,$$

where γ_μ^E are the Euclidean Dirac matrices. These obey the anti-commutation rule $\{\gamma_\mu^E, \gamma_\nu^E\} = 2\delta_{\mu\nu}$ and can be defined in term of the usual Dirac matrices as $\gamma_4^E = \gamma_0$, $\gamma_{1,2,3}^E = -i\gamma_{1,2,3}$. In the following we will drop the double notation for the Euclidean and Minkowski space-time. We will assume the use of the Euclidean space-time, unless we state otherwise. Proceeding in the same way as we did before, we obtain the naive fermionic lattice action [1]

$$S_F^{naive} = a^4 \sum_i \bar{\psi}(i) \left(\left(\sum_\mu \frac{\gamma_\mu \psi(i + a\epsilon_\mu) - \gamma_\mu \psi(i - a\epsilon_\mu)}{2a} \right) + m\psi(i) \right) .$$

This action can also be recast in matrix notation as

$$S_F^{naive} = \bar{\psi}(i) M_{ij} \psi(j) ,$$

$$\text{with } M_{ij} = a^4 \left(m\delta_{i,j} + \frac{1}{2a} \sum_\mu (\delta_{i,i+\mu} - \delta_{i,i-\mu}) \right) .$$

It can be shown that this action yields the propagator $M^{-1}(q) = (\frac{i}{a}\gamma_\mu \ sin(q_\mu a) + m)^{-1}$. Due to the periodicity of the sine function, this propagator has 16 poles. In other terms the naive lattice action describes 16 particles instead of 1.

This problem, known as fermion doubling, is no accident. It is a consequence of a deep theoretical problem. The Nielsen-Ninomiya no-go theorem [25] states that no bilinear fermionic action on the lattice can at the same time be local, exhibit no doublers, preserve the chiral symmetry and reproduce the correct fermionic action in the continuum limit.

In order to avoid the fermion doubling, Wilson proposed to add the following term to the naive action:

$$\Delta S_F^W = -a^4 \sum_i \frac{ra}{2} \bar{\psi}(i) \Box \psi(i) .$$

Here $0 < r < 1$ is a real parameter that may be taken equal to 1 and $\Box\psi(i) = \sum_\mu \frac{\psi(i+\epsilon_\mu) + \psi(i-\epsilon_\mu) - 2\psi(i)}{2a^2}$ is the discretized Laplacian. The Wilson term vanishes in the continuum limit, therefore the Wilson action still reproduces the correct action in the continuum limit, but it removes the doublers. However the action loses the chiral symmetry at finite a.

In addition to Wilson fermions, other solutions have been proposed, such as Kogut-Susskind (or staggered) fermions [26], twisted-mass fermions [27] and domain-wall fermions [28, 29]. In particular, in the fifth chapter we make use of staggered fermions. In the staggered formulation fermionic fields are redefined as $\psi(x) = \gamma_1^{x_1} \gamma_2^{x_2} \gamma_3^{x_3} \gamma_4^{x_4} \chi(x)$. After such redefinition one has $\bar{\psi}(x) m \psi(x) = \bar{\chi}(x) m \chi(x)$ and $\bar{\psi}(x) \gamma_\mu \psi(x \pm \mu) = \bar{\chi}(x) \eta_\mu(x) \chi(x \pm \mu)$, where we have introduced the staggered phases $\eta_\mu(x) \equiv (-1)^{\sum_{\nu<\mu} x_\nu}$. One obtains the action

$$S_F^{stag} = a^4 \sum_i \bar{\chi}(i) \left(\eta_\mu(i) \frac{U_\mu(i)\chi(x+\mu) - U_\mu^\dagger(i-\mu)\chi(i-\mu)}{2a} + m\chi(i) \right) . \quad (1.1)$$

Having gamma matrices been replaced by staggered phases, this action is diagonal in spinor space. As a consequence, three out of four spinor indices can be dropped

[1] Also in the case of the fermionic action, the lattice spacing a can be eliminated in pretty much the same way we did for the ϕ^4 theory, by rescaling the field ψ to a dimensionless one, $\hat{\psi} = a^{\frac{3}{2}} \psi$.

out and $\chi(x)$ in eq. 1.1 can be regarded as a one-component spinor. It can be shown that this has the effect of reducing the number of doublers from 16 to 4 [30, 31]. This residual *taste* degeneracy can be dealt with by the rooting procedure, in which $detM$ is replaced by $(detM)^{\frac{1}{4}}$. As a side effect of this procedure, however, the action becomes non-local [32].

1.2 The lattice formulation of QCD

Let's now consider Quantum Chromodynamics, which is the quantum field theory of the strong interaction. QCD is a non-abelian gauge theory having the color group $SU(3)$ as the gauge group. In this theory there are N_f fermion fields ψ_f ($f = 1 \dots N_f$) and 8 gluon fields $A^a_\mu(x)$ ($a = 1 \dots 8$) whose dynamics is governed, using the Minkowski space-time, by the Lagrangian

$$\mathcal{L}_{QCD} = \mathcal{L}_F + \mathcal{L}_G = \sum_{f=1\dots N_f} \bar{\psi}_f(i\gamma^\mu D_\mu - m)\psi_f - \frac{1}{4}F^a_{\mu\nu}F^{a\mu\nu}$$

The covariant derivative is $D_\mu = \partial_\mu - igA_\mu$, where $A_\mu(x) = A^a_\mu(x)T_a$ and T_a are the generators of the $SU(3)$ group. The gluon field strength tensor is defined as $F_{\mu\nu} = [D_\mu, D_\nu] \equiv F^a_{\mu\nu}T_a$. The QCD Lagrangian is invariant under the local gauge transformation

$$\begin{cases} \psi(x) \mapsto V(x)\psi(x) \\ \bar{\psi}(x) \mapsto \bar{\psi}(x)V^\dagger(x) \\ A_\mu(x) \mapsto V(x)A_\mu(x)V^\dagger(x) - ig(\partial_\mu V(x))V^\dagger(x) \quad \text{, with } V(x) \in SU(3)\ . \end{cases}$$

After performing a Wick rotation, one obtains the Euclidean Lagrangian

$$\mathcal{L}_{QCD} = \sum_{f=1\dots N_f} \bar{\psi}_f(\gamma_\mu D_\mu + m)\psi_f + \frac{1}{4}F^a_{\mu\nu}F^{a\mu\nu}$$

The lattice action is expressed in term of the infinitesimal parallel transports $U_\mu(x) = e^{-igA_\mu(x)a}$, also called gauge links. Unlike gauge fields, which live in the algebra of $SU(3)$, gauge links live in the color group itself. Pictorially, they can be represented by arrows originating from the site x and pointing to the site $x + a\epsilon_\mu$. Similarly arrows originating from the site x and pointing to the site $x - a\epsilon_\mu$ represent the backward links $U_{-\mu}(x)$. One has that $U_{-\mu}(x) = U^\dagger_\mu(x - a\epsilon_\mu)$. Gauge links transform under local gauge transformations as

$$U_\mu(x) \mapsto V(x)U_\mu(x)V^\dagger(x + a\epsilon_\mu), \text{ with } V(x) \in SU(3)\ . \tag{1.2}$$

In order to understand why gauge links are useful building blocks for the lattice action, let's look at how we can formulate on the lattice the kinetic term of the fermionic action. If for simplicity we consider only 1 flavor and we use the backward finite difference to approximate the derivative, we can write

$$\begin{aligned} \bar{\psi}(x)\gamma_\mu \tfrac{U_\mu(x)\psi(x+a\epsilon_\mu)-\psi(x)}{a} &\approx \bar{\psi}(x)\gamma_\mu \tfrac{(1-igA_\mu(x)a)\psi(x+a\epsilon_\mu)-\psi(x)}{a} \\ &= \bar{\psi}(x)\gamma_\mu \left(\tfrac{\psi(x+a\epsilon_\mu)-\psi(x)}{a} - igA_\mu(x)\psi(x+a\epsilon_\mu)\right) \\ &\overset{a\to 0}{\to} \bar{\psi}(x)\gamma_\mu(\partial_\mu - igA_\mu(x))\psi(x)\ . \end{aligned}$$

After discretizing the covariant derivative we get a term $\bar{\psi}(x)\gamma_\mu U_\mu(x)\psi(x+a\epsilon_\mu)$ that couples spinors at different sites. But thanks to eq. 1.2, this term is manifestly gauge invariant.

By making use of the gauge links, the Wilson fermionic action for QCD is written as $S_F^W = S_F^{naive} + \Delta S_F^W$ with

$$\begin{cases} S_F^{naive} = a^4 \sum_i \bar{\psi}(i) \sum_\mu \left(\frac{\gamma_\mu U_\mu(i)\psi(i+a\epsilon_\mu) - \gamma_\mu U_\mu^\dagger(i-a\epsilon_\mu)\psi(i-a\epsilon_\mu)}{2a} + m\psi(i) \right) \\ \Delta S_F^W = -a^4 \sum_i \frac{ra}{2}\bar{\psi}(i) \sum_\mu \left(\frac{U_\mu(i)\psi(i+a\epsilon^\mu) + U_\mu^\dagger(i-a\epsilon_\mu)\psi(i-a\epsilon_\mu) - 2\psi(i)}{2a^2} \right) . \end{cases}$$

As for the gauge part of the action, the lattice discretization proposed by Wilson reads

$$S_G^W \equiv \beta \sum_{x,\mu>\nu} \left(1 - \frac{1}{3} ReTr U_{\mu\nu}(x) \right) .$$

The lattice gauge action is built from Wilson plaquettes, which are a parallel transports along a square loop,

$$\begin{aligned} U_{\mu\nu}(x) &\equiv U_\mu(x) U_\nu(x+a\epsilon_\mu) U_{-\mu}(x+a\epsilon_\mu+a\epsilon_\nu) U_{-\nu}(x+a\epsilon_\nu) \\ &= U_\mu(x) U_\nu(x+a\epsilon_\mu) U_\mu^\dagger(x+a\epsilon_\nu) U_\nu^\dagger(x) . \end{aligned}$$

From the Wilson gauge action one correctly recovers the gauge action of QCD in the continuum limit for $\beta = \frac{6}{g^2}$. Using eq. 1.2 and the cyclic property of the trace it is also easy to show that S_G^W is gauge invariant.

On the lattice physical quantities are then calculated by computing integrals of the form

$$\begin{aligned} \langle O \rangle &= \frac{1}{Z} \int \left(\prod_{i,\mu} dU_{i,\mu} \right) \left(\prod_i d\bar{\psi}_i \right) \left(\prod_i d\psi_i \right) \; O \; e^{-(S_G^W + S_F^W)} \\ &= \frac{1}{Z} \int \left(\prod_{i,\mu} dU_{i,\mu} \right) \left(\prod_i d\bar{\psi}_i \right) \left(\prod_i d\psi_i \right) \; O \; e^{-S_G^W} \; e^{-\bar{\psi}_n \; M_{nm} \; \psi_m} \\ &= \frac{1}{Z} \int \left(\prod_{i,\mu} dU_{i,\mu} \right) \; O \; det \; M \; e^{-S_G^W} \\ &= \frac{1}{Z} \int \left(\prod_{i,\mu} dU_{i,\mu} \right) \; O \; e^{-S_G^W + log \; det \; M} . \end{aligned}$$

Note that, since fermionic fields are anti-commutating Grassmann variables that cannot easily be represented in the computer, in the last two steps the integration over the fermionic degrees of freedom has been explicitly carried out.

1.3 The sign problem in QCD at finite temperature and density

The thermodynamics of a quantum field theory can be derived from the thermal partition function $Z = Tr[e^{-\beta H}]$. In the path-integral formulation the partition function at a temperature T is expressed by the path integral

$$Z(T) = \int [d\phi] \; e^{-S[\phi]} ,$$

where the Lagrangian density is meant to be integrated up to the Euclidean time $\tau = \beta = \frac{1}{T}$ and one assume periodic and anti-periodic boundary conditions respectively for bosonic and fermionic fields. Specifically the action is

$$S[\phi] = \int_0^\beta d\tau \int_V d^3x \; \mathcal{L}[\phi] .$$

Since we are integrating up to a time $\tau = N_t a = \frac{1}{T}$, the temporal extension of the lattice is fixed by the temperature. The temperature can be changed either by varying N_t while keeping the lattice spacing a fixed or by varying a while keeping N_t fixed.

Thermodynamic quantities, like the energy density ϵ or the pressure P, are obtained from the logarithm of the partition function, i.e.

$$\epsilon = -\frac{1}{V}\frac{\partial\ log(Z)}{\partial\ \beta}\ ,$$

$$P = \frac{1}{\beta}\frac{log(Z)}{V}\ .$$

In the lattice formulation of the quantum field theory, these are integrals that can be calculated numerically by Monte Carlo methods. But one is not only interested in the thermodynamics of a physical system at zero density. In order to study the thermodynamics at finite density, one introduces a chemical potential μ that enters the partition function as $Z(T,\mu) = Tr[e^{-\beta(H-\mu N)}]$. The chemical potential μ couples with the particle number operator $N = \bar{\psi}\gamma_4\psi$. One can embed the chemical potential by adding a μ-dependent term to the fermionic action: for a gauge theory, such as QCD, one obtains

$$S_F = \int d\tau \int d^3x\ \bar{\psi}(\gamma^\mu D_\mu + m)\psi + \mu\bar{\psi}\gamma_4\psi\ .$$

On the lattice we might be tempted to naively discretize the new term so that for the Wilson action, for instance, we get

$$S_F^W \mapsto S_F^W + \mu a^4 \sum_i \bar{\psi}(i)\gamma_4\psi(i)\ .$$

Unfortunately this simple solution results in having a divergent energy in the continuum limit,

$$\epsilon(\mu) \propto \left(\frac{\mu}{a}\right)^2\ .$$

This happens because, as it was realized in ref. [33], the chemical potential acts as the temporal component of a constant imaginary gauge field. On the lattice the chemical potential must enter in term of links, like the gluon fields. In particular, one has to multiply the forward and backward temporal links by $e^{a\mu}$ and $e^{-a\mu}$, obtaining

$$\begin{cases} S_F^{naive} = a^4 \sum_i \bar{\psi}(i) \sum_\mu \left(\frac{\gamma_\mu e^{\delta_{\mu 4} a\mu} U_\mu(i)\psi(i+a\epsilon_\mu) - \gamma_\mu e^{-\delta_{\mu 4} a\mu} U_\mu^\dagger(i-a\epsilon_\mu)\psi(i-a\epsilon_\mu)}{2a} + m\psi(i) \right) \\ \Delta S_F^W = -a^4 \sum_i \frac{ra}{2}\bar{\psi}(i) \sum_\mu \left(\frac{e^{\delta_{\mu 4} a\mu} U_\mu(i)\psi(i+a\epsilon^\mu) + e^{-\delta_{\mu 4} a\mu} U_\mu^\dagger(i-a\epsilon_\mu)\psi(i-a\epsilon_\mu) - 2\psi(i)}{2a^2} \right)\ . \end{cases}$$

At zero density, the fermionic matrix is γ_5-hermitian, that is $\gamma_5 M \gamma_5 = M^\dagger$. But as soon as we add a finite chemical potential, γ_5-hermitianicity is lost. In place of γ_5-hermitianicity one finds that the fermionic matrix obeys the relation

$$\gamma_5 M(\mu)\gamma_5 = M^\dagger(-\mu)\ .$$

Since $(det\ \gamma_5)^2 = 1$, from this relation it follows the fermionic determinant is such that

$$det\ M(\mu) = \overline{det\ M(-\mu)}\ .$$

Therefore the fermionic determinant is complex at finite density and this prevents us from interpreting e^{-S} as a probability distribution for importance sampling. This issue is known as the sign problem and it currently hinders the investigation of the T-μ phase diagram of QCD.

1.4 From QCD to simpler models affected by the sign problem

In this section we introduce two QED and QCD inspired models that provide simpler but physically motivated settings in which one can test novel techniques and ideas proposed to tame the sign problem.

1.4.1 One-dimensional $U(1)$-links model and the Thirring model

First we consider a one-dimensional $U(1)$-links model governed by the action

$$S = S_G + S_F = \beta \sum_{t=1}^{L} \left(1 - \frac{1}{2}(U_t + U_t^\dagger)\right) + \sum_{t,t'} \bar{\chi}_t M_{t,t'} \chi_{t'}\ .$$

$$\text{with } M_{t,t'} = \frac{1}{2}(U_t e^{\mu} \delta_{t+1,t'} - U_{t'}^\dagger e^{-\mu} \delta_{t-1,t'}) + m\delta_{t,t'}$$

Here $U_t = e^{i\phi_t} \in U(1)$ are the link variables, $\beta = \frac{1}{e^2}$ is the inverse coupling constant and M is the fermionic matrix. A chemical potential μ has been added following the prescription introduced by ref. [33] and discussed in the previous section. One can derive the following expression for the fermionic determinant [34]

$$detM = \frac{1}{2^L}\left(e^{L\mu}\prod_t U_t + e^{-L\mu}\prod_t U_t^\dagger + (m + \sqrt{1+m^2})^L + (m - \sqrt{1+m^2})^L\right)\ .$$

This is a simple model that resembles lattice QED in one dimension. It's easy to see that the fermionic determinant satisfies the relation $det\ M(\mu) = \overline{det\ M(-\mu)}$. Then in presence of a finite chemical potential the model, like lattice QCD, is affected by a sign problem originating from the fermionic determinant. After integrating out the fermionic degrees of freedom, the partition function can be written as

$$Z = \int dU_t\ e^{-\beta \sum_{t=1}^{L}\left(1 - \frac{1}{2}(U_t + U_t^\dagger)\right) + log\ det\ M}\ .$$

If we now rework the partition function in terms of the phase of the link variables ($\int dU_t \mapsto \int \frac{d\phi_t}{2\pi}$), we obtain

$$Z = \int \frac{d\phi}{2\pi}\ e^{-\beta \sum_{t=1}^{L}(1 - cos(\phi_t)) + log\ det\ M}\ .$$

Moreover from the relation $(m+\sqrt{1+m^2})^L + (m-\sqrt{1+m^2})^L = 2cosh(L\ asinh(m))$ (valid when L is even), one has

$$detM = \frac{1}{2^{L-1}}(cosh(L\mu + i\sum_t \phi_t) + cosh(L\ asinh(m)))\ .$$

This form makes it manifest that the model is equivalent to the one-dimensional Thirring model [42–45, 50].

1.4.2 Heavy-dense QCD as a 3d effective theory

We now consider an effective theory for heavy quarks having Polyakov loops as the only degrees of freedom. We sketch here the general ideas behind its derivation, referring the reader to refs. [47–49] for a detailed calculation. The effective action of the theory is obtained by integrating the QCD partition function over the spatial gauge links, i.e.

$$Z = \int dU_4 \; dU_i \; detM \; e^{\frac{\beta}{6}\sum_p (TrU_p + TrU_p^\dagger)} = \int dU_4 \; e^{-S_{eff}} \; ,$$

$$\text{with } \; -S_{eff} = log\left(\int dU_i \; detM \; e^{\frac{\beta}{6}\sum_p (TrU_p + TrU_p^\dagger)} \right) \; .$$

In order to perform the integration one employs a combined strong coupling and hopping parameter expansion.

As a first step consider the pure gauge theory. The integration over the spatial links is carried out by making use of the character expansion in the strong coupling limit ($\beta \to 0$),

$$-S_{eff} = log\left(\int dU_i \; \prod_p (1 + \sum_r d_r a_r(\beta) \chi_r(U_p)) \right)$$

The sum extends over the irreducible representations of the $SU(3)$ group, d_r and $a_r(\beta)$ are respectively the dimension and the expansion coefficient of the r-th representation, while $\chi_r(U_p) = TrU_p^{(r)}$ is the character of U_p in the given representation. The leading contribution in β is obtained by neglecting the purely spatial plaquettes. The integration is performed by applying the integration rule $\int dU \chi_r(XU)\chi_s(U^{-1}Y) = \frac{\delta_{rs}}{d_r}\chi_r(XY)$. Notice that this rule forces all terms to be made out of plaquettes living in the same representation. After integrating one is left with only loops winding around the temporal direction. Considering only the leading contribution, which comes from the fundamental representation, one has

$$\begin{aligned} -S_{eff} &= \sum_{<x,y>} log\left(1 + \lambda(TrW_x TrW_y^\dagger + TrW_x^\dagger TrW_y)\right) \\ &= \sum_{<x,y>} \lambda(TrW_x TrW_y^\dagger + TrW_x^\dagger TrW_y) + O(u^{2N_t}) \; , \end{aligned}$$

where $\lambda = u^{N_t}$ and $u = \alpha_f(\beta) \approx \frac{\beta}{18}$. Higher order corrections to the gauge coupling λ can be calculated in order to take into account the contribution from the purely spatial plaquettes.

As a second step consider the hopping parameter expansion in the strong coupling limit ($\beta = 0$). Let's recall that the hopping matrix H is defined from the fermionic matrix M by $M = 1 - kH$, where the hopping parameter $k = \frac{1}{2ma+8}$ is a suitable expansion parameter in the limit of heavy quarks. By separating the contributions from the temporal and spatial links, the fermionic determinant can be expressed as $det\; M = det(1-kH) = det(1-T-S) = det(1-T)\; det(1-\frac{S}{1-T}) \equiv det\; Q_{stat}\; det\; Q_{kin}$. The leading contribution in k is given by the static determinant $det\; Q_{stat}$, thus it

is obtained neglecting the so-called spatial hops S. The explicit expression for the static determinant is

$$det\ Q_{stat} = det(1 - ke^{a\mu}(1+\gamma_4)U_4(x)\delta_{x,y-\hat{4}} - ke^{-a\mu}(1-\gamma_4)U_4^\dagger(x-\hat{4})\delta_{x,y+\hat{4}})\ .$$

This can be worked out as

$$det\ Q_{stat} = \prod_x (1 + h_1 TrW_x + h_1^2 TrW_x^\dagger + h_1^3)^2 (1 + \bar{h}_1 TrW_x^\dagger + \bar{h}_1^2 TrW_x + \bar{h}_1^3)^2\ ,$$

where we have introduced the quarks and antiquarks couplings $h_1 = (2k)^{N_t}(e^{a\mu})^{N_t}$, $\bar{h}_1 = (2k)^{N_t}(e^{a\mu})^{-N_t}$. The effective fermionic action then reads

$$-S_{eff} = 2\sum_x log(1+h_1 TrW_x + h_1^2 TrW_x^\dagger + h_1^3) + 2\sum_x log(1+\bar{h}_1 TrW_x^\dagger + \bar{h}_1^2 TrW_x + \bar{h}_1^3).$$

At leading order this is given in terms of independent, decoupled Polyakov loops. When taking into account the kinetic determinant to go beyond leading order, higher order terms appear coupling Polyakov loops originating at different spatial sites of the lattice.

Hitherto we have considered the strong coupling and the hopping parameter expansions separately. The final step consists in taking the two expansions together. This involves the introduction of mixing terms that appear as corrections to the quarks and antiquarks couplings.

All in all one obtains an effective theory of QCD that greatly simplifies the original theory, since the number of degrees of freedom is significantly reduced. On the other hand the region in the (μ, m, T)-space that one has access to is limited by the number of terms in the expansion that one is able to take into account in the numerical calculations. The theory is still affected by a sign problem, since the effective fermionic action is complex. Later we will be concerned with the cold-dense limit and in this regime the theory is further simplified. In the cold, large N_t limit one has $\lambda = u^{N_t} \to 0$ and the gauge action can, de facto, be neglected. In the dense limit one has $(e^{a\mu})^{-N_t} = e^{-\frac{\mu}{T}} \ll 1$ and the $\bar{h}_1$ contributions can be neglected as well.

Chapter 2

Lefschetz thimble regularization

In this chapter we introduce the thimble regularization method and we show how one can perform a Monte Carlo integration on thimbles by importance sampling. We also discuss some numerical algorithms used in our actual code.

2.1 Thimble regularization

The Picard-Lefschetz theory provides an alternative and elegant way to tackle the sign problem, by complexifying the integrals and deforming the domain of integration. Specifically the new domain of integration is a combination of manifolds, the thimbles, where the sign problem is absent (apart from a residual phase problem coming from the orientation of the thimbles with respect to the embedding manifold). The method was originally proposed independently by refs. [12] and [13], following the work carried out by Witten in refs. [14, 15].

In order to illustrate the method, let's start from the following integral,

$$I = \int_{\mathcal{C}} d^n x \; e^{-S(x)} \; ,$$

with $\mathcal{C} = \mathbb{R}^n$. This integral can be seen as the prototype for the partition function of a lattice field theory governed by the complex-valued action $S(x)$. We now complexify the degrees of freedom,

$$x = (x_1, \ldots, x_n) \mapsto z = (z_1 = x_1 + iy_1, \ldots, z_n = x_n + iy_n) \; ,$$

and we analytically continue the action $S(x) \mapsto S(z)$. We assume that the action $S = S(z) = S(x, y) = S_R + iS_I$ is holomorphic, hence the Cauchy-Riemann equations hold,

$$\begin{cases} \partial_{x_i} S_R = \partial_{y_i} S_I \\ \partial_{y_i} S_R = -\partial_{x_i} S_I \; . \end{cases}$$

Or equivalently,

$$\begin{cases} \partial_{\overline{z}_i} S = 0 \\ \partial_{z_i} \overline{S} = 0 \; . \end{cases}$$

Now we define the set of the critical points of the theory,

$$\Sigma = \{ z_\sigma \text{ s.t. } \partial_{z_i} S|_{z_\sigma} = 0 \} \; ,$$

and we assume that all critical points are non-degenerate, hence the Hessian of the action is non-singular (it has a non-zero determinant) at each critical point,

$$det\ H(S, z_\sigma) \neq 0 \text{ , with } H(S, z_\sigma)_{ij} = \partial_{z_i}\partial_{z_j} S(z)|_{z_\sigma} \ .$$

Attached to each critical point we can define a manifold, the stable thimble $\mathcal{J}_\sigma$, as the union of the solutions of the steepest-ascent equations

$$\begin{cases} \frac{dz_i}{dt} = \frac{\partial \overline{S}}{\partial \overline{z}_i} \\ \frac{d\overline{z}_i}{dt} = \frac{\partial S}{\partial z_i} \end{cases} \text{ , with } z(-\infty) = z_\sigma \ .$$

The solutions of the SA equations are characterized by a non-decreasing S_R (hence the name steepest-ascent) and a constant S_I. Indeed using the chain rule for the flow time derivative one finds that

$$\begin{cases} \frac{d}{dt} S_R = \frac{1}{2}\frac{d}{dt}(S + \overline{S}) = \frac{1}{2}\sum_i (\frac{dz_i}{dt}\frac{\partial S}{\partial z_i} + \frac{d\overline{z}_i}{dt}\frac{\partial \overline{S}}{\partial \overline{z}_i}) = |\nabla S|^2 \geq 0 \\ \frac{d}{dt} S_I = \frac{1}{2i}\frac{d}{dt}(S - \overline{S}) = \frac{1}{2i}\sum_i (\frac{dz_i}{dt}\frac{\partial S}{\partial z_i} - \frac{d\overline{z}_i}{dt}\frac{\partial \overline{S}}{\partial \overline{z}_i}) = 0 \ . \end{cases}$$

Then one can rewrite the original integral as

$$I = \sum_{\sigma \in \Sigma} n_\sigma \int_{\mathcal{J}_\sigma} d^n z\ e^{-S(z)} = \sum_{\sigma \in \Sigma} n_\sigma e^{-iS_I(z_\sigma)} \int_{\mathcal{J}_\sigma} d^n z\ e^{-S_R(z)} \ .$$

The original integral has been decomposed into a sum of integrals over thimbles. The imaginary part of S factorizes out of the integrals, since it is constant on each thimble, and the convergence of the integrals is ensured by S_R being non-decreasing. The term e^{-S_R} is real and positive, thus it can be interpreted as a probability distribution for importance sampling. The intersection numbers $n_\sigma = \langle \mathcal{K}_\sigma, \mathcal{C} \rangle$ are integer numbers that count the number of intersections between the original domain $\mathcal{C}$ and the unstable thimble $\mathcal{K}_\sigma$, where the latter is defined as the union of solutions of the steepest descent equations

$$\begin{cases} \frac{dz_i}{dt} = -\overline{\frac{\partial S}{\partial z_i}} \\ \frac{d\overline{z}_i}{dt} = -\frac{\partial S}{\partial z_i} \end{cases} \text{ , with } z(-\infty) = z_\sigma \ .$$

The solutions of the SD equations, like the solutions of the SA equations, have a constant imaginary part of the action. But in this case the real part of the action is non-increasing. As a consequence any critical point having a real part of the action lower than the minimum action on the original domain, $S^{min} = min_{z \in \mathcal{C}} Re(S(z))$, has necessarily a zero intersection number and does not contribute to the decomposition. The reason is that the associated unstable thimble can never intersect the original domain. On the other hand critical points that lie on the original domain do necessarily contribute to the decomposition, since their unstable thimbles intersect the original domain (precisely at the critical points).

Let's now expand the action quadratically at a given critical point,

$$S(z) = S(z_\sigma) + \frac{1}{2}(z - z_\sigma)^T H(S, z_\sigma)(z - z_\sigma) \ .$$

The Hessian at z_σ is an $n \times n$ complex symmetric, non-singular matrix. By Takagi's theorem there exist n orthonormal Takagi vectors $v^{(i)}$,

$$\sum_h v_h^{(i)} \overline{v}_h^{(j)} = \delta_{ij} \ ,$$

and n non-negative Takagi values λ_i (which we assume to be non-zero) that satisfy the generalized eigenvalue equation,

$$Hv^{(i)} = \lambda_i \overline{v}^{(i)} \ . \tag{2.1}$$

The Takagi vectors $v^{(i)}$ form, together with $w^{(i)} = iv^{(i)}$, a basis of $\mathbb{C}^n$ in the sense that any element of $\mathbb{C}^n$ can be written as a linear combination with real coefficients of the $v^{(i)}$ and $w^{(i)}$. If we parametrize the displacement from z_σ in terms of this basis, we find that

$$S(z) = S(z_\sigma) + \frac{1}{2}\lambda_i(\eta_i + i\xi_i)^2 \ , \text{ with } z - z_\sigma = \eta_i v^{(i)} + \xi_i w^{(i)} \ .$$

For the real and imaginary part of the action,

$$\begin{cases} S_R(z) = S_R(z_\sigma) + \frac{1}{2}\sum_i \lambda_i \eta_i^2 - \frac{1}{2}\sum_i \lambda_1 \xi_i^2 \\ S_I(z) = S_I(z_\sigma) + \sum_i \lambda_i \eta_i \xi_i \ . \end{cases}$$

The vectors $\{v^{(i)}\}$ identify n independent directions along which the the real part of the action is non-decreasing and the imaginary part of the action is constant. They are a basis for the tangent space of the thimble $\mathcal{J}_\sigma$ at the critical point. Therefore the thimble $\mathcal{J}_\sigma$ has real dimension n, the same as the original domain $\mathcal{C}$. The $\{w^{(i)}\}$ are instead a basis for the tangent space of the unstable thimble $\mathcal{K}_\sigma$ at the critical point.

At this point it is important to note that the integration measure on the thimble is $dz^n = det\ J\ d\eta^n$, where $det\ J$ is the Jacobian of the transformation between z and η. Because of this Jacobian the integrands in the thimble decomposition are not strictly real, thus we are left with a residual sign problem. However this usually turns out to be a mild sign problem that can be dealt with by reweighting.

The Jacobian is $det\ J = det\ V = |det\ V|\ e^{i\omega}$, where V is the matrix having as columns the basis vectors for the tangent space and $e^{i\omega}$ is the residual phase. By solving the Takagi problem, eq. 2.1, it is quite easy to find a basis for the tangent space at the critical points, the Takagi vectors. These however do not constitute a basis for the tangent space at any other point. Nonetheless, from a variational argument we can think of a way to compute a basis at any point z on the thimble starting from the basis at the critical point. First we expand

$$\delta = \sum_i \left(\delta z_i \partial_{z_i} + \delta \overline{z}_i \partial_{\overline{z}_i}\right) \ ,$$

then we find out how the infinitesimal displacement δz varies along the flow

$$\frac{d}{dt}(\delta z_j) = \delta\left(\frac{d}{dt} z_j\right) = \delta\left(\frac{\partial \overline{S}}{\partial \overline{z}_j}\right) =$$

$$= \sum_i \left(\delta z_i \partial_{z_i} + \delta \overline{z}_i \partial_{\overline{z}_i}\right) \frac{\partial \overline{S}}{\partial \overline{z}_j} = \sum_i \delta \overline{z}_i \frac{\partial^2 \overline{S}}{\partial \overline{z}_i \partial \overline{z}_j} \ .$$

Therefore in order to determine a basis (hence $det\ J$) at a generic point z on the thimble we may transport along the flow each Takagi vector $V^{(h)}$ by integrating the parallel transport equations,

$$\frac{dV_j^{(h)}}{dt} = \sum_i \overline{V}_i^{(h)} \overline{\partial^2_{z_i z_j} S} \ .$$

Since these equations depend on the Hessian of the action, which in turn depends on the fields, they have to be integrated simultaneously with the SA equations.

The Takagi vectors, which are the initial conditions for the parallel transport equations, are found by solving the Takagi problem. However, rather than solving the Takagi problem directly, it is easier to diagonalize the expanded Hessian

$$\tilde{H} = \begin{pmatrix} Re(H) & -Im(H) \\ -Im(H) & -Re(H) \end{pmatrix} .$$

The expanded Hessian $\tilde{H}$ is a $2n \times 2n$ block matrix made out of the real and imaginary parts of the Hessian at the critical point H. Being a real symmetric matrix, $\tilde{H}$ is diagonalizable. Moreover, if we define the matrix

$$J = \begin{pmatrix} 0 & -\mathbb{I} \\ \mathbb{I} & 0 \end{pmatrix}$$

one has that $J^{-1}\tilde{H}J = -\tilde{H}$ with $J^{-1} = J^T$, $J^2 = \mathbb{I}$. It follows that the matrices $\tilde{H}$ and $-\tilde{H}$ are similar matrices and therefore if λ is an eigenvalue of $\tilde{H}$, $-\lambda$ is also an eigenvalue. Assuming all eigenvalues are non-zero, the expanded Hessian has n positive eigenvalues λ_i and n negative eigenvalues $-\lambda_i$. The positive eigenvalues are the Takagi values. Indeed if λ is a positive eigenvalue of $\tilde{H}$ and

$$w = \begin{pmatrix} v_R \\ v_I \end{pmatrix}$$

is the eigenvector associated to λ, one has that

$$\begin{cases} Re(H)v_R - Im(H)v_I = \lambda v_R \\ -Im(H)v_R - Re(H)v_I = \lambda v_I \end{cases} .$$

Then $v = v_R + iv_I$ is the Takagi vector associated to the Takagi value λ, since

$$Hv = (Re(H) + iIm(H))(v_R + iv_I) =$$

$$= Re(H)v_R - Im(H)v_I + i(Im(H)v_R + Re(H)v_I) =$$

$$= \lambda v_R - i\lambda v_I = \lambda \overline{v} .$$

2.2 Thimble regularization for $SU(N)$ gauge theories

The thimble decomposition discussed in the previous section can be applied, after suitably adapting the formalism, to the case of a $SU(N)$ gauge theory. In a $SU(N)$ gauge theory the gauge variables are links, these are matrices $U \in SU(N)$. Any $SU(N)$ matrix can be constructed from a linear combination of the generators of the group,

$$U = e^{ix_a T^a} \in SU(N) \ , \ \{x_a\}_{a=1\ldots N^2-1} \in \mathbb{R} .$$

The generators T^a are traceless Hermitian matrices normalized as $\{T^a, T^b\} = \frac{1}{2}\delta^{ab}$. Their commutators are determined by the structure constant of the group f^{abc}, $[T^a, T^b] = if^{abc}T^c$.

For a $SU(N)$ gauge theory complexifying the degrees of freedom means complexifying the real parameters x_a, thus we have

$$U = e^{ix_a T^a} \in SU(N) \mapsto U = e^{iz_a T^a} = e^{i(x_a + iy_a)T^a} \in SL(N, \mathbb{C}) .$$

After complexification we obtain matrices which are members of the special linear group $SL(N,\mathbb{C})$. These are $N \times N$ complex matrices with determinant 1. In some cases, such as heavy-dense QCD, the action is expressed in terms of U and $U^\dagger$. One must stress that by complexifying the dagger of U one does not yield the dagger of the complexified U. Instead one has

$$U^\dagger = e^{-ix_a T^a} \in SU(N) \mapsto e^{-i(x_a + iy_a)T^a} = U^{-1} \in SL(N,\mathbb{C}) \ ,$$

therefore in such theories occurrences of $U^\dagger$ must be replaced by U^{-1}.

To apply the thimble regularization method we need a proper definition for the derivatives and in this case the natural definition is based on the Lie derivative,

$$\begin{cases} \nabla^a f(U) = \lim_{\alpha\to 0} \frac{1}{\alpha}(f(e^{i\alpha T^a}U) - f(U)) = \frac{\partial}{\partial\alpha} f(e^{i\alpha T^a}U)|_{\alpha=0} \\ \overline{\nabla}^a f(\overline{U}) = \lim_{\alpha\to 0} \frac{1}{\alpha}(f(e^{i\alpha T^a}\overline{U}) - f(\overline{U})) = \frac{\partial}{\partial\alpha} f(e^{i\alpha T^a}\overline{U})|_{\alpha=0} \\ \nabla^a f(\overline{U}) = 0 \ , \ \overline{\nabla}^a f(U) = 0 \ . \end{cases}$$

Starting from the Lie derivative we can introduce the derivatives for a function f of the gauge fields,

$$\nabla^a_{\mu,x} f(\{U_{\nu,y}\}) = \frac{\partial}{\partial\alpha} f\left(e^{i\alpha T^a} U_{\mu,x}, \{U_{\nu,y}\}_{(\nu,y)\neq(\mu,x)}\right)|_{\alpha=0} \ .$$

Due to the non-abelian nature of the $SU(N)$ gauge group, these derivatives do not commute. Instead they obey the commutation rules

$$[\nabla^a_{\mu,x}, \nabla^b_{\nu,y}] = -f^{abc}\delta_{\mu\nu}\delta_{xy}\nabla^c_{\mu,x} \ ,$$

$$[\overline{\nabla}^a_{\mu,x}, \overline{\nabla}^b_{\nu,y}] = -f^{abc}\delta_{\mu\nu}\delta_{xy}\overline{\nabla}^c_{\mu,x} \ ,$$

$$[\overline{\nabla}^a_{\mu,x}\nabla^b_{\nu,y}] = 0 \ .$$

Having introduced a definition for the derivatives, we can now define the critical points of the theory as

$$\Sigma = \{p_\sigma \text{ s.t. } \nabla^a_{\mu,x} S|_{p_\sigma} = 0\} \ .$$

The Hessian $\nabla^a_{\mu,x}\nabla^b_{\nu,y}S$ is still symmetric at the critical points, since at the critical points the commutator of the derivatives vanishes thanks to the condition of vanishing gradient.

Before writing down the steepest ascent equations we also need an expression for the flow time derivative of a function $f(U) : SL(N,\mathbb{C}) \mapsto \mathbb{C}$ along a curve $U(t)$ generated by an infinitesimal displacement $\alpha_a T^a dt$ [35],

$$\frac{dU(t)}{dt} = (i\alpha_a T^a)U(t) \ ,$$

$$U(t+dt) = e^{i\alpha_a T^a dt}U(t) \ ,$$

$$\frac{d}{dt}f(U(t)) = \alpha_a \ \nabla^a f(U(t)) \ . \tag{2.2}$$

Now we can formulate the SA equations as

$$\frac{dU_{\mu,x}(t)}{dt} = (iT^a\overline{\nabla}^a_{\mu,x}\overline{S}[U(t)])U_{\mu,x}(t) \ , \tag{2.3}$$

$$U_{\mu,x}(t+dt) = e^{iT^a \overline{\nabla}^a_{\mu,x} \overline{S}[U(t)]dt} U_{\mu,x}(t) \ .$$

From eq. 2.2 it follows that the chain rule for $\frac{d}{dt}$ along the flow is

$$\frac{d}{dt} = \overline{\nabla}^a_{x,\mu} \overline{S} \ \nabla^a_{x,\mu} + \nabla^a_{x,\mu} S \ \overline{\nabla}^a_{x,\mu}$$

and it can be shown that the solutions of eqs. 2.3 have indeed a constant imaginary part of the action and a non-decreasing real part of the action,

$$\begin{cases} \frac{d}{dt} S_R = \frac{1}{2} \frac{d}{dt} (S + \overline{S}) = \frac{1}{2} \sum_{\mu,x,a} (\overline{\nabla}^a_{x,\mu} \overline{S} \ \nabla^a_{x,\mu} S + \nabla^a_{x,\mu} S \ \overline{\nabla}^a_{x,\mu} \overline{S}) = |\nabla S|^2 \geq 0 \\ \frac{d}{dt} S_I = \frac{1}{2i} \frac{d}{dt} (S - \overline{S}) = \frac{1}{2i} \sum_{\mu,x,a} (\overline{\nabla}^a_{x,\mu} \overline{S} \ \nabla^a_{x,\mu} S - \nabla^a_{x,\mu} S \ \overline{\nabla}^a_{x,\mu} \overline{S}) = 0 \ . \end{cases}$$

Likewise, we can define the steepest descent equations

$$\frac{dU_{\mu,x}(t)}{dt} = -(iT^a \overline{\nabla}^a_{\mu,x} \overline{S}[U(t)]) U_{\mu,x}(t) \ ,$$

$$U_{\mu,x}(t+dt) = e^{-idtT^a \overline{\nabla}^a_{\mu,x} \overline{S}[U(t)]} U_{\mu,x}(t) \ .$$

whose solutions have non-increasing S_R and constant S_I.

Finally we can derive the parallel transport equations, using a variational argument as we did in the case of a scalar theory. We start from the variation, which in this case lives in the $su(N)$ algebra,

$$U_{\mu,x} \mapsto e^{i\delta z_{\mu,x,a} T^a} U_{\mu,x}$$

$$\delta = \sum_{\mu,x,a} (\delta z_{\mu,x,a} \nabla^a_{\mu,x} + \overline{\delta z}_{\mu,x,a} \overline{\nabla}^a_{\mu,x}) \ ,$$

and we determine the flow time variation of $\delta z_{\mu,x,c}$ by equating

$$\left(\frac{d}{dt} \delta U_{\mu,x} \right) U^{-1}_{\mu,x} = \left(\delta \frac{d}{dt} U_{\mu,x} \right) U^{-1}_{\mu,x} \ .$$

The left hand side is

$$\left(\frac{d}{dt} \delta U_{\mu,x} \right) U^{-1}_{\mu,x} = \left(\frac{d}{dt} \sum_{\nu,y,c} (\delta z_{\nu,y,c} \nabla^c_{\nu,y} + \overline{\delta z}_{\nu,y,c} \overline{\nabla}^c_{\nu,y}) U_{\mu,x} \right) U^{-1}_{\mu,x} =$$

$$= \left(\frac{d}{dt} \sum_c \delta z_{\mu,x,c} i T^c U_{\mu,x} \right) U^{-1}_{\mu,x} = \left(\sum_c iT^c \left(\frac{d(\delta z_{\mu,x,c})}{dt} U_{\mu,x} + \delta z_{\mu,x,c} \frac{dU_{\mu,x}}{dt} \right) \right) U^{-1}_{\mu,x} =$$

$$= \sum_c iT^c \frac{d(\delta z_{\mu,x,c})}{dt} - \sum_c \delta z_{\mu,x,c} \sum_a T^c T^a \overline{\nabla}^a_{\mu,x} \overline{S}.$$

Assuming that the action is holomorphic ($\nabla^a_{\mu,x} \overline{S} = 0$), we find for the right hand side

$$\left(\delta \frac{d}{dt} U_{\mu,x} \right) U^{-1}_{\mu,x} = \left(\sum_{\nu,y,a} \left(\delta z_{\nu,y,a} \nabla^a_{\nu,y} + \overline{\delta z}_{\nu,y,a} \overline{\nabla}^a_{\nu,y} \right) \left(\sum_c iT^c \overline{\nabla}^c_{\mu,x} \overline{S} U_{\mu,x} \right) \right) U^{-1}_{\mu,x} =$$

$$= \left(\sum_c iT^c \left(\sum_a \delta z_{\mu,x,a} \overline{\nabla}^c_{\mu,x} \overline{S} iT^a U_{\mu,x} + \sum_{a,\nu,y} \overline{\delta z}_{\nu,y,a} \overline{\nabla}^a_{\nu,y} \overline{\nabla}^c_{\mu,x} \overline{S} U_{\mu,x} \right) \right) U^{-1}_{\mu,x} =$$

$$= \left(\sum_c iT^c \left(\sum_a \delta z_{\mu,x,a} \overline{\nabla}^c_{\mu,x} \overline{S} iT^a + \sum_{a,\nu,y} \overline{\delta z}_{\nu,y,a} \overline{\nabla}^a_{\nu,y} \overline{\nabla}^c_{\mu,x} \overline{S} \right) \right) =$$

$$= -\sum_c \delta z_{\mu,x,c} \sum_a T^a T^c \overline{\nabla}^a_{\mu,x} \overline{S} + \sum_c iT^c \sum_{a,\nu,y} \overline{\delta z}_{\nu,y,a} \overline{\nabla}^a_{\nu,y} \overline{\nabla}^c_{\mu,x} \overline{S} \ .$$

By collecting the expressions that we have just derived for the left and right hand sides, we obtain

$$\sum_c iT^c \frac{d(\delta z_{\mu,x,c})}{dt} = \sum_c \sum_a \delta z_{\mu,x,c} [T^c, T^a] \overline{\nabla}^a_{\mu,x} \overline{S} + \sum_c iT^c \sum_{a,\nu,y} \overline{\delta z}_{\nu,y,a} \overline{\nabla}^a_{\nu,y} \overline{\nabla}^c_{\mu,x} \overline{S} =$$

$$= \sum_a \sum_b \delta z_{\mu,x,a} [T^a, T^b] \overline{\nabla}^b_{\mu,x} \overline{S} + \sum_c iT^c \sum_{a,\nu,y} \overline{\delta z}_{\nu,y,a} \overline{\nabla}^a_{\nu,y} \overline{\nabla}^c_{\mu,x} \overline{S} =$$

$$= \sum_a \sum_b \sum_c \delta z_{\mu,x,a} i f^{abc} T^c \overline{\nabla}^b_{\mu,x} \overline{S} + \sum_c iT^c \sum_{a,\nu,y} \overline{\delta z}_{\nu,y,a} \overline{\nabla}^a_{\nu,y} \overline{\nabla}^c_{\mu,x} \overline{S} \ .$$

Therefore we have

$$\frac{d(\delta z_{\mu,x,c})}{dt} = \sum_{a,b} \delta z_{\mu,x,a} [T^a, T^b] \overline{\nabla}^b_{\mu,x} \overline{S} + \sum_{a,\nu,y} \overline{\delta z}_{\nu,y,a} \overline{\nabla}^a_{\nu,y} \overline{\nabla}^c_{\mu,x} \overline{S} \ ,$$

and the parallel transport equations for the basis vectors are

$$\frac{dV_{\mu,x,c}}{dt} = \sum_{\nu,y,a} \overline{\nabla}^a_{y,\nu} \overline{\nabla}^c_{x,\mu} \overline{SV}_{\nu,y,a} + \sum_{a,b} f^{abc} \overline{\nabla}^b_{x,\mu} \overline{S} V_{\mu,x,a} \ .$$

2.3 Monte Carlo integration

From what we have seen in the previous sections, under suitable conditions the partition function of a lattice field theory can be decomposed as

$$Z = \sum_{\sigma \in \Sigma} n_\sigma e^{-iS_I(z_\sigma)} \int_{\mathcal{J}_\sigma} d^n z \ e^{-S_R} = \sum_{\sigma \in \Sigma} n_\sigma e^{-iS_I(z_\sigma)} \int_{\mathcal{J}_\sigma} d^n \delta y \ e^{i\omega_\sigma} \ e^{-S_{eff}} \ ,$$

where $d^n z = det\ V\ d^n \delta y = |det\ V|\ e^{i\omega_\sigma} d^n \delta y$. Here the δy_h are the infinitesimal displacements along the local basis vectors $V^{(h)}(z)$ of the tangent space, $e^{i\omega_\sigma}$ is the residual phase and the modulus $|det\ V|$ has been included in the definition of the effective action

$$S_{eff} = S_R - log(|det\ V|) \ .$$

In the same way we can decompose the observables of the theory as

$$\langle O \rangle = \frac{1}{Z} \sum_{\sigma \in \Sigma} n_\sigma e^{-iS_I(z_\sigma)} \int_{\mathcal{J}_\sigma} d^n \delta y \ O \ e^{i\omega_\sigma} \ e^{-S_{eff}}$$

$$= \frac{\sum_{\sigma\in\Sigma} n_\sigma e^{-iS_I(z_\sigma)} \int_{\mathcal{J}_\sigma} d^n\delta y \; O \; e^{i\omega_\sigma} \; e^{-S_{eff}}}{\sum_{\sigma\in\Sigma} n_\sigma e^{-iS_I(z_\sigma)} \int_{\mathcal{J}_\sigma} d^n\delta y \; e^{i\omega_\sigma} \; e^{-S_{eff}}} \; .$$

The residual sign problem stemming from the residual phase $e^{i\omega_\sigma}$ can be dealt with by reweighting,

$$\langle O \rangle = \frac{\sum_\sigma n_\sigma e^{-iS_I(z_\sigma)} Z_\sigma \langle O e^{i\omega_\sigma} \rangle_\sigma}{\sum_\sigma n_\sigma e^{-iS_I(z_\sigma)} Z_\sigma \langle e^{i\omega_\sigma} \rangle_\sigma} \; ,$$

after having discretized the expectation value $\langle f \rangle_\sigma$ on the single thimble $\mathcal{J}_\sigma$ as

$$\langle f \rangle_\sigma = \int_{\mathcal{J}_\sigma} d^n\delta y \; f \; \frac{e^{-S_{eff}}}{Z_\sigma} \text{ with}$$

$$Z_\sigma = \int_{\mathcal{J}_\sigma} d^n\delta y \; e^{-S_{eff}} \; .$$

So far we have been able to recast a generic observable $\langle O \rangle$ into a sum of contributions coming from individual thimbles. Since these contributions are expectation values with respect to a well-defined (real, positive and normalized) probability distribution $\frac{e^{-S_{eff}}}{Z_\sigma}$, nothing prevents their calculation by importance sampling. These contributions are weighted by the Z_σ, whose calculation is a tricky task that we will discuss in the next chapter. For now we want to think of a way to compute $\langle f \rangle_\sigma$ by importance sampling (and this is all we need in the particular case where only one thimble gives a relevant contribution to the decomposition).

We make use of the natural identification of a point of the thimble by the initial direction $\hat{n}$ on the tangent space of the SA path and the integration time t,

$$z \in \mathcal{J}_\sigma \leftrightarrow (\hat{n}, t) \; .$$

The direction $\hat{n}$ is specified by n components $\{n_i\}$ and it is normalized so that $\sum_i n_i^2 = \mathcal{R}$. Somehow we want to rewrite the integrals, such as the partition function

$$Z_\sigma = \int_{\mathcal{J}_\sigma} d^n\delta y \; e^{-S_{eff}} = \int_{\mathcal{J}_\sigma} \prod_i d\delta y_i \; e^{-S_{eff}} \; , \tag{2.4}$$

in terms of the integration measure $\mathcal{D}\hat{n} \; dt = \prod_i dn_i \delta(|\hat{n}|^2 - \mathcal{R}) \; dt$. We can do that by employing a Fadeev-Popov trick, that is we rewrite 1 as

$$1 = \Delta(\hat{n}, t) \int \prod_i dn_i \delta(|\hat{n}|^2 - \mathcal{R}) \int dt \prod_i \delta(\delta y_i - \delta y_i(\hat{n}, t)) \; . \tag{2.5}$$

Then by inserting eq. 2.5 into eq. 2.4 we obtain

$$Z_\sigma = \int_{\mathcal{J}_\sigma} \prod_i d\delta y_i \; \Delta(\hat{n}, t) \int \prod_i dn_i \delta(|\hat{n}|^2 - \mathcal{R}) \int dt \prod_i \delta(\delta y_i - \delta y_i(\hat{n}, t)) \; e^{-S_{eff}}$$

$$= \int \prod_i dn_i \delta(|\hat{n}|^2 - \mathcal{R}) \int dt \; \Delta(\hat{n}, t) \; e^{-S_{eff}} = \int \mathcal{D}\hat{n} \; Z^\sigma_{\hat{n}} \; .$$

An expression for $\Delta(\hat{n}, t)$ was worked out in ref. [37], that is $\Delta(\hat{n}, t) = 2 \sum_i \lambda_i n_i^2$. Using this expression we can finally rewrite the partition function as an integral, over all possible SA paths, of the *partial* partition function

$$Z^\sigma_{\hat{n}} = \int dt \; \Delta(\hat{n}, t) \; e^{-S_{eff}} = 2 \sum_i \lambda_i n_i^2 \int dt \; e^{-S_{eff}}$$

In the same way we can rewrite the expectation value $\langle f \rangle_\sigma$ as

$$\langle f \rangle_\sigma = \int_{\mathcal{J}_\sigma} d^n\delta y \ f \ \frac{e^{-S_{eff}}}{Z_\sigma} = \int \mathcal{D}\hat{n} \frac{f_{\hat{n}}}{Z_\sigma} \text{ with}$$

$$f_{\hat{n}} = 2 \sum_i \lambda_i n_i^2 \int dt \ f \ e^{-S_{eff}} \ .$$

Finally if we further rewrite

$$\langle f \rangle_\sigma = \int \mathcal{D}\hat{n} \frac{f_{\hat{n}}}{Z_\sigma} = \int \mathcal{D}\hat{n} \frac{f_{\hat{n}}}{Z^\sigma_{\hat{n}}} \frac{Z_{\hat{n}}}{Z_\sigma} \ ,$$

we can see how the expectation value can be calculated by importance sampling, by sampling entire SA paths $\hat{n} \propto Z^\sigma_{\hat{n}}$ and estimating $\langle f \rangle_\sigma$ as the sample mean of $\frac{f_{\hat{n}}}{Z^\sigma_{\hat{n}}}$. In order to sample paths $\propto Z^\sigma_{\hat{n}}$ one could for instance extract proposals $\hat{n}'$ uniformly from the hypersphere of radius $\mathcal{R}$ and accept such proposals with probability

$$P_{acc}(\hat{n}' \leftarrow \hat{n}) = min\left(1, \frac{Z^\sigma_{\hat{n}'}}{Z^\sigma_{\hat{n}}}\right) \ .$$

2.4 Numerical algorithms

The recipe for our Monte Carlo sampling of a thimbles is to sample steepest ascent paths $\hat{n} \propto \frac{Z_{\hat{n}}}{Z_\sigma}$ and estimate an expectation value $\langle f \rangle_\sigma$ as the sample mean $\langle f \rangle_\sigma \approx \frac{1}{N} \sum_{\hat{n}} \frac{f_{\hat{n}}}{Z_{\hat{n}}}$. The quantities $Z_{\hat{n}}$ and $f_{\hat{n}}$ are the flow time integrals

$$Z_{\hat{n}} = 2 \sum_i \lambda_i n_i^2 \int dt \ e^{-S_R(\hat{n},t) + log(|det \ V(\hat{n},t)|)}$$

$$f_{\hat{n}} = 2 \sum_i \lambda_i n_i^2 \int dt \ f \ e^{-S_R(\hat{n},t) + log(|det \ V(\hat{n},t)|)} \ .$$

These integrals can be integrated numerically. Close to the critical point the action S can be approximated by the Gaussian action $S(\eta) = S(z_\sigma) + \frac{1}{2} \sum_i \lambda_i \eta_i^2$ and the solutions of the steepest ascent (and the parallel transport) equations are given by

$$\begin{cases} z = z_\sigma + n_i e^{\lambda_i t} v^{(i)} \\ V^{(h)} = v^{(h)} e^{\lambda_h t} \ . \end{cases}$$

By choosing a reference time $t = t_0 \ll 0$, these expressions yield a reasonable initial condition for the numerical integration. Since the real part of the action is monotonic in flow time, it is possible to integrate in action.

We have that

$$\frac{dS_R}{dt} = \frac{1}{2}(S + \overline{S}) = |\nabla S|^2 \mapsto dt = dS_R \ |\nabla S|^{-2} \ .$$

Therefore after the change of variable the integrals become

$$Z_{\hat{n}} = 2 \sum_i \lambda_i n_i^2 \int_{S_R(z_\sigma)}^{\infty} ds \ |\nabla S|^{-2} \ e^{-s + log(|det \ V(s)|)}$$

$$f_{\hat{n}} = 2\sum_i \lambda_i n_i^2 \int_{S_R(z_\sigma)}^{\infty} ds\ f\ |\nabla S|^{-2}\ e^{-s+log(|det\ V(s)|)}\ .$$

Moreover after a second change of variable $s = S_R \mapsto s = S_R - S_R(z_\sigma)$ we get

$$Z_{\hat{n}} = 2\sum_i \lambda_i n_i^2 e^{-S_R(z_\sigma)} \int_0^{\infty} ds\ |\nabla S|^{-2}\ e^{-s+log(|det\ V(s)|)}$$

$$f_{\hat{n}} = 2\sum_i \lambda_i n_i^2 e^{-S_R(z_\sigma)} \int_0^{\infty} ds\ f\ |\nabla S|^{-2}\ e^{-s+log(|det\ V(s)|)}\ .$$

In this form, these integrals can be calculated by making use of the Gauss-Legendre quadrature

$$\int_0^{\infty} f(x)e^{-x}dx = \sum w_i f(x_i)\ .$$

Here $\{x_i\}$ and $\{w_i\}$ are the quadrature points and their associated weights and an algorithm for their computation is available in ref. [38]. Note that integrating by quadrature we have to compute the determinant $det\ V(s)$ only at the quadrature points.

In order to compute the integrals, we need to integrate both SA and PT equations. After the change of variable these are

$$\frac{dz_i}{ds} = |\nabla S|^{-2}\ \frac{\partial \overline{S}}{\partial \overline{z}_i}$$

$$\frac{dV_j^{(h)}}{ds} = |\nabla S|^{-2}\ \sum_i \overline{V}_i^{(h)} \overline{\partial^2_{z_i z_j} S}\ .$$

For the integration of the field and the basis it is convenient to use an RK-embedded integration scheme. An RK-embedded integrator is composed by two Runge-Kutta integrators of order p and $p+1$ that share the intermediate steps. This allows to estimate with small additional effort the integration error ϵ as the difference between the $(p+1)$-th order and the p-th order integration steps. This estimate can in turn be used to automatically adjust the step size so as to keep the integration error under control: if the error is lower than some threshold tol the $(p+1)$-th order solution is accepted, otherwise it is rejected. The integration step is adjusted anyway in order to target the desired accuracy,

$$dt \mapsto dt\ \left|\frac{tol}{\epsilon}\right|^{\frac{1}{p+1}}\ .$$

If the error is larger than the tolerance, the step size is decreased in order to improve the accuracy. On the other hand if the error is lower than the tolerance, the step size is increased in order not to have more than the desired accuracy. In practice, in order to avoid adjustments for the integration step that are too extreme, one adjusts the step with something like

$$dt \mapsto 0.9\ dt\ min\left(max\left(\left(\frac{tol}{err}\right)^{\frac{1}{p+1}}, 0.25\right), 2\right),$$

so as to increase the step by at most a factor 2 or decrease it by at most a factor $\frac{1}{4}$.

Specifically, for the Thirring model we have used the Bogacki-Shampine integrator [39]. Given a differential equation $\frac{dz}{dt} = f(z,t)$, the steps for the Bogacki-Shampine integrator are

$$\begin{cases} z_n(t_n) \\ z_{i1}(t_{i1} = t_n + \frac{1}{2}\ dt) = z_n + \frac{1}{2} f(z_n, t_n)\ dt \\ z_{i2}(t_{i2} = t_n + \frac{3}{4}\ dt) = z_n + \frac{3}{4} f(z_n, t_n)\ dt \\ z^{(3)}_{n+1}(t_{n+1}) = z_n + (\frac{2}{9} f(z_n, t_n) + \frac{1}{3} f(z_{i1}, t_{i1}) + \frac{4}{9} f(z_{i2}, t_{i2}))\ dt \\ z^{(2)}_{n+1}(t_{n+1}) = z_n + (\frac{7}{24} f(z_n, t_n) + \frac{1}{4} f(z_{i1}, t_{i1}) + \frac{1}{3} f(z_{i2}, t_{i2}) + \frac{1}{8} f(z^{(3)}_{n+1}, t_{n+1}))\ dt\ . \end{cases}$$

The error estimate is given by the difference between the third and second order integration steps,

$$\epsilon = \left| z^{(3)}_{n+1} - z^{(2)}_{n+1} \right| =$$

$$= \left| -\frac{5}{72} f(z_n, t_n) + \frac{1}{12} f(z_{i1}, t_{i1}) + \frac{1}{9} f(z_{i2}, t_{i2}) - \frac{1}{8} f(z^{(3)}_{n+1}, t_{n+1}) \right|\ dt\ .$$

Actually, since we are integrating in action, we can also directly formulate an estimate for the error for the third order integration step in terms of the action,

$$\epsilon = \left| S(z^{(3)}_{n+1}) - (S(z_n) + ds)) \right|\ .$$

This error is only telling us whether we are correctly integrating the fields, it knows nothing about the basis. Nonetheless we can check a-posteriori that we are correctly integrating the basis by verifying the consistency relation proposed in ref. [13]. Since the gradient of the action lives in the tangent space, it can be written as a linear combination of the local basis of the tangent space,

$$\overline{\nabla_z S} = \sum_h \alpha_h V^{(h)}(t)\ .$$

Here the coefficients α_h are constant, while the local basis vectors $V^{(h)}(t)$ change along the flow. We can determine the α_h by computing the gradient close to the critical point, where the Gaussian (quadratic) approximation of the action holds:

$$\sum_h \alpha_h V^{(h)}(t_0 \ll 0) = \overline{\nabla_z S}(t_0 \ll 0) =$$

$$= \overline{\nabla_z (S(z_\sigma) + \frac{1}{2}(z(t_0) - z_\sigma)^T H (z(t_0) - z_\sigma))} =$$

$$= \overline{\nabla_z (\frac{1}{2}(z(t_0) - z_\sigma)^T H (z(t_0) - z_\sigma))} =$$

$$= \overline{H(z(t_0) - z_\sigma)} = \overline{H(n_i e^{\lambda_i t_0} v^{(i)})} =$$

$$= (\lambda_i n_i e^{\lambda_i t_0} v^{(i)}) = (\lambda_i n_i V^{(i)}(t_0))\ .$$

We find that $\alpha_h = \lambda_h n_i$, hence we have

$$\overline{\nabla_z S} = \sum_h n_h \lambda_h V^{(h)}(t)$$

and we can check whether we are correctly integrating the basis by verifying that the following norm vanishes

$$\epsilon_k = \frac{|\overline{\nabla_z S} - \sum_h n_h \lambda_h V^{(h)}(t)|}{|\overline{\nabla_z S}|} \ .$$

Before discussing the mechanism for choosing the Metropolis proposals, a caveat is due that some additional care is needed when choosing an integrator for a $SU(N)$ gauge theory. In the lattice formulation of a $SU(N)$ gauge theory, the gauge fields live in the gauge group $SU(N)$ and one needs an integration scheme that preserves tha structure of that group. In addition to that, since the fields have to be integrated simultaneously with the basis, an higher order integration scheme for the gauge fields should make use of intermediate steps that can be shared with the integration scheme for the basis. For heavy-dense QCD we made use of the 4-th order Runge-Kutta method from ref. [40]. For a given differential equation $\frac{dU}{dt} = iZ(U)\ U(t)$, with $U \in SU(3)$ and $Z \in su(3)$, the steps for the integrator are

$$\begin{cases} U_n \\ U_{i1} = e^{\frac{1}{2} iZ(U_n)dt}\ U_n \\ U_{i2} = e^{\frac{1}{2} iZ(U_{i1})dt + \frac{1}{8}[iZ(U_n)dt, iZ(U_{i1})dt]}\ U_n \\ U_{i3} = e^{iZ(U_{i2})dt}\ U_n \\ U_{n+1} = e^{\frac{1}{6} iZ(U_n)dt + \frac{1}{3} iZ(U_{i1})dt + \frac{1}{3} iZ(U_{i2})dt + \frac{1}{6} iZ(U_{i3})dt - \frac{1}{12}[iZ(U_n)dt, iZ(U_{i3})dt]}\ U_n \ . \end{cases}$$

Let's now discuss how we choose and accept/reject Metropolis proposals for the next configuration in our Markov chain. In our Monte Carlo, the proposals are the initial directions $\hat{n}$ of the SA paths and we want to sample these directions $\propto \frac{Z_{\hat{n}}}{Z_\sigma}$. Starting from a given configuration $\hat{n}$ we generate a new proposal by performing N consecutive rotations within the subspaces defined by randomly picked directions. That is we extract two random integers $i \neq j$ and we perform a rotation within the subspace defined by (n_i, n_j), then we extract a random integer $h \neq j$ and we perform a rotation within the subspace defined by (n_j, n_h) and so on. The process continues until we have performed a given number N of rotations. Each rotation is done as follows. If (n_i, n_j) are the directions chosen for the rotation and $C = n_i^2 + n_j^2$, we can parametrize n_i and n_j as

$$\begin{cases} n_i = \sqrt{C}\ sin(\phi) \\ n_j = \sqrt{C}\ cos(\phi) \ . \end{cases}$$

Then we uniformly extract $\phi_0 \in [-\alpha, \alpha]$ and we update the proposal for the new configuration as

$$\begin{cases} n'_i = \sqrt{C}\ sin(\phi + \phi_0) \\ n'_j = \sqrt{C}\ cos(\phi + \phi_0) \\ n'_h = n_h \ (\text{for } h \neq i, j\ ) \end{cases} \ .$$

The final proposal is accepted with probability

$$P_{acc}(\hat{n}' \leftarrow \hat{n}) = min\left(1, \frac{Z^\sigma_{\hat{n}'}}{Z^\sigma_{\hat{n}}}\right) \ .$$

The parameter α has to be tuned so as to reach a good compromise between avoiding a low acceptance rate (for large α) and a high autocorrelation time (for low α).

2.5 Reflection symmetry

In this section we examine a useful property, discussed in ref. [36], of the multi-thimble decomposition due to the presence of a reflection symmetry. Consider the partition function of a physical system

$$Z = \int_{\mathbb{R}^n} d^n x \; e^{-S(x)} \; .$$

This must be real even if in presence of a sign problem the action S is complex valued. A way to ensure the reality of the partition function is the presence of a reflection symmetry. That is, there exists a real operator $L : x_i \mapsto x'_i = L_{ij} x_j$ acting on the fields such that $L = L^T = L^{-1}$ and for which $\overline{S(x)} = S(Lx)$. Now consider the multi-thimble decomposition for Z,

$$Z = \sum_\sigma n_\sigma \int_{\mathcal{J}_\sigma} d^n z \; e^{-S(z)} \; .$$

Here the fields x have been complexified, $x \mapsto z = x + iy$. We can extend the linear map L to an antilinear map $K : z_i \mapsto z'_i = L_{ij} \overline{z}_j$ that satisfies

$$\overline{S(z)} = S(Kz) = S(L\overline{z}) \; .$$

From this property it follows that the contributions in the multi-thimble decomposition occur in complex conjugate pairs.

In order to see that firstly we have to show that the SA equations are covariant under the antilinear map K, in other words if $z(t)$ is a solution of the SA eqs. then $Kz(t)$ is also a solution of the SA eqs. Indeed one has that

$$\frac{d(Kz)_i}{dt} = \frac{d(L\overline{z})_i}{dt} = \frac{dL_{ij}\overline{z}_j}{dt} = L_{ij}\frac{d\overline{z}_j}{dt} = L_{ij}\frac{\partial S(z)}{\partial z_j} = L_{ij}\frac{\partial \overline{S(Kz)}}{\partial z_j} \; .$$

Then from the chain rule

$$\partial_{z_j} = \sum_k \partial_{z_j}(Kz)_k \; \partial_{(Kz)_k} + \partial_{z_j}(\overline{Kz})_k \; \partial_{(\overline{Kz})_k} = L_{jk}\partial_{(\overline{Kz})_k}$$

one obtains

$$\frac{d(Kz)_i}{dt} = \sum_{j,k} L_{ij}L_{jk}\frac{\partial \overline{S(Kz)}}{\partial (\overline{Kz})_k} = \sum_k \delta_{ik}\frac{\partial \overline{S(Kz)}}{\partial (\overline{Kz})_k} = \frac{\partial \overline{S(Kz)}}{\partial (\overline{Kz})_i} \; .$$

We conclude that if z_σ is a critical point and $\mathcal{J}_\sigma$ is its associated thimble, then Kz_σ is also a critical point and the associated thimble $\mathcal{J}^K_\sigma$ will appear in the multi-thimble decomposition together with $\mathcal{J}_\sigma$. Moreover one has that

$$\int_{\mathcal{J}_\sigma} d^n z \; e^{-S(z)} = \int_{\mathcal{J}_\sigma} d^n z \; e^{-\overline{S(L\overline{z})}} = \overline{\int_{\mathcal{J}_\sigma} d^n (L^{-1}L\overline{z}) \; e^{-S(L\overline{z})}} = \pm \overline{\int_{\mathcal{J}^K_\sigma} d^n z' \; e^{-S(z')}} \; ,$$

where in the last step we made the change of variable $z' = L\overline{z}$. The sign depends on whether the antilinear map changes the orientation of the thimble. Depending on the sign, conjugate thimbles give contributions that are either purely imaginary (and in this case their intersection number must be zero to ensure the reality of the partition function) or purely real.

2.6 Gaussian approximation

Consider the quadratic expansion for the action S,

$$S(\eta) = S(z_\sigma) + \frac{1}{2}\sum_i \lambda_i \eta_i^2 \text{ , where } \eta = z - z_\sigma \ .$$

In the Gaussian approximation of the theory, in which one assumes the quadratic expansion for S holds everywhere, the partition function Z can be calculated analytically:

$$Z = \sum_\sigma Z_\sigma = \sum_\sigma e^{-iS_I(z_\sigma)} \int_{\mathcal{J}_\sigma} d^n z \ e^{-S_R(z)} \approx$$

$$\approx \sum_\sigma e^{-iS_I(z_\sigma)} e^{i\omega_\sigma} e^{-S_R(z_\sigma)} \int_{\mathbb{R}^n} d^n\eta e^{-\frac{1}{2}\sum \lambda_i \eta_i^2} =$$

$$= (2\pi)^{\frac{n}{2}} \sum_\sigma n_\sigma e^{-iS_I(z_\sigma)} e^{i\omega_\sigma} \frac{e^{-S_R(z_\sigma)}}{\sqrt{\prod_i \lambda_i}} =$$

$$= (2\pi)^{\frac{n}{2}} \sum_\sigma n_\sigma e^{-iS_I(z_\sigma)} e^{i\omega_\sigma} \frac{e^{-S_R(z_\sigma)}}{\sqrt{det\Lambda_\sigma}} \ ,$$

where we have defined the Takagi determinant $det\Lambda_\sigma$ as the determinant of the matrix having the Takagi values on its diagonal, $(\Lambda_\sigma)_{i,j} = \delta_{ij}\lambda_i$. One can see that in this approximation the dominant thimble is the one having the highest $e^{-S_R(z_\sigma)}$ hence the lowest real part of action (or more precisely the one having the highest $\frac{e^{-S_R(z_\sigma)}}{\sqrt{\prod_i \lambda_i}}$).

One might also be interested in knowing what the partial partition function looks like in the same approximation. Let's recall that the partial partition function is defined as

$$Z_{\hat{n}} = 2\sum_i \lambda_i n_i^2 \int dt \ e^{-S_R(\hat{n},t) + log(|det \ V(\hat{n},t)|)} \ ,$$

where $V^{(h)}(\hat{n},t)$ is the parallel transported basis. In the Gaussian approximation,

$$\begin{cases} z = z_\sigma + n_i e^{\lambda_i t} v^{(i)} \\ V^{(h)} = v^{(h)} e^{\lambda_h t} \ . \end{cases}$$

Then in terms of $\hat{n}$ and t the action S and the determinant $det \ V$ are given by

$$S(t) = S(z_\sigma) + \frac{1}{2}\sum_i \lambda_i (n_i e^{\lambda_i t})^2 \ ,$$

$$det \ V(\hat{n},t) = e^{\sum_h \lambda_h t} e^{i\omega} \ .$$

Therefore one finds the following expression for the partial partition function in the Gaussian approximation,

$$Z_{\hat{n}} \approx 2\sum_i \lambda_i n_i^2 \int dt e^{-\sum_i \lambda_i t - \frac{1}{2}\sum_i \lambda_i n_i^2 e^{2\lambda_i t}} \ .$$

Chapter 3

Multi-thimble simulations

When thimble regularization was first proposed, the single thimble dominance hypothesis was formulated. From semiclassical arguments the fundamental thimble (the one attached to the critical point having the minimum real part of the action) is the thimble giving the most relevant contribution and its contribution is expected to be further enhanced in the infinite volume limit. Moreover the regularization on the fundamental thimble has the same symmetries and the same perturbative expansion as the original theory. Therefore it was conjectured that the fundamental thimble would dominate in the thermodynamic limit and the one-thimble approximation would be enough to correctly capture the physical content of the full theory. During the last few years various counter-examples have been found where the one-thimble approximation is not a valid approximation, even in the thermodynamic limit. Therefore the contributions from the thimbles other than the fundamental one cannot, in general, be neglected. In this chapter we discuss the techniques we have developed for multi-thimble simulations. In particular we propose two methods to calculate the weight of the thimbles and we consider two use cases as an example of their application.

3.1 Multi-thimble simulations

The thimble decomposition of an observable $\langle O \rangle$ is given by

$$\langle O \rangle = \frac{\sum_\sigma n_\sigma e^{-iS_I(z_\sigma)} Z_\sigma \langle O e^{i\omega_\sigma} \rangle_\sigma}{\sum_\sigma n_\sigma e^{-iS_I(z_\sigma)} Z_\sigma \langle e^{i\omega_\sigma} \rangle_\sigma} \ ,$$

where $\langle \bullet \rangle_\sigma$ are the contributions from the individual thimbles $\mathcal{J}_\sigma$ and they are weighted by the weights Z_σ. In the previous chapter we described a method for calculating these contributions by importance sampling. This is all we need when only one thimble enters the decomposition, so that the decomposition reduces to

$$\langle O \rangle = \frac{\langle O e^{i\omega_\sigma} \rangle_\sigma}{\langle e^{i\omega_\sigma} \rangle_\sigma} \ .$$

Unfortunately taking into account only the dominant thimble is not enough, as we now know from various counter-examples, from the ϕ^4 toy model [37], to one-dimensional QCD [41] and the Thirring model [42, 45]. In such cases one has to think of a way to compute the relative weights of the thimble in order to properly collect their contributions. We have explored two possible ways to accomplish this

task (though other ways are being explored as well, see ref. [46], but see also the next chapter).

The first method takes advantage of the Gaussian approximation of the theory. While computing the partition function Z_σ itself is expected to be an hard task, computing the partition function in the Gaussian approximation, Z_σ^G, is relatively straightforward. Thus one could compute the Gaussian weights Z_σ^G first and then compute their corrections $\frac{Z_\sigma}{Z_\sigma^G}$. The corrections can be estimated by importance sampling,

$$\frac{Z_\sigma^G}{Z_\sigma} = \frac{1}{Z_\sigma}\int D\hat{n} Z_{\hat{n}}^G = \int D\hat{n}\frac{Z_{\hat{n}}^G}{Z_{\hat{n}}}\frac{Z_{\hat{n}}}{Z_\sigma} = \left\langle \frac{Z_{\hat{n}}^G}{Z_{\hat{n}}} \right\rangle_{\hat{n}} .$$

If the theory resembles the Gaussian theory to a certain extent, one expects computing these corrections to be an easier task than calculating the Z_σ themselves.

The second method follows a more pragmatic approach. The idea is the following: consider for the sake of simplicity the case where two thimbles are needed, then

$$\langle O \rangle = \frac{n_0 e^{-iS_I(z_0)} Z_0 \langle O e^{i\omega_0}\rangle_0 + n_1 e^{-iS_I(z_1)} Z_1 \langle O e^{i\omega_1}\rangle_1}{n_0 e^{-iS_I(z_0)} Z_0 \langle O e^{i\omega_0}\rangle_0 + n_1 e^{-iS_I(z_1)} Z_1 \langle O e^{i\omega_1}\rangle_1} .$$

After dividing both the numerator and the denominator by $n_0 e^{-iS_I(z_0)} Z_0$ we obtain

$$\langle O \rangle = \frac{\langle O e^{i\omega_0}\rangle_0 + \alpha \langle O e^{i\omega_1}\rangle_1}{\langle e^{i\omega_0}\rangle_0 + \alpha \langle e^{i\omega_1}\rangle_1} .$$

where $\alpha = \frac{n_1 e^{-iS_I(z_1)} Z_1}{n_0 e^{-iS_I(z_0)} Z_0}$. The parameter α does not depend on the observable, therefore we can fix it from some observable $\tilde{O}$ known by some other mean (i.e. from the analytical solution or from an experimental measurement) and then use it to calculate any other observable.

In the following part of this chapter we show how by using these methods one is able to perform multi-thimble simulations. We consider two use cases as examples. All in all multi-thimble simulations are found to be of limited usefulness, in term of the number of degrees of freedom that one can reach while mantaining a reasonable signal-to-noise ratio. Therefore in the next chapter we will discuss a more promising approach.

3.2 Case study 1 - heavy-dense QCD

As a first application, we consider a simple version of heavy-dense QCD, i.e. we come back to the 3d-effective theory introduced in sec. 1.4.2. The partition function, up to leading order in β and next-to-leading order in k, is written as [47–49]

$$Z = \int [dU_0]\, e^{-S_{eff}[U]} ,$$

where the effective action S_{eff} is given by

$$S_{eff} = S_G + S_F = -\lambda \sum_{<x,y>} \left(TrW_x TrW_y^\dagger + TrW_x^\dagger TrW_y \right)$$

$$-2\sum_x ln\left(1 + h_1 TrW_x + h_1^2 TrW_x^\dagger + h_1^3\right)$$

$$+2h_2 \sum_{<x,y>} \left(\frac{h_1 TrW_x + 2h_1^2 TrW_x^\dagger + 3h_1^3}{1 + h_1 TrW_x + h_1^2 TrW_x^\dagger + h_1^3} \right) \left(\frac{h_1 TrW_y + 2h_1^2 TrW_y^\dagger + 3h_1^3}{1 + h_1 TrW_y + h_1^2 TrW_y^\dagger + h_1^3} \right) , \tag{3.1}$$

and the parameters λ, h_1 and h_2 are defined as

$$\lambda = u^{N_t} e^{N_t \cdot (4u^4 + 12u^5 + \ldots)} ,$$

$$h_1 = (2ke^\mu)^{N_t} [1 + 6k^2 N_t \frac{u - u^{N_t}}{1 - u} + \ldots] ,$$

$$h_2 = k^2 \frac{N_t}{3} [1 + 2\frac{u - u^{N_t}}{1 - u} + \ldots] .$$

Here $u \approx \frac{\beta}{18}$, k is the hopping parameter and $TrW_x = Tr \prod_{t=1}^{N_t} U_0(x,t)$ is the Polyakov loop at the spatial site $x = \vec{x}$. The sums $\sum_x$ and $\sum_{<x,y>}$ extend respectively over the N_{sites} spatial sites of the lattice and over nearest neighbors. At finite chemical potential the fermion action is complex and this model is affected by a genuine sign problem. In ref. [48] this theory has been used to the study the nuclear liquid-gas transition by complex Langevin simulations. In this chapter we plan to approach the theory by the Lefschetz thimble method.

3.2.1 Critical points

In the region of parameters we are interested in ($\beta \approx 6.0$, $N_t \approx 100$, following ref. [48]), we have $\lambda \approx 10^{-48}$ and the contribution of the gauge action is numerically negligible (and will be neglected). As for the femionic action, we choose to work in a convenient gauge, the one in which in all temporal links at $t \neq 0$ are set to the identity matrix. The effective action then reads

$$S_{eff} = S_F^0 + S_F^1 = -2 \sum_x ln \left(1 + h_1 TrU_x + h_1^2 TrU_x^\dagger + h_1^3 \right)$$

$$+2h_2 \sum_{<x,y>} \left(\frac{h_1 TrU_x + 2h_1^2 TrU_x^\dagger + 3h_1^3}{1 + h_1 TrU_x + h_1^2 TrU_x^\dagger + h_1^3} \right) \left(\frac{h_1 TrU_y + 2h_1^2 TrU_y^\dagger + 3h_1^3}{1 + h_1 TrU_y + h_1^2 TrU_y^\dagger + h_1^3} \right) .$$

The action is written in terms of $\{U_x\}$, the temporal links at the spatial site x and $t = 0$. These are matrices $\in SU(3)$ and, after complexifying the degrees of freedom, they become matrices $\in SL(3, \mathbb{C})$. Occurrences of $U_x^\dagger$ are replaced by U_x^{-1}. The effective action becomes

$$S_{eff} = S_F^0 + S_F^1 = -2 \sum_x ln \left(1 + h_1 TrU_x + h_1^2 TrU_x^{-1} + h_1^3 \right)$$

$$+2h_2 \sum_{<x,y>} \left(\frac{h_1 TrU_x + 2h_1^2 TrU_x^{-1} + 3h_1^3}{1 + h_1 TrU_x + h_1^2 TrU_x^{-1} + h_1^3} \right) \left(\frac{h_1 TrU_y + 2h_1^2 TrU_y^{-1} + 3h_1^3}{1 + h_1 TrU_y + h_1^2 TrU_y^{-1} + h_1^3} \right) .$$

We want to determine what are the critical points of the complexified action. Let's first recall some useful properties of the Lie derivative:

1. $\nabla^a Tr[U] = iTr[T^a U]$
2. $\nabla^a Tr[U^{-1}] = -iTr[U^{-1} T^a]$
3. $\nabla^b \nabla^a Tr[U] = -Tr[T^a T^b U]$

4. $\nabla^b \nabla^a Tr[U^{-1}] = -Tr[U^{-1} T^b T^a]$.

Here $\{T^a\}_{a=1,\ldots,8}$ denote the generators of $SU(3)$, normalized so that $Tr\left[T^a T^b\right] = \frac{1}{2}\delta^{ab}$. The critical points are defined as those points p_σ such that $\nabla^a_z S_F \Big|_{p_\sigma} = 0$.

For the leading term of the action, S_F^0, we find the following gradient

$$\begin{aligned} \nabla^a_z S_F^0 &= -2\nabla^a ln\left(1 + h_1 TrU_z + h_1^2 TrU_z^{-1} + h_1^3\right) \\ &= \frac{-2\nabla^a\left(1 + h_1 TrU_z + h_1^2 TrU_z^{-1} + h_1^3\right)}{\left(1 + h_1 TrU_z + h_1^2 TrU_z^{-1} + h_1^3\right)} \\ &= \frac{-2i\left(h_1 Tr[T^a U_z] - h_1^2 Tr[U_z^{-1} T^a]\right)}{\left(1 + h_1 TrU_z + h_1^2 TrU_z^{-1} + h_1^3\right)} \ . \end{aligned} \tag{3.2}$$

Since $\{T^a\}_{a=1,\ldots,8}$ are traceless matrices, we immediately see that every mixture of center elements of $SU(3)$, $\left\{U_z = \mathbb{I}\, e^{i\omega_z} \mid \omega_z \in 0, \pm\frac{2\pi}{3}\right\}_z$, is a critical point.

For the following term of the action in the hopping parameter expansion, S_F^1, we find

$$\nabla^a_z S_F^1 = +2h_2 \left(\nabla^a \left(\frac{h_1 TrU_z + 2h_1^2 TrU_z^{-1} + 3h_1^3}{1 + h_1 TrU_z + h_1^2 TrU_z^{-1} + h_1^3}\right)\right) \tag{3.3}$$

$$\left(\sum_{x=z\pm\hat{\mu}} \frac{h_1 TrU_x + 2h_1^2 TrU_x^{-1} + 3h_1^3}{1 + h_1 TrU_x + h_1^2 TrU_x^{-1} + h_1^3}\right) \ . \tag{3.4}$$

After computing the remaining Lie derivative, one obtains

$$\begin{aligned} &\nabla^a \left(\frac{h_1 TrU_z + 2h_1^2 TrU_z^{-1} + 3h_1^3}{1 + h_1 TrU_z + h_1^2 TrU_z^{-1} + h_1^3}\right) = \\ &= \frac{\nabla^a\left(h_1 TrU_z + 2h_1^2 TrU_z^{-1} + 3h_1^3\right)}{1 + h_1 TrU_z + h_1^2 TrU_z^{-1} + h_1^3} - \frac{h_1 TrU_z + 2h_1^2 TrU_z^{-1} + 3h_1^3}{\left(1 + h_1 TrU_z + h_1^2 TrU_z^{-1} + h_1^3\right)^2} \cdot \\ &\cdot \nabla^a\left(1 + h_1 TrU_z + h_1^2 TrU_z^{-1} + h_1^3\right) = \\ &= \frac{ih_1 Tr[T^a U_z] - 2ih_1^2 Tr[U_z^{-1} T^a]}{1 + h_1 TrU_z + h_1^2 TrU_z^{-1} + h_1^3} - \frac{h_1 TrU_z + 2h_1^2 TrU_z^{-1} + 3h_1^3}{\left(1 + h_1 TrU_z + h_1^2 TrU_z^{-1} + h_1^3\right)^2} \cdot \\ &\cdot \left(ih_1 Tr[T^a U_z] - ih_1^2 Tr[U_z^{-1} T^a]\right) = \\ &= i\frac{\begin{pmatrix} h_1 Tr[T^a U_z] - 2h_1^2 Tr[U_z^{-1} T^a] - h_1^3 (Tr[T^a U_z] TrU_z^{-1} + Tr[U_z^{-1} T^a] TrU_z) \\ -2h_1^4 Tr[T^a U_z] + h_1^5 Tr[U_z^{-1} T^a] \end{pmatrix}}{\left(1 + h_1 TrU_z + h_1^2 TrU_z^{-1} + h_1^3\right)^2} \ . \end{aligned}$$

Since $\nabla^a_z S_F^1$ is a sum of terms $\propto Tr[T^a U_z]$, $Tr[U_z^{-1} T^a]$, the critical points of the theory are again given by mixtures of center elements of $SU(3)$.

3.2.2 Reflection symmetry

The theory has a reflection symmetry, that is

$$S(\{-\overline{A}_x\}) = \overline{S(\{A_x\})} \ ,$$

where $U_x = e^{iA_x}$ and $e^{i(-\overline{A}_x)} = \overline{U}_x$. Equivalently one has that

$$S(\{\overline{U}_x\}) = \overline{S(\{U_x\})} \ .$$

Indeed this relation is fulfilled by the action 3.1, since h_1 and h_2 are real parameters and $Tr(\overline{U}) = \overline{Tr(U)}$.

As a consequence we expect critical points to occur in complex conjugate pairs (a result that we already have found) and we also expect their thimble to give conjugate contributions (a result that we have confirmed in our simulations).

3.2.3 Hessian of the action and the Takagi problem

In order to determine a basis for the tangent base at the critical points, which we need as a starting condition for the parallel transport equations, we have to calculate the hessian of the action. Let's start by calculating the hessian of S_F^0. One has

$$\begin{aligned}
\nabla_w^b \nabla_z^a S_F^0 &= \nabla_w^b \left(\frac{-2\nabla^a \left(1 + h_1 TrU_z + h_1^2 TrU_z^{-1} + h_1^3\right)}{\left(1 + h_1 TrU_z + h_1^2 TrU_z^{-1} + h_1^3\right)} \right) = \qquad (3.5)\\
&= \frac{-2\nabla_w^b \nabla^a \left(1 + h_1 TrU_z + h_1^2 TrU_z^{-1} + h_1^3\right)}{\left(1 + h_1 TrU_z + h_1^2 TrU_z^{-1} + h_1^3\right)} + \\
&\quad + \frac{2\nabla^a \left(1 + h_1 TrU_z + h_1^2 TrU_z^{-1} + h_1^3\right)}{\left(1 + h_1 TrU_z + h_1^2 TrU_z^{-1} + h_1^3\right)^2} \cdot \\
&\quad \cdot \nabla_w^b \left(1 + h_1 TrU_z + h_1^2 TrU_z^{-1} + h_1^3\right) = \\
&= \frac{2\delta^{wz} \left(h_1 Tr[T^a T^b U_z] + h_1^2 Tr[U_z^{-1} T^b T^a]\right)}{\left(1 + h_1 TrU_z + h_1^2 TrU_z^{-1} + h_1^3\right)} + \\
&\quad - \frac{2\delta^{wz} \left(h_1 Tr[T^a U_z] - h_1^2 Tr[U_z^{-1} T^a]\right)}{\left(1 + h_1 TrU_z + h_1^2 TrU_z^{-1} + h_1^3\right)^2} \cdot \left(h_1 Tr[T^b U_z] - h_1^2 Tr[U_z^{-1} T^b]\right) \ .
\end{aligned}$$

The second term of the sum is $\propto Tr[T^a U_z]$, $Tr[U_z^{-1} T^a]$ and vanishes when evaluated at the critical points. Hence for the hessian evaluated at the critical points we are left with

$$\begin{aligned}
\nabla_w^b \nabla_z^a S_F^0 \Big|_{p_\sigma} &= \frac{-2\nabla_w^b \nabla^a \left(1 + h_1 TrU_z + h_1^2 TrU_z^{-1} + h_1^3\right)}{\left(1 + h_1 TrU_z + h_1^2 TrU_z^{-1} + h_1^3\right)} \Big|_{p_\sigma} \qquad (3.6)\\
&= \frac{2\delta^{wz} \left(h_1 Tr[T^a T^b U_z] + h_1^2 Tr[U_z^{-1} T^b T^a]\right)}{\left(1 + h_1 TrU_z + h_1^2 TrU_z^{-1} + h_1^3\right)} \Big|_{p_\sigma} = \\
&= \delta^{wz} \delta^{ab} \frac{\left(h_1 e^{i\omega_z} + h_1^2 e^{-i\omega_z}\right)}{\left(1 + 3h_1 e^{i\omega_z} + 3h_1^2 e^{-i\omega_z} + h_1^3\right)} \ .
\end{aligned}$$

The calculation of the hessian of S_F^1 is a bit more tedious, but it can be carried out yielding

$$\begin{aligned}
\nabla_w^b \nabla_z^a S_F^1 &= -2h_2 \left[\frac{\begin{array}{c} h_1 Tr[T^a U_z] - 2h_1^2 Tr[U_z^{-1} T^a] - h_1^3 (Tr[T^a U_z] + Tr[U_z^{-1} T^a]) \\ -2h_1^4 Tr[T^a U_z] + h_1^5 Tr[U_z^{-1} T^a] \end{array}}{(1 + h_1 TrU_z + h_1^2 TrU_z^{-1} + h_1^3)^2} \right] \\
&\cdot \left[\sum_{x=z\pm\hat{\mu}} \delta_{wx} \frac{\begin{array}{c} h_1 Tr[T^b U_x] - 2h_1^2 Tr[U_x^{-1} T^b] - h_1^3 (Tr[T^b U_x] + Tr[U_x^{-1} T^b]) \\ -2h_1^4 Tr[T^b U_x] + h_1^5 Tr[U_x^{-1} T^b] \end{array}}{(1 + h_1 TrU_x + h_1^2 TrU_x^{-1} + h_1^3)^2} \right] \\
&+4h_2 \delta_{wz} \left(h_1 Tr[T^b U_z] - h_1^2 Tr[U_z^{-1} T^b] \right) \\
&\cdot \left[\frac{\begin{array}{c} h_1 Tr[T^a U_z] - 2h_1^2 Tr[U_z^{-1} T^a] - h_1^3 (Tr[T^a U_z] TrU_z^{-1} \\ +Tr[U_z^{-1} T^a] TrU_z) - 2h_1^4 Tr[T^a U_z] + h_1^5 Tr[U_z^{-1} T^a] \end{array}}{(1 + h_1 TrU_z + h_1^2 TrU_z^{-1} + h_1^3)^3} \right] \\
&\cdot \left[\sum_{x=z\pm\hat{\mu}} \frac{h_1 TrU_x + 2h_1^2 TrU_x^{-1} + 3h_1^3}{1 + h_1 TrU_x + h_1^2 TrU_x^{-1} + h_1^3} \right] \\
&-2h_2 \delta_{wz} \left[\frac{\begin{array}{c} h_1 Tr[T^a T^b U_z] + 2h_1^2 Tr[U_a^{-1} T^b T^a] - h_1^3 (Tr[T^a T^b U_z] TrU_z^{-1} - Tr[T^a U_z] Tr[U_z^{-1} T^b] \\ -Tr[U_z^{-1} T^b T^a] TrU_z + Tr[U_z^{-1} T^a] Tr[T^b U_z]) - 2h_1^4 Tr[T^a T^b U_z] - h_1^5 Tr[U_a^{-1} T^b T^a] \end{array}}{(1 + h_1 TrU_z + h_1^2 TrU_z^{-1} + h_1^3)^2} \right] \\
&\cdot \left[\sum_{x=z\pm\hat{\mu}} \frac{h_1 TrU_x + 2h_1^2 TrU_x^{-1} + 3h_1^3}{1 + h_1 TrU_x + h_1^2 TrU_x^{-1} + h_1^3} \right]
\end{aligned} \tag{3.7}$$

Evaluating at the critical points, only the third term survives:

$$\begin{aligned}
\nabla_w^b \nabla_z^a S_F^1 \Big|_{p_\sigma} &= -h_2 \delta_{wz} \delta_{ab} \left(\frac{(h_1 - 2h_1^4) e^{i\omega_z} + (2h_1^2 - h_1^5) e^{-i\omega_z}}{(1 + 3h_1 e^{i\omega_z} + 3h_1^2 e^{-i\omega_z} + h_1^3)^2} \right) \cdot \\
&\cdot \left(\sum_{x=z\pm\hat{\mu}} \frac{3h_1 e^{i\omega_x} + 6h_1^2 e^{-i\omega_x} + 3h_1^3}{1 + 3h_1 e^{i\omega_x} + 3h_1^2 e^{-i\omega_x} + h_1^3} + \right) \ .
\end{aligned} \tag{3.8}$$

All in all we obtained an expression for the hessian of S_F evaluated at the critical points of the form

$$\nabla_w^b \nabla_z^a S_F \Big|_{p_\sigma} = \delta_{wz} \delta_{ab} \left[f(z) + g(z) \left(\sum_{\hat{\mu}} h(z + \hat{\mu}) + h(z - \hat{\mu}) \right) \right] \ . \tag{3.9}$$

Then, if we define $\gamma(z) \equiv f(z) + g(z) \left(\sum_{\hat{\mu}} h(z + \hat{\mu}) + h(z - \hat{\mu}) \right) \equiv |\gamma(z)| e^{i\phi(z)}$, it can be shown that the Takagi values and vectors are given respectively by

$$v_{az}^{j_1 j_2} = \delta_{aj_1} \delta_{zj_2} e^{-i\frac{\phi(z)}{2}} \tag{3.10}$$

$$\lambda^{j_1 j_2} = |\gamma(z = j_2)| \ . \tag{3.11}$$

Indeed, it can be shown that for the vectors defined as such the Takagi factorization theorem holds,

$$\begin{aligned}
v_{az}^{j_1 j_2} \nabla_w^b \nabla_z^a S_F v_{bw}^{h_1 h_2} &= \delta_{aj_1} \delta_{zj_2} e^{-i\frac{\phi(z)}{2}} \delta_{wz} \delta_{ab} |\gamma(z)| e^{i\phi(z)} \delta_{bh_1} \delta_{wh_2} e^{-i\frac{\phi(w)}{2}} \\
&= \delta_{j_1 h_1} \delta_{j_2 h_2} |\gamma(z = h_2)| = \lambda^{j_1 j_2} \delta_{j_1 h_1} \delta_{j_2 h_2} \ .
\end{aligned} \tag{3.12}$$

From the previous expression for the Takagi values, one may also derive the Takagi determinant

$$det\Lambda_\sigma = \prod_i \lambda_i = \left(\prod_{z \in V} |\gamma(z)| \right)^{N_c^2 - 1} . \tag{3.13}$$

3.2.4 Monte Carlo simulations

In this work we made the very first step in simulating the theory. We considered the action up to the leading term in the hopping parameter expansion,

$$S = -2 \sum_x ln \left(1 + h_1 Tr U_x + h_1^2 Tr U_x^{-1} + h_1^3 \right) .$$

This simplified action is valid in the limit of very heavy quarks. The steepest ascent equations are

$$\frac{dU_x}{dt} = i(\sum_a T^a \overline{\nabla_x^a S[U]}) U_x ,$$

where the drift term is determined by the gradient of the action, which we have derived previously

$$\nabla_x^a S[U] = -2i \frac{h_1 Tr[T^a U_x] - h_1^2 Tr[U_x^{-1} T^a]}{1 + h_1 Tr U_x + h_1^2 Tr U_x^{-1} + h_1^3} .$$

By making use of the property

$$U = \frac{1}{N_c} Tr(U) \mathbb{I} + 2 \sum_a Tr(T^a U) T^a$$

$$\sum_a Tr(T^a U) T^a = \frac{1}{2} (U - \frac{1}{N_c} Tr(U) \mathbb{I}) \equiv \frac{1}{2} (U)_{Tr},$$

where we denoted the traceless part of a matrix M with $(M)_{Tr}$, the drift can be expressed as

$$\sum_a T^a \overline{\nabla_x^a S[U]} = \left(-i \alpha_x (h_1 U_x - h_1^2 U_x^{-1})_{Tr} \right)^\dagger ,$$

$$\text{with } \alpha_x \equiv (1 + h_1 Tr U_x + h_1^2 Tr U_x^{-1} + h_1^3)^{-1} .$$

The parallel transport equations for the tangent space basis vectors are

$$\frac{dV_{zc}}{dt} = \sum_{w,a} \overline{V_{wa} \nabla_w^a \nabla_z^c S[U]} + \sum_{a,b} f^{abc} V_{za} \overline{\nabla_z^b S[U]} ,$$

where the Hessian of the action is

$$\nabla_w^b \nabla_z^a S[U] = 2 \delta_{wz} \left[\frac{(h_1 Tr[T^a T^b U_z] + h_1^2 Tr[U_z^{-1} T^b T^a])}{(1 + h_1 Tr U_z + h_1^2 Tr U_z^{-1} + h_1^3)} - \right.$$

$$\left. \frac{(h_1 Tr[T^a U_z] - h_1^2 Tr[U_z^{-1} T^a])(h_1 Tr[T^b U_z] - h_1^2 Tr[U_z^{-1} T^b])}{(1 + h_1 Tr U_z + h_1^2 Tr U_z^{-1} + h_1^3)^2} \right] .$$

These can also be recast into the compact notation

$$\frac{d}{dt} V_z \equiv \frac{d}{dt} \sum_c V_{zc} T^c = \sum_{w,a,c} \overline{V_{wa} \nabla_w^a \nabla_z^c S[U]} T^c + \sum_{a,b,c} f^{abc} V_{za} \overline{\nabla_z^b S[U]} T^c =$$

$$= (\alpha_z(h_1 V_z U_z + h_1^2 U_z^{-1} V_z)_{Tr})^\dagger - (\alpha_z^2(h_1^2 U_z - h_1^3 U_z^{-1})_{Tr}(Tr[V_z U_z] - h_1 Tr[U_z^{-1} V_z]))^\dagger$$
$$-i[V_z, \overline{\nabla_z S[U]}] \ .$$

By solving the Takagi problem one finds $8 \cdot N_{sites}$ Takagi vectors and their associated Takagi values,

$$v_{az}^{(j_1 j_2)} = \delta_{a j_1} \delta_{z j_2} e^{-i\frac{\phi(z)}{2}}$$
$$\lambda^{(j_1 j_2)} = |\gamma(j_2)|$$

where the indexes j_1, j_2 run respectively from 1 to 8 and from 1 to N_{sites} and $\gamma(z)$ is defined by

$$\gamma(z) = \frac{h_1 e^{i\omega_z} + h_1^2 e^{-i\omega_z}}{1 + 3h_1 e^{i\omega_z} + 3h_1^2 e^{-i\omega_z} + h_1^3} \equiv |\gamma(z)| \ e^{i\phi(z)} \ .$$

We studied two observables, the Polyakov loop and the quark number density,

$$\begin{aligned} \langle L \rangle &= \left\langle \frac{1}{N_{sites}} \sum_z Tr U_z \right\rangle \\ \langle n \rangle &= \frac{T}{V} \frac{\partial ln Z}{\partial \mu} = \frac{1}{N_t N_{sites}} \frac{1}{Z} \frac{\partial Z}{\partial \mu} = \\ &= \frac{1}{N_t N_{sites}} \frac{1}{Z} \int \left[\prod_x dU_x \right] \left(-\frac{\partial S}{\partial \mu} \right) e^{-S_G[U] - S_F[U]} \ . \end{aligned} \tag{3.14}$$

The operator n is obtained by taking the derivative of the action with respect to the chemical potential

$$\begin{aligned} n &= \frac{1}{N_t N_{sites}} \left(-\frac{\partial S}{\partial \mu} \right) = \\ &= 2 \frac{1}{N_t N_{sites}} \sum_z \frac{\partial}{\partial \mu} ln \left(1 + h_1 Tr U_z + h_1^2 Tr U_z^{-1} + h_1^3 \right) = \\ &= 2 \frac{1}{N_t N_{sites}} \sum_z \frac{N_t \left(h_1 Tr U_z + 2h_1^2 Tr U_z^{-1} + 3h_1^3 \right)}{\left(1 + h_1 Tr U_z + h_1^2 Tr U_z^{-1} + h_1^3 \right)} = \\ &= 2 \frac{1}{N_{sites}} \sum_z \frac{\left(h_1 Tr U_z + 2h_1^2 Tr U_z^{-1} + 3h_1^3 \right)}{\left(1 + h_1 Tr U_z + h_1^2 Tr U_z^{-1} + h_1^3 \right)} \ . \end{aligned} \tag{3.15}$$

In the limits $h_1 \to 0, \infty$, the quark number density operator tends asymptotically to $0, 2N_c$. These limits corresponds respectively to the limit of zero chemical potential, where the quark number density vanishes, and the limit of infinite chemical potential, where the quark number density saturates to twice the number of colors. Note that by using this simplified action, in absence of any coupling between neighbor lattice sites, a three dimensional system of with a spatial lattice length N_s can be regarded as equivalent to a unidimensional system with a spatial lattice length N_s^3.

For the simulations we have used the parameters $N_t = 116$, $\beta = 5.7$, $k = 0.0000887$ and we varied the chemical potential from $\mu = 0.9990\mu_c$ to $\mu = 1.0010\mu_c$, where $\mu_c \equiv m = -ln(2k)$. As we have seen previously, the critical points of this theory are mixture of center elements of the $SU(3)$ color group: their number grows exponentially with the number of sites as $3^{N_{sites}}$. In order to find out which are the most relevant we can make use of the Gaussian approximation

$$Z \approx \sum_\sigma Z_\sigma^{SC} = (2\pi)^{\frac{n}{2}} \sum_\sigma n_\sigma \frac{e^{-S(z_\sigma)}}{\sqrt{\prod_i \lambda_i^{(\sigma)}}} e^{i\omega_\sigma} \equiv (2\pi)^{\frac{n}{2}} \sum_\sigma n_\sigma e^{-S_{eff}^\sigma} e^{i\omega_\sigma} \ .$$

The Gaussian weights can be reconstructed by sampling critical points $\propto e^{-S^{\sigma}_{eff}}$. Numerical results are illustrated in fig. 3.1 for two different volumes at a chemical potential $\mu = 0.9990\mu_c$. The histogram represents the Gaussian weights of the thimbles attached to the critical points having an ever increasing number of temporal links set any center elements other than the identity. For volumes up to 3^3 the dominant thimble (the one associated to the critical point where all links are set to the identity matrix) is the most relevant, with at most a non negligible contribution coming from the sub-leading thimbles (the ones associated to the critical points having precisely one link set to other center elements). Eventually, as we increase the volume, many other critical points give a non negligible contribution due to combinatorics.

We ran simulations on lattices having $N_{sites} = 1, 2, 4$. Admittedly these are very small-sized systems. Nonetheless thimble contributions are collected entirely a-priori in this case, using the first method to compute the weights discussed at the beginning of this chapter. Hence these numerical experiments are a clean way to show that multi-thimble simulations are, at least conceptually, a theoretically sound approach.

Figs. 3.2, 3.3 and 3.4 illustrate respectively the results obtained for $N_{sites} = 1, 2, 4$ from one-thimble simulations (top figures) and from multi-thimble simulations (bottom figures). The colored solid lines represent the analytical solutions, which are known for this simplified model. The colored error bars represent the numerical data from the simulations. The results for the quark number density (multiplied by a factor $\frac{1}{6}$) are illustrated in red, the ones for the Polyakov loop are depicted in green. The results from the simulations performed on the fundamental thimble alone show for both observables discrepancies that become larger and larger as we decrease μ from $\mu = 1.0\mu_c$ to $\mu = 0.9990\mu_c$ and as we increase it from $\mu = 1.0\mu_c$ to $\mu = 1.0010\mu_c$. We also performed multi-thimble simulations, sampling both the fundamental thimble and the sub-leading thimbles. There exist two distinct sub-leading thimbles, corresponding to two possible choices for the link to be set to a center element other than the identity ($\omega_z = \pm\frac{2\pi}{3}$). However these thimbles give conjugate contributions, therefore only one independent contribution is needed (in addition to the contribution from the fundamental thimble). The numerical results from multi-thimble simulations show that all discrepancies disappear after we take into account the sub-leading thimbles.

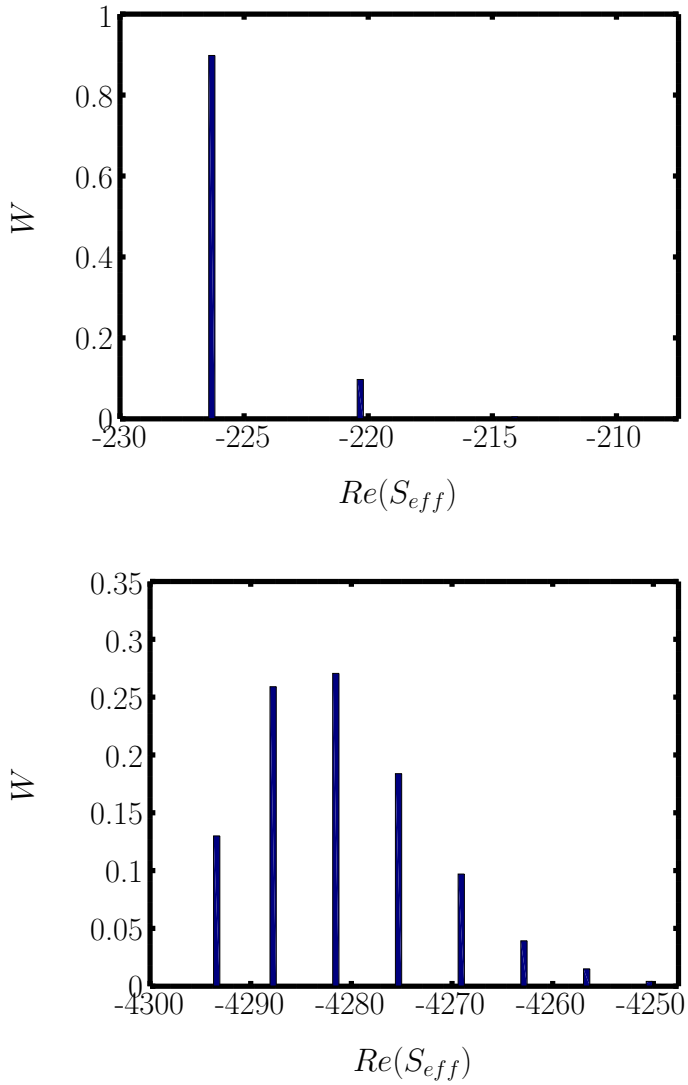

Figure 3.1: Heavy-dense QCD: Gaussian weights for $N_{sites} = 3^3$ (top) and $N_{sites} = 8^3$ (bottom). Parameters used are $N_t = 116$, $k = 0.0000887$, $\mu = 0.9990\mu_c$.

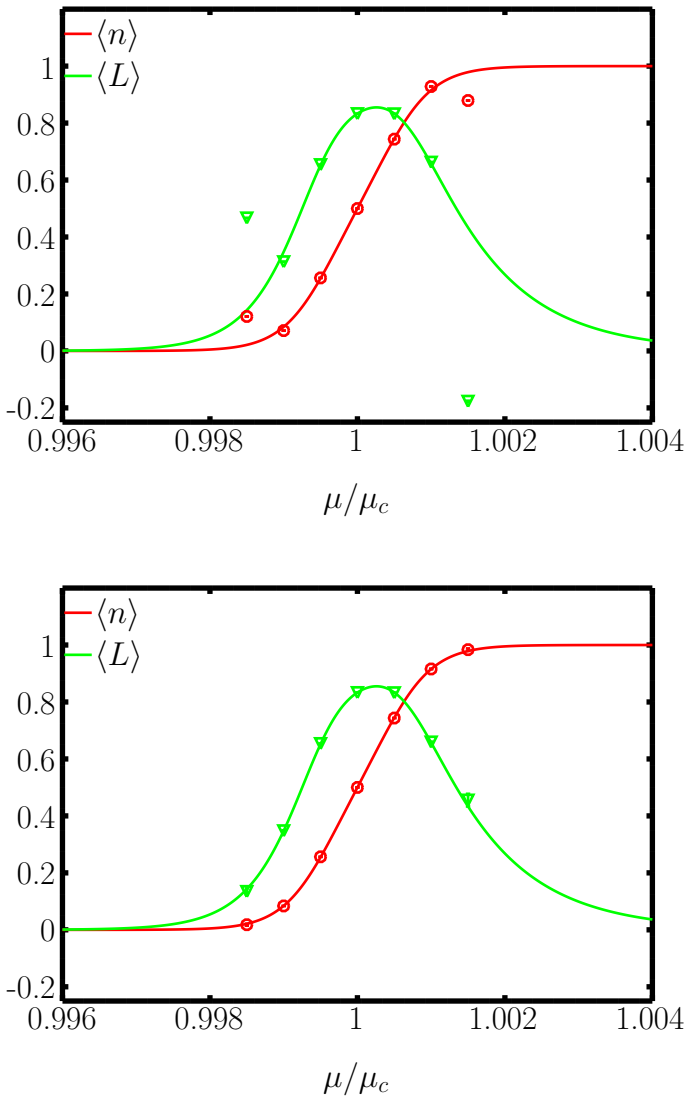

Figure 3.2: Heavy-dense QCD: results for the quark number density (red) and the Polyakov loop (green) obtained from 1 thimble (top) and 3 thimbles (bottom), $N_{sites} = 1$. Parameters used are $N_t = 116$, $k = 0.0000887$.

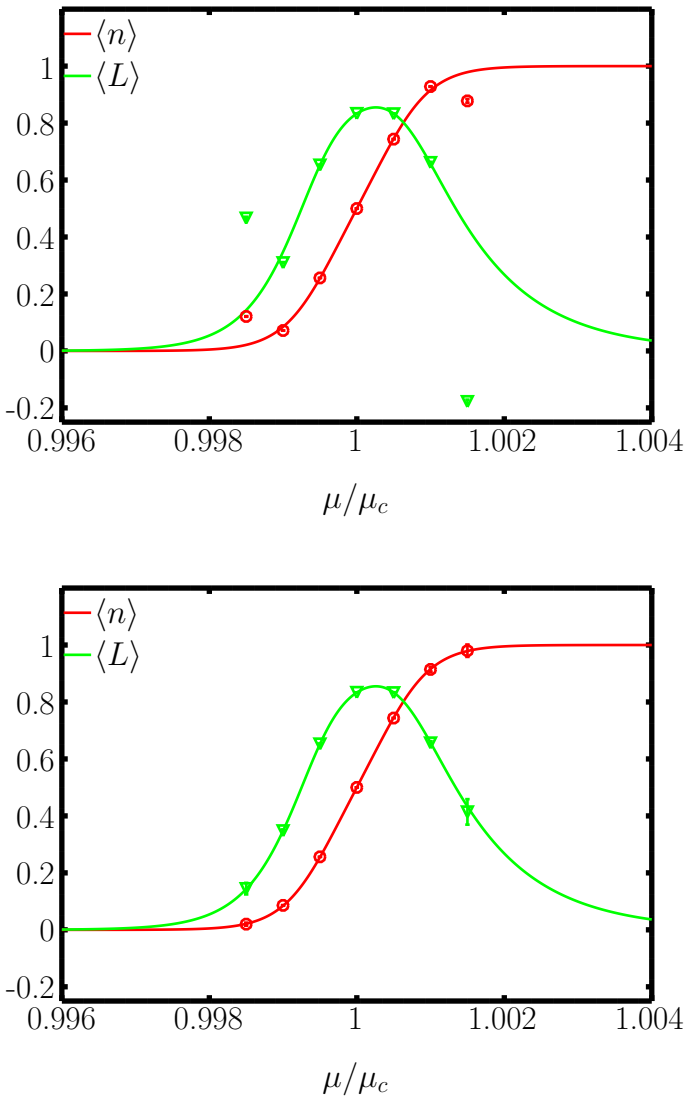

Figure 3.3: Heavy-dense QCD: results for the quark number density (red) and the Polyakov loop (green) obtained from 1 thimble (top) and 3 thimbles (bottom), $N_{sites} = 2$. Parameters used are $N_t = 116$, $k = 0.0000887$.

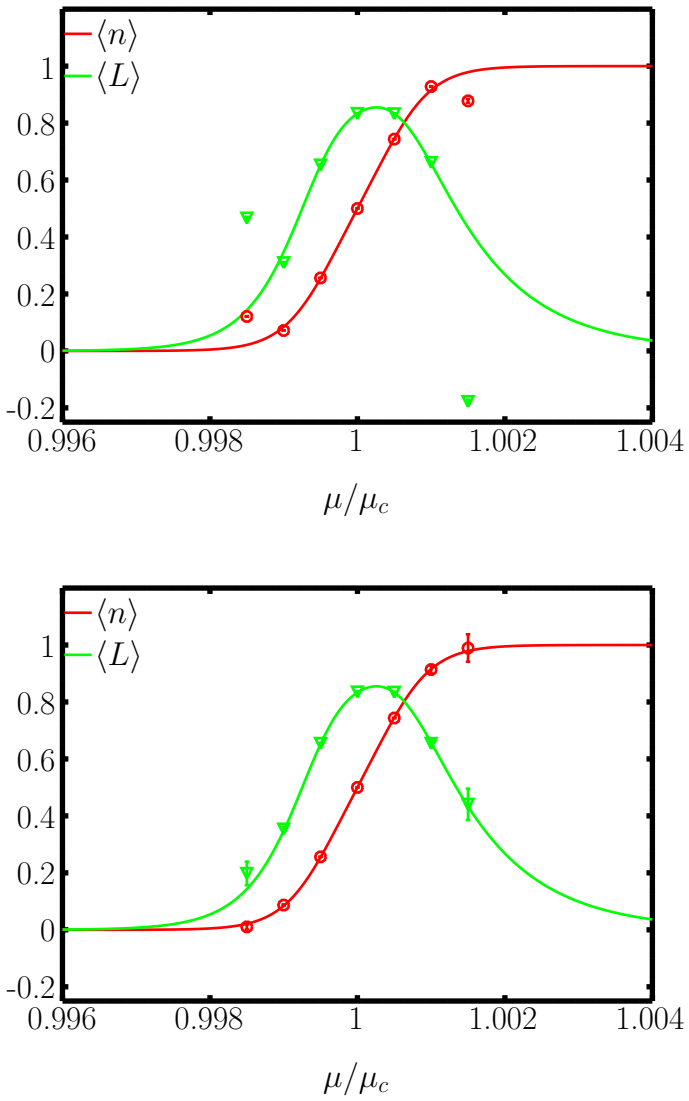

Figure 3.4: Heavy-dense QCD: results for the quark number density (red) and the Polyakov loop (green) obtained from 1 thimble (top) and 3 thimbles (bottom), $N_{sites} = 4$. Parameters used are $N_t = 116$, $k = 0.0000887$.

3.3 Case study 2 - the one-dimensional Thirring model

As a second application we consider the one-dimensional Thirring model [42–45, 50]. This theory is governed by the Eucliean Lagrangian

$$\mathcal{L} = \bar{\chi}(\gamma^4 \frac{d}{dt} + m + \gamma^4 \mu)\chi + \frac{g^2}{2}(\bar{\chi}\gamma^4\chi)^2 \ .$$

The quartic interaction can be canceled out by introducing an auxiliary field ϕ. In this formulation the Lagrangian reads

$$\mathcal{L} = \bar{\chi}(\gamma^4 \frac{d}{dt} + m + \gamma^4 \mu + i\gamma^4\phi)\chi + \beta\phi^2 \ ,$$

where $\beta = \frac{1}{2g^2}$ is the half inverse squared coupling constant. On the lattice, the partition function of the Thirring model is

$$Z = \int \left(\prod_{i=1...L} d\phi_n \right) e^{-\beta \sum_{n=1...L}(1-cos(\phi_n)) + log\ detD},$$

where $L = N_t$ is the number of lattice sites and $detD$ is the determinant of the fermionic matrix, A closed form expression can be worked out for the fermionic determinant [43],

$$detD = \frac{1}{2^{L-1}} \left(cosh(L\hat{\mu} + i \sum_n \phi_n) + cosh(L\ asinh(\hat{m})) \right) \ .$$

Here $\hat{\mu}$ and $\hat{m}$ are the chemical potential and the fermion mass in lattice units. As anticipated this is exactly the same expression we've found in sec. 1.4.1. This theory can be solved exactly. An analytic solution for the partition function is known in terms of the modified Bessel function of the first kind $I_\alpha(z)$ [43],

$$Z = \frac{1}{2^{L-1}} e^{-L\beta} \left[I_1(\beta)^L cosh(L\hat{\mu}) + I_0(\beta)^L cosh(Lasinh(\hat{m})) \right] \ .$$

Hence analytical solutions can also be derived for the observables of the theory, such as the number density and the chiral condensate

$$\langle n \rangle = \frac{1}{L} \frac{\partial log\ Z}{\partial \hat{\mu}} = \frac{I_1(\beta)^L sinh(L\hat{\mu})}{I_1(\beta)^L cosh(L\hat{\mu}) + I_0(\beta)^L cosh(L\ asinh(\hat{m}))}$$

$$\langle \bar{\chi}\chi \rangle = \frac{1}{L} \frac{\partial log\ Z}{\partial \hat{m}} = \frac{1}{cosh(asinh(\hat{m}))} \frac{I_0(\beta)^L sinh(L\ asinh(\hat{m}))}{I_1(\beta)^L cosh(L\hat{\mu}) + I_0(\beta)^L cosh(L\ asinh(\hat{m}))} \ .$$

At finite chemical potentials this model is affected by a sign problem, stemming from the fermionic determinant $detD$. The Thirring model has has been used to explore alternative methods to fight the sign problem, see for instance refs. [42–45, 50]. In particular refs. [42–44] used the Lefschetz thimble method and performed Monte Carlo calculations on the dominant thimble. They found that the contribution from the dominant thimble is not enough to recover the correct results known from the analytical solutions, not even in the thermodynamic limit.

3.3.1 Critical points

We explored the theory by thimble regularization ourselves with the goal of collecting the contributions coming from more than one thimble in order to address the discrepancies due to the one-thimble approximation observed in the literature. The first thing we have to do is to complexify the degrees of freedom. The action of the model becomes

$$\beta \sum_{n=1...L} (1 - cos(z_n)) - log\ detD$$

$$detD = \frac{1}{2^{L-1}} \left(cosh(L\hat{\mu} + i \sum_n z_n) + cosh(L\ asinh(\hat{m})) \right) ,$$

where the auxiliary field z_n is now complex valued. Then we have to determine the critical points. These are the solutions of

$$\frac{\partial S}{\partial z_n} = \beta sin(z_n) - i\ \frac{sinh(L\hat{\mu} + i \sum_i z_i)}{cosh(L\hat{\mu} + i \sum_i z_i) + cosh(L\ asinh(\hat{m}))} = 0\ .$$

It follows that the critical points of the theory statisfy the equation

$$sin(z_n) = \frac{i}{\beta} \frac{sinh(L\hat{\mu} + i \sum_i z_i)}{cosh(L\hat{\mu} + i \sum_i z_i) + cosh(L\ asinh(\hat{m}))}\ .$$

From this equation one concludes that critical points are uniform field configurations where $z_i = z$ for all i, except possibly a number n_- of lattice points where $z_i = \pi - z$ (leaving $sin(z_n)$ unchanged). The critical points can then be labeled by the integer number $n_- = 0, 1, \ldots, \frac{L}{2}$ and by the complex number z. At fixed n_-, the values admitted for z are found by numerically solving

$$sin(z) = \frac{i}{\beta} \frac{sinh(L\hat{\mu} + i(L - 2n_-)z + in_-\pi)}{cosh(L\hat{\mu} + i(L - 2n_-)z + in_-\pi) + cosh(L\ asinh(\hat{m}))} =$$

$$= \frac{i}{\beta} \frac{sinh(L\hat{\mu} + i(L - 2n_-)z)}{cosh(L\hat{\mu} + i(L - 2n_-)z) + (-1)^{n_-} cosh(L\ asinh(\hat{m}))}\ .$$

For instance fig. 3.5 depicts the critical points in the $n_- = 0$ sector for $m = 1$, $L = 4$, $\beta = 1$ at $\mu = 0$. The figure only shows the critical points lying on the left complex half-plane. Other critical points exist in the right complex half-plane. These are obtained from the critical points present in the left complex half-plane by reflection with respect to the imaginary axis. Indeed if z is a critical point also $-\bar{z}$ is a critical point, but because of a symmetry it gives a conjugate contribution.

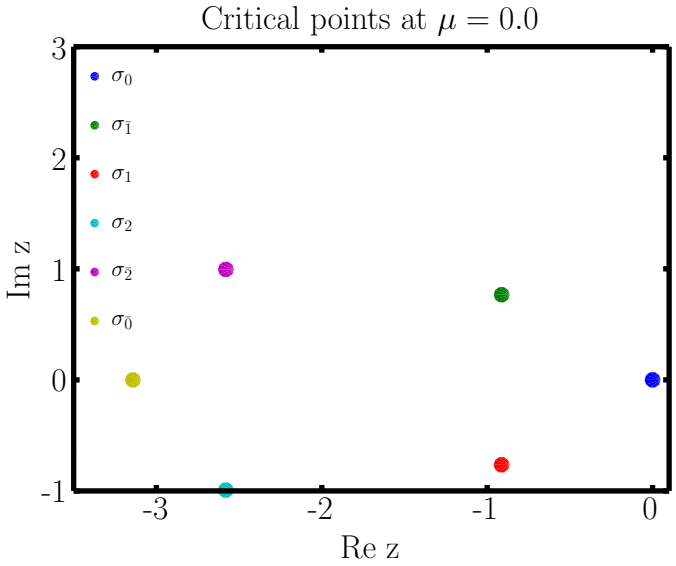

Figure 3.5: Thirring model: critical points in the $n_- = 0$ sector at $\mu = 0$. Parameters used are $L = 4$, $\beta = 1$, $m = 1$.

3.3.2 Reflection symmetry

We pointed out that if $p = (n_-, z)$ is a critical point, then $p' = (n_-, z' = -\overline{z})$ is also a critical point. This can be shown by proving that if p satisfies the condition of vanishing gradient, then so does p'. Since β is real, one has

$$\beta sin(z') = \beta sin(-\overline{z}) = -\beta sin(\overline{z}) = -\overline{\beta sin(z)} \ .$$

Now if we consider the hyperbolic functions $f = cosh(z),\ sinh(z)$, both are 2π-periodic on the imaginary axis, thus one has

$$f(L\hat{\mu}+i(L-2n_-)z'+in_-\pi) = f(L\hat{\mu}-i(L-2n_-)\overline{z}+in_-\pi) = f(L\hat{\mu}-i(L-2n_-)\overline{z}-in_-\pi+in_-2\pi) =$$

$$= f(L\hat{\mu}-i(L-2n_-)\overline{z}-in_-\pi) = f(\overline{L\hat{\mu} + i(L-2n_-)z + in_-\pi}) = \overline{f(L\hat{\mu} + i(L-2n_-)z + in_-\pi)} \ .$$

Therefore one also has that

$$\beta sin(z') - i\ \frac{sinh(L\hat{\mu} + i(L-2n_-)z' + in_-\pi)}{cosh(L\hat{\mu} + i(L-2n_-)z' + in_-\pi) + cosh(Lm)} =$$

$$= -\overline{\beta sin(z)} - i\ \overline{\frac{sinh(L\hat{\mu} + i(L-2n_-)z + in_-\pi)}{cosh(L\hat{\mu} + i(L-2n_-)z + in_-\pi) + cosh(Lm)}}$$

$$= -\left(\overline{\beta sin(z) - i\frac{sinh(L\hat{\mu} + i(L-2n_-)z + in_-\pi)}{cosh(L\hat{\mu} + i(L-2n_-)z + in_-\pi) + cosh(Lm)}}\right) = 0 \ ,$$

which is what we wanted to prove.

More generally, one can show that the theory fulfills a reflection symmetry. If we define the map $K : z \mapsto z' = Kz = L\overline{z} = -\overline{z}$, the theory satisfies

$$S(z) = \overline{S(z')} \ .$$

Indeed we have

$$\begin{cases} cos(z'_n) = cos(-\overline{z}_n) = cos(\overline{z}_n) = \overline{cos(z_n)} \\ cosh(L\hat{\mu} + i(L-2n)z' + in\pi) = \overline{cosh(L\hat{\mu} + i(L-2n)z + in\pi)} \end{cases} ,$$

which implies

$$S(z') = \beta \sum_n (1-cos(z'_n)) + ln(2^{L-1}) - ln(cosh(L\hat{\mu}+i(L-2n)z'+in\pi)+cosh(L\, asinh(\hat{m})))$$

$$= \overline{\beta \sum_n (1-cos(z_n))} + \overline{ln(2^{L-1})} - \overline{ln(cosh(L\hat{\mu}+i(L-2n)z'+in\pi)+cosh(L\, asinh(\hat{m})))}$$

$$= \overline{S(z)} \ .$$

In presence of a reflection symmetry we expect critical points and the attached thimbles to appear in conjugate pairs.

3.3.3 Hessian of the action and the Takagi problem

The hessian of the action is

$$H_{i,j} = \frac{\partial^2 S}{\partial z_i \partial z_j} = \beta cos(z_i)\delta_{i,j} + \frac{cosh(L\hat{\mu}+i\sum_n z_n)}{cosh(L\hat{\mu}+i\sum_n z_n)+cosh(L\ asinh(\hat{m}))}$$

$$- \frac{sinh^2(L\hat{\mu}+i\sum_n z_n)}{(cosh(L\hat{\mu}+i\sum_n z_n)+cosh(L\ asinh(\hat{m})))^2} \ .$$

Let's define $s(n_-, z) \equiv \sum_n z_n = (L-2n_-)z + n\pi$. At a given critical point $p_\sigma = (n_-, z)$ the Hessian is given by the sum of a diagonal matrix and a constant term

$$H_{i,j}\Big|_{p_\sigma} = \beta cos(z_i)\delta_{i,j} + f(n_-, z), \text{ with}$$

$$f(n_-, z) = \frac{cosh(L\hat{\mu}+i\ s(n_-,z))}{cosh(L\hat{\mu}+i\ s(n_-,z))+cosh(L\ asinh(\hat{m}))}$$

$$- \frac{sinh^2(L\hat{\mu}+i\ s(n,z))}{(cosh(L\hat{\mu}+i\ s(n_-,z))+cosh(L\ asinh(\hat{m})))^2} \ .$$

The Takagi problem can be solved numerically by diagonalizing the expanded Hessian $\tilde{H}_{i,j}\Big|_{p_\sigma}$.

3.3.4 Monte Carlo simulations

By making use of the expression we have derived for the gradient and the Hessian of S, we can write down the steepest ascent equations,

$$\frac{dz_n}{dt} = \frac{\partial \overline{S}}{\partial \overline{z}} = \overline{\beta sin(z_n) - \frac{i\ sinh(L\hat{\mu}+i\sum_j z_j)}{cosh(L\hat{\mu}+i\sum_j z_j)+cosh(L\ asinh(\hat{m}))}} \ ,$$

and the parallel transport equations,

$$\frac{dv_j^{(h)}}{dt} = \sum_i \overline{v_i^{(h)}} \left(\overline{\beta cos(z_i)\delta_{i,j} + \frac{cosh(L\hat{\mu}+i\sum_n z_n)}{cosh(L\hat{\mu}+i\sum_n z_n)+cosh(L\ asinh(\hat{m}))}} \right.$$

$$\left. - \overline{\frac{sinh^2(L\hat{\mu}+i\sum_n z_n)}{(cosh(L\hat{\mu}+i\sum_n z_n)+cosh(L\ asinh(\hat{m})))^2}} \right) \ .$$

As observables we have considered the fermion number density and the chiral condensate,

$$\langle n \rangle = \frac{1}{L}\frac{\partial lnZ}{\partial \hat{\mu}} = \frac{1}{L}\frac{1}{Z}\frac{\partial Z}{\partial \hat{\mu}} = \Big\langle \frac{sinh(L\hat{\mu} + i\sum_n z_n)}{cosh(L\hat{\mu} + i\sum_n z_n) + cosh(L\ asinh(\hat{m}))} \Big\rangle$$

$$\langle \bar{\chi}\chi \rangle = \frac{1}{L}\frac{\partial lnZ}{\partial \hat{m}} = \frac{1}{L}\frac{1}{Z}\frac{\partial Z}{\partial \hat{m}} = \Big\langle \frac{1}{cosh(\hat{m})}\frac{sinh(L\ asinh(\hat{m}))}{cosh(L\hat{\mu} + i\sum_n z_n) + cosh(L\ asinh(\hat{m}))} \Big\rangle .$$

Firstly, we ran one- and multi-thimble simulations for the parameters $L = 4$, $m = 1$, $\beta = 1$. A thorough analysis of the multi-thimble decomposition for the Thirring model has been carried out in ref. [43], where the authors studied the imaginary part of the action at the critical points as a function of the chemical potential in order to look for Stokes phenomena and to get information about changes in the thimble decomposition. In Stokes phenomena the stable thimble attached to a critical point overlaps with the unstable thimble attached to another critical point. Being S_I constant on the thimbles, this can only happen if the action has the same imaginary part at the two critical points. In presence of a Stokes phenomenon, the intersection numbers of the two thimbles can change.

Fig 3.6 (top) shows the critical points in the $n_- = 0$ sector as a function of μ. Fig. 3.6 (center) shows the imaginary part of the action evaluated at the critical points as a function of μ. Following ref. [43], at zero chemical potential the only critical points having a non-zero intersection number are σ_0 and $\sigma_{\bar{0}}$. [1] At $\mu \approx 0.40$ there is a Stokes phenomenon between σ_2 and $\sigma_{\bar{0}}$ (see the crossing between the yellow and the cyan line in fig. 3.6 (center)), after the Sokes the former enters the thimble decomposition while the latter exits the decomposition. Then at $\mu \approx 0.56$ there is another Stokes phenomenon between the critical points σ_1 and σ_0 and σ_1 acquires a non-zero intersection number. Again, at $\mu \approx 0.73$ there is a Stokes phenomenon between the critical points σ_1 and σ_2 and σ_2 exits the thimble decomposition. In fig. 1 (bottom) one can also see that in the region where $\sigma_{\bar{0}}$ and σ_2 have both a non-zero intersection number, the real part of the action on these is much larger than the real part of the action on the critical points σ_0 and σ_1. Therefore their contribution are suppressed.

[1] Actually this true provided that we add a small imaginary part to β, otherwise there is a Stokes phenomenon between the two critical points and the thimble decomposition is not well-defined.

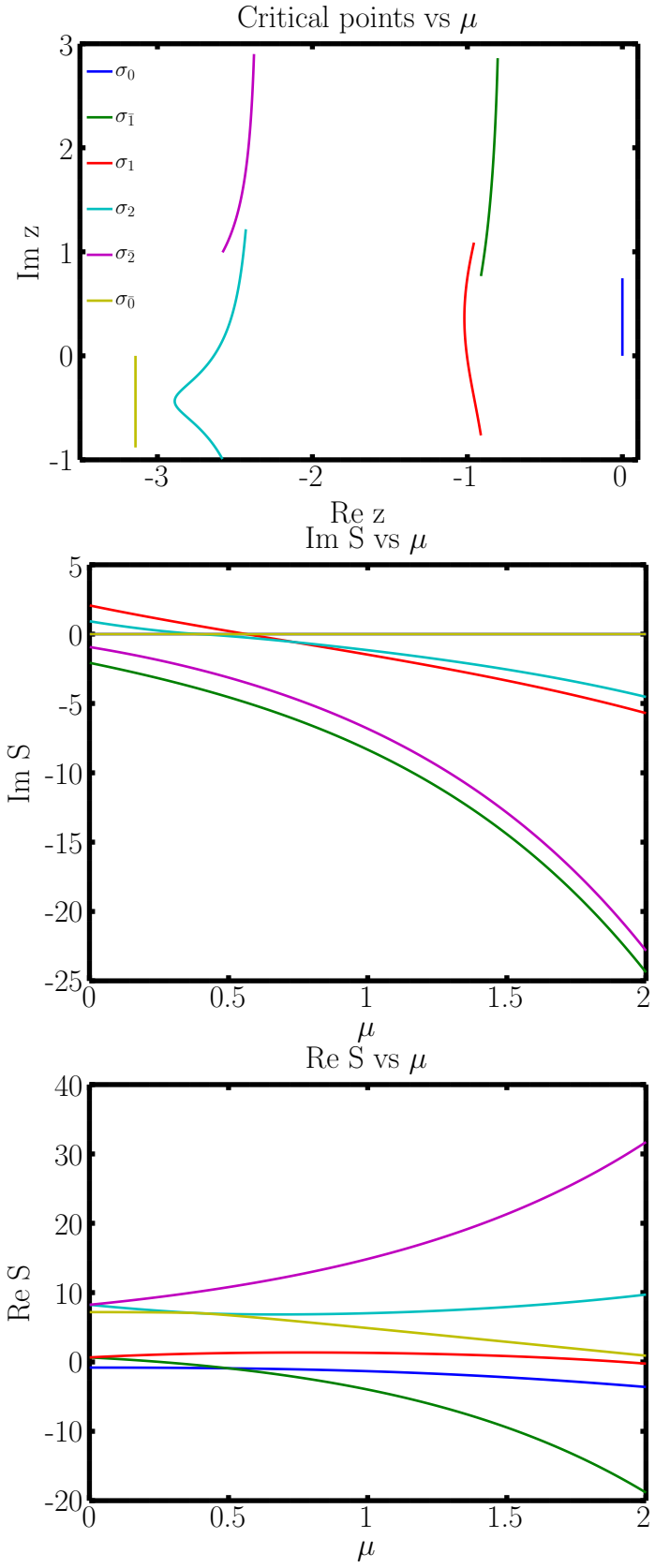

Figure 3.6: Thirring model: critical points in the $n_- = 0$ sector as a function of the chemical potential. Parameters used are $L = 4$, $\beta = 1$, $m = 1$. These figures show how the critical points move as μ is varied (top) and how the imaginary part (center) and real part (bottom) of the action changes at those critical points.

Figure 3.7 shows the results we obtained from one-thimble simulations on the dominant thimble $\mathcal{J}_{\sigma_0}$. The chemical potential was varied from $\mu = 0.0$ to $\mu = 1.95$. We also repeated the simulations for different values of $\beta = 1, 2, 4$, in order to check the effect of the coupling constant on the validity of the one-thimble approximation. These results confirm what was observed in refs. [43, 44]: while at low couplings the one-thimble approximations is good, at larger couplings the same approximation fails. Specifically, discrepancies between the numerical results and the analytical results begin to show up at $\beta = 2$ and become particularly noticeable at $\beta = 1$.

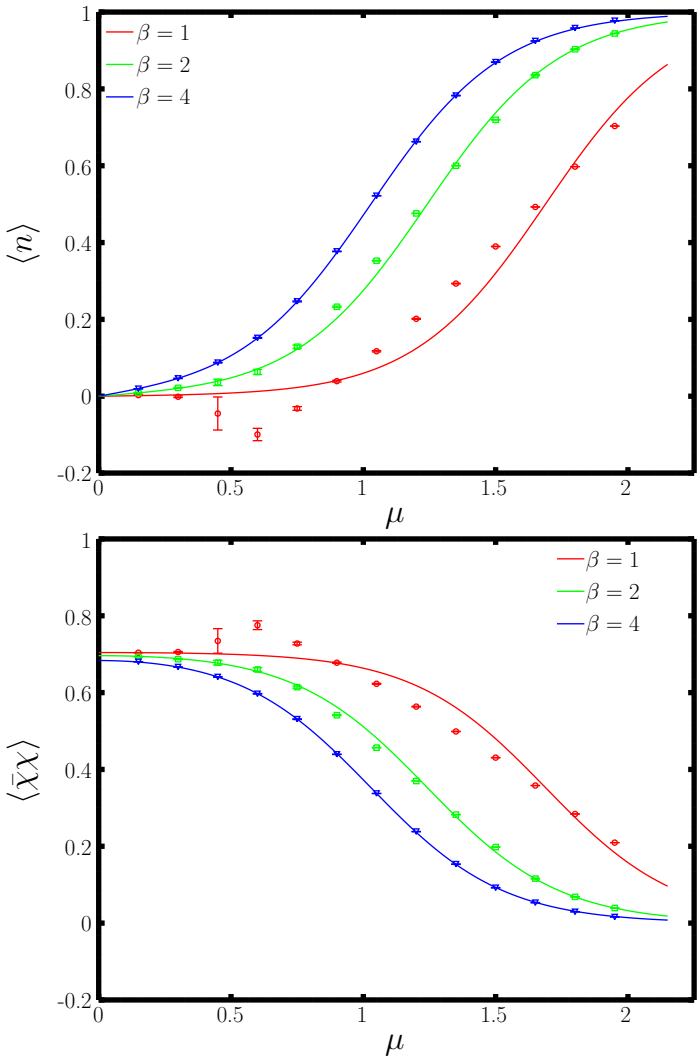

Figure 3.7: Thirring model: results obtained from one-thimble simulations for the fermion number density (top) and the chiral condensate (bottom) for $\beta = 1$, 2, 4 (red, green, blue). Parameters used are $L = 4$, $m = 1$.

We also tried to address these discrepancies by performing multi-thimble simulations, sampling both the fundamental thimble $\mathcal{J}_{\sigma_0}$ and the sub-leading thimble $\mathcal{J}_{\sigma_1}$. The relative weights of the thimbles have been determined by the second method we discussed at the beginning of this chapter, that is by fixing α from a known observable. Specifically, the results for the fermion number density have been obtained by fixing α from the analytical solution for the chiral condensate and viceversa.

Some useful insights useful for the Monte Carlo simulations were obtained by studying the lower dimensional case $L = 2, m = 1, \beta = 1$. Figure 3.8 shows the profile of the logarithm of the partial partition function as a function of n_0, that is the component of the initial displacement along the Takagi vector associated to the largest Takagi value. One can appreciate two peaks showing up around given values of n_0 for the thimble $\mathcal{J}_{\sigma_0}$. In the case of $\mathcal{J}_{\sigma_1}$ (see bottom picture of fig. 3.8) the peaks are thin enough that the relevant configurations are not representable in double precision. Therefore we ran the numerical simulations in quadruple precision. For the Metropolis acceptance step, we generated proposals using a smaller angle for rotations involving the direction n_0 than the one used for the other rotations.

The numerical results from the multi-thimble simulations for $L = 4$, $m = 1$, $\beta = 1, 2$ are shown in fig. 3.9. Though the region $\mu \approx 0.60 \div 0.75$ for $\beta = 1$ is affected by large statistical errors, elsewhere the discrepancies observed from the results of the simulations on $\mathcal{J}_{\sigma_0}$ disappear after taking into account the contribution from $\mathcal{J}_{\sigma_1}$. These results answer the question that was left open in ref. [42], that is whether the discrepancies observed using simulations performed on the dominant thimble can be addressed by collecting the contribution from the sub-dominant thimble. Admittedly we have answered the question using a small $L = 4$ lattice. Indeed carrying out multi-thimble simulations is hard. Specifically, for the Thirring model this is due in part to the somewhat pathological profile of $Z_{\hat{n}}^{(\sigma_1)}$ and in part to the difficulty in keeping a reasonable signal-to-noise ratio for the weights as we increase the number of degrees of freedom. In the next chapter we discuss what we regard as a more powerful approach. We are going to show that, using this latter approach, the Thirring model can be simulated towards the continuum limit (it turned out that $L = 64$ is enough for this purpose).

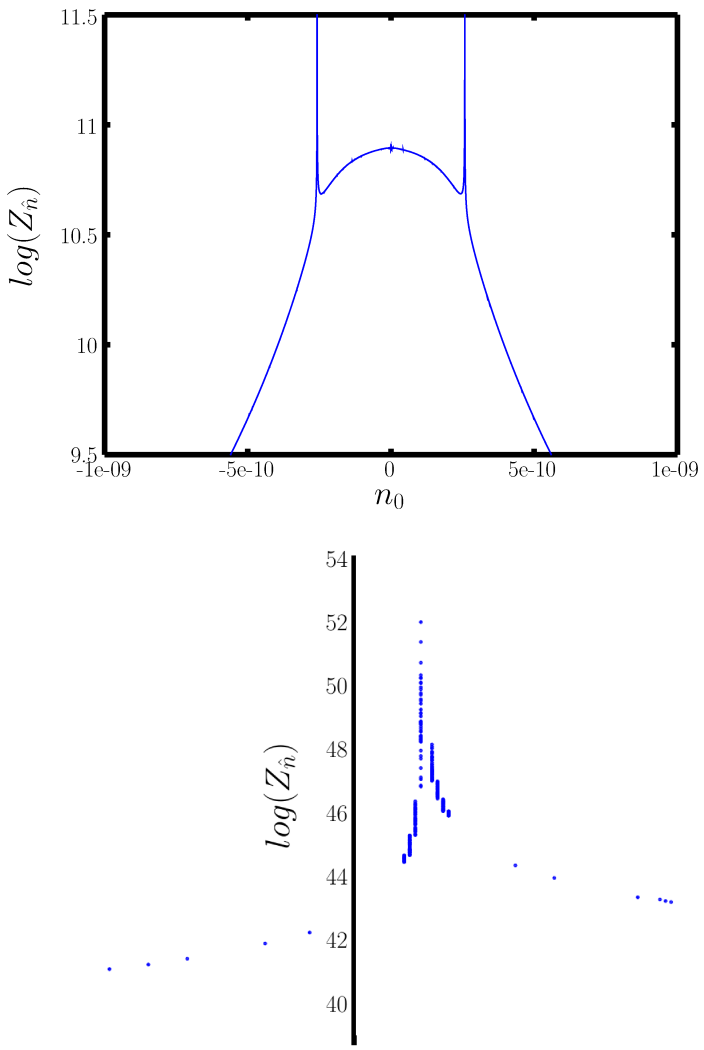

Figure 3.8: Thirring model: profiles of $log(Z_{\hat{n}}^{(\sigma_0)})$ (top) and $log(Z_{\hat{n}}^{(\sigma_1)})$ (bottom) as a function of n_0 for $L = 2$. Parameters used are $\beta = 1$, $m = 1$.

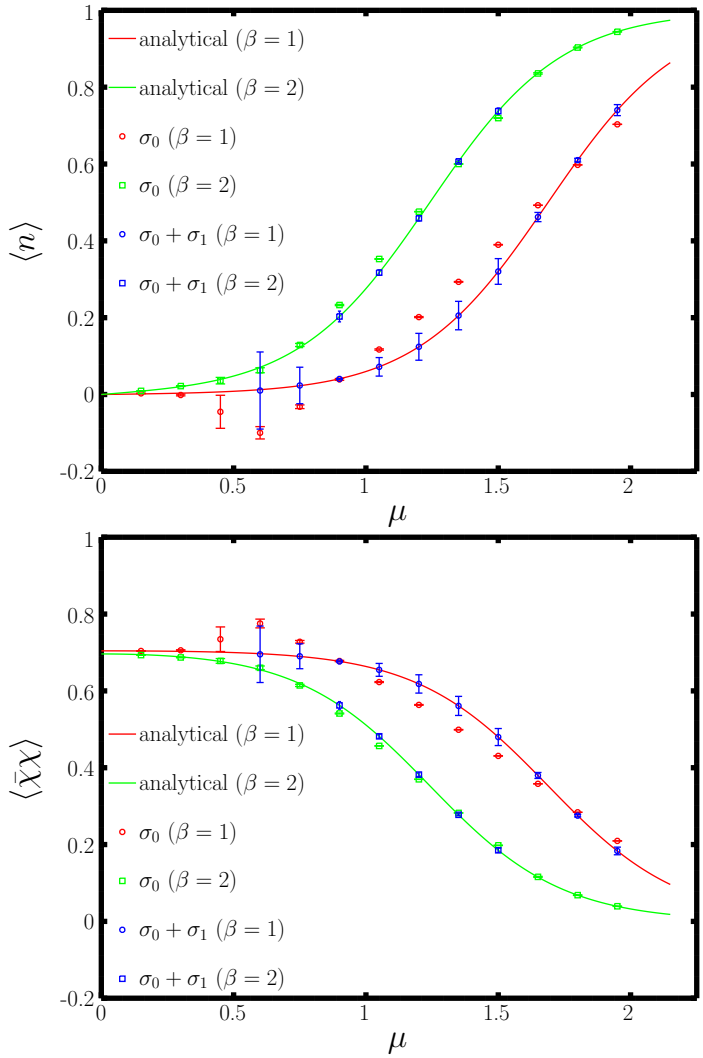

Figure 3.9: Thirring model: results obtained from one- and multi-thimble simulations for the fermion number density (top) and the chiral condensate (bottom) for $\beta = 1, 2$. Results obtained from 1 thimble are displayed respectively in red ($\beta = 1$) and green ($\beta = 2$), while results from 3 thimbles are displayed in blue ($\beta = 1$, 2). Parameters used are $L = 4$, $m = 1$.

Chapter 4

Taylor expansion on thimbles and Padé approximants

In this section we discuss how Taylor series expansions on the dominant thimbles can be used to extend the range of validity of the one-thimble approximation. The method is then applied to heavy-dense QCD and to the one-dimensional Thirring model.

4.1 Taylor expansion on thimbles

Conceptually the Lefschetz thimble regularization method provides a neat tool to fight the sign problem: the original integral is decomposed into a sum of integrals that are free of the sign problem and therefore well suited for calculation by importance sampling. In practice, however, performing multi-thimble simulations is a difficult problem because a general and satisfactory way to compute the correct weights to assign to each contribution is still missing. We made some progress on this front, by proposing two calculation methods. These were discussed in the previous chapter. In this chapter we explore a different point of view. We know from many counter-examples that the one-thimble approximation is not always enough to recover the correct results of the theory. However we argue that in some cases we can exploit the rich and dynamic thimble structure of a theory in order to by-pass the need for multi-thimble simulations. Indeed in general the thimble structure is not fixed in stone, it may change as we move within the parameters space of the theory. A key concept here is that of a Stokes phenomenon, as in the presence of Stokes phenomena the intersection numbers can change. An example is given by the Thirring model: at $\mu = 0$ the only relevant contribution is the one from the dominant thimble $\mathcal{J}_0$, but as we increase μ various Stokes phenomena take place. Thimbles that didn't enter the multi-thimble decomposition before a given Stokes do acquire a non-zero intersection number after the Stokes (and viceversa). As a consequence multiple regions can be identified. There are some *bad* regions where more than one thimble give a relevant contribution in the multi-thimble decomposition and there are some *good* regions where the one-thimble approximation is a valid approximation. Though the multi-thimble decomposition is discontinuous at the Stokes, physical observables are in general continuous quantities: the idea is then to reach the *bad* regions by Taylor expanding the observables around points located inside the *good* regions. Taylor coefficients can be calculated from one-thimble simulations.

It will be instructive to examine the case of a simple toy model, the one-dimensional ϕ^4 model. The model is governed by the action

$$S(\phi) = \frac{1}{2}\sigma\phi^2 + \frac{1}{4}\lambda\phi^4$$
$$\text{with } \sigma \in \mathbb{C}, \lambda \in \mathbb{R}^+ \ .$$

If we define $\phi = x + iy$, the real and imaginary parts of the action can be written as

$$S_R = \frac{1}{2}[\sigma_R(x^2 - y^2) - 2\sigma_I xy] + \frac{1}{4}\lambda[x^4 + y^4 - 6x^2y^2]$$
$$S_I = \frac{1}{2}[\sigma_I(x^2 - y^2) + 2\sigma_R xy] + \lambda[x^3y - y^3x] \ .$$

This theory has 3 critical points. As usual these are found by requiring a vanishing gradient,

$$\frac{dS}{d\phi} = \phi(\sigma + \lambda\phi^2) = 0$$
$$\rightarrow \begin{cases} \phi_0 = 0 \\ \phi_\pm = \pm\sqrt{-\frac{\sigma}{\lambda}} \ . \end{cases}$$

Fig. 4.1 shows how the thimble structure of the theory changes as σ_R is varied from a positive value to a negative one. Proceeding from the left to the right in the figure, σ_R is decreased while keeping fixed $\lambda = 2.0$ and $\sigma_I = 0.75$.

$Re(\sigma) > 0$

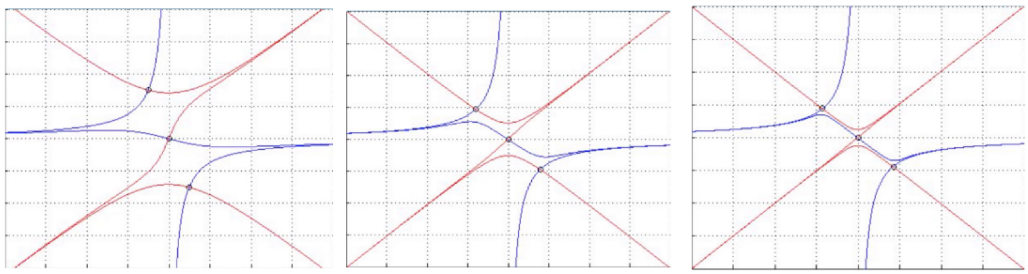

$Re(\sigma) \leq 0$

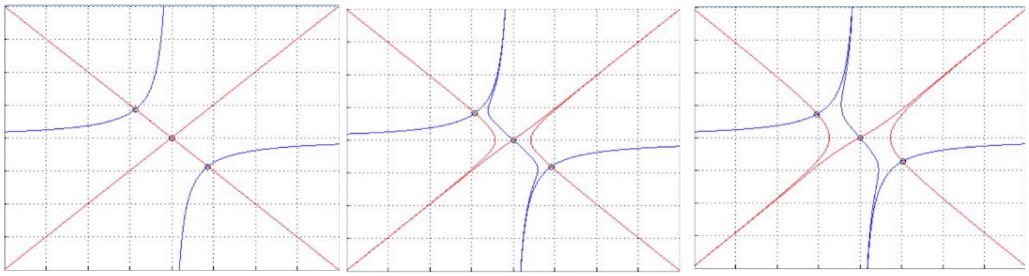

Figure 4.1: ϕ^4 model: thimble structure at different values of σ_R. These figures show the critical points (black circles) and the attached stable thimbles (blue solid lines) and unstable thimbles (red solid lines). Parameters used are $\lambda = 2.0$, $\sigma_I = 0.75$.

Critical points are represented by the black circles, while stable and unstable thimbles are represented respectively by the blue and red solid lines.

For positive values of σ_R the unstable thimbles attached to the critical points $\phi_\pm$ do not cross the original domain of integration (that is the real axis, $Im(\phi) = 0$). Therefore the thimbles $\mathcal{J}_\pm$ have a zero intersection number and do not enter the thimble decomposition. The thimble $\mathcal{J}_0$, attached to the critical point ϕ_0, is the only thimble entering the thimble decomposition. The intersection numbers are $n_0 = 1, n_\pm = 0$.

As σ_R is lowered, the thimble structure changes. For positive values of σ_R the stable thimble $\mathcal{J}_0$ attached to ϕ_0 acts as a barrier for the unstable thimbles $\mathcal{K}_\pm$ attached to $\phi_\pm$. These can never intersect the original domain, since in order to do that they would have to cross $\mathcal{J}_0$. But clearly this cannot happen, since the imaginary part of the action is different at the critical points $\phi_\pm$ and ϕ_0.

At $\sigma_R = 0$ the imaginary part of the action is the same on $\phi_\pm$ and ϕ_0 and a Stokes phenomenon takes place. After the Stokes, for negative values of σ_R, the unstable thimbles attached to all three critical points cross the original domain. All the thimbles enter the thimble decomposition, with intersection numbers $n_0 = -1, n_\pm = 1$ [37].

So far we have identified a region, the one in which $\sigma_R > 0$, where only one thimble enters the thimble decomposition. This is the thimble attached to ϕ_0. But this is not the end of the story. For $\phi_\pm$ one has that

$$\begin{cases} x^2 - y^2 = -\frac{\sigma_R}{\lambda} \\ xy = -\frac{\sigma_I}{2\lambda} \\ x^4 + y^4 = (x^2 - y^2)^2 + 2x^2y^2 = \left(\frac{\sigma_R}{\lambda}\right)^2 + 2\left(\frac{\sigma_I}{2\lambda}\right)^2 \end{cases} .$$

It follows that the real part of the action at $\phi_\pm$ is given by

$$S_R(\phi_\pm) = \frac{1}{4}\frac{\sigma_I^2 - \sigma_R^2}{\lambda} .$$

On the other hand, at ϕ_0 one has that

$$S_R(\phi_0) = 0 .$$

The Gaussian weight of $\mathcal{J}_\pm$ can be estimated as

$$W = \frac{2e^{-S_R(\phi_\pm)}}{2e^{-S_R(\phi_\pm)} + e^{-S_R(\phi_0)}} = \frac{1}{1 + \frac{e^{-S_R(\phi_0)}}{2e^{-S_R(\phi_\pm)}}} = \frac{1}{1 + \frac{1}{2}e^{\frac{1}{4}\frac{\sigma_I^2 - \sigma_R^2}{\lambda}}}$$

It follows that for $\sigma_R \ll 0$ the contribution from $\mathcal{J}_0$ is exponentially depressed. Moreover, the critical points $\phi_\pm$ give conjugate contributions. Therefore we have identified another region, the one in which $\sigma_R \ll 0$, where only one thimble gives a relevant contribution in the thimble decomposition. This is the thimble $\mathcal{J}_\pm$ attached to the critical point $\phi_\pm$.

Now we can pick at least two points in the *good* regions, specifically one point such that $\sigma_R \gtrsim 0$ and one point such that $\sigma_R \ll 0$. Then we can Taylor expand the observables around these points in order to reach the *bad* region $\sigma_R \lesssim 0$. In practice a Padé interpolation of the Taylor coefficients computed at different points works better in bridging the *good* regions than using the different Taylor series separately.

Fig. 4.2 shows the numerical results obtained by applying the Taylor expansion (on thimbles) method to the ϕ^4 model.

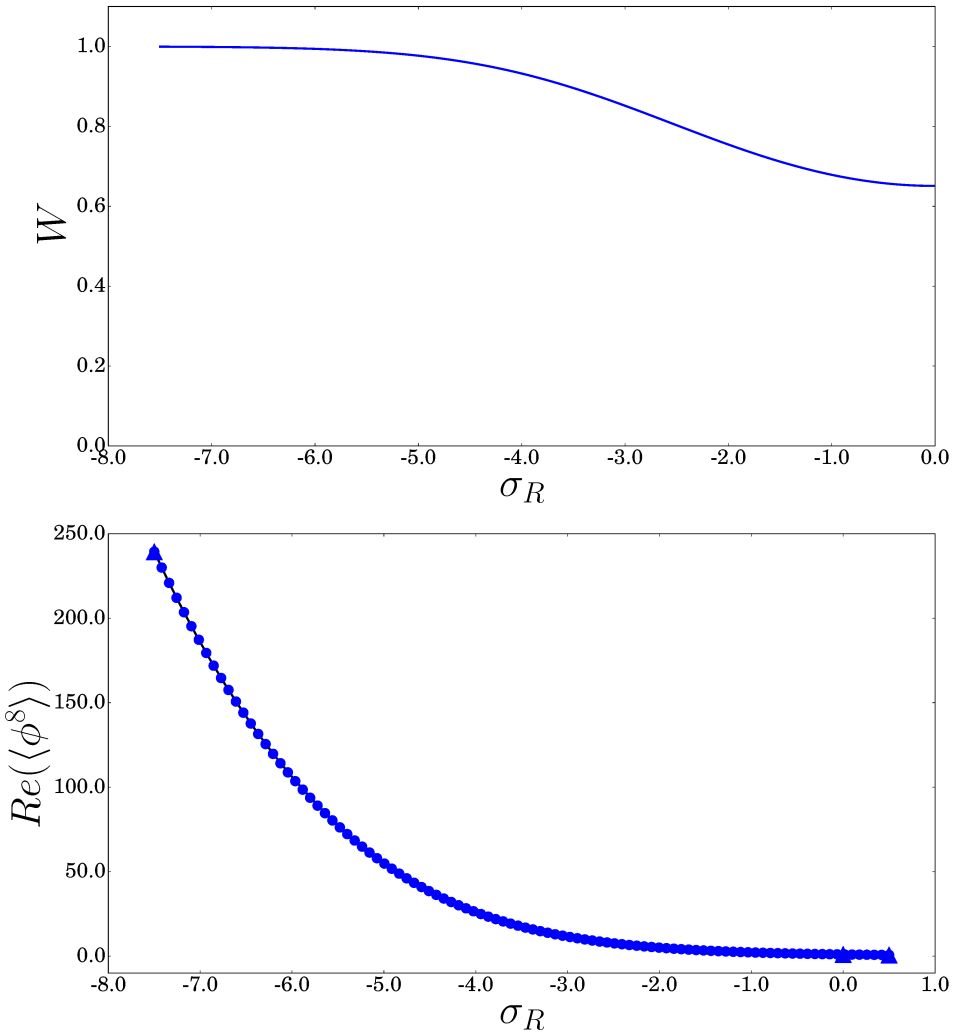

Figure 4.2: ϕ^4 model: the top figure shows the Gaussian estimate for the weight of $\mathcal{J}_\pm$ as a function of σ_R. The bottom figure shows the numerical results from the Padé interpolation for $\langle\phi^8\rangle$ (blue points), the expansion points $\sigma_R = -7.5, 10.0^{-6}, 0.5$ (blue triangles) and the analytical solution (black solid line). Parameters used are $\lambda = 2.0$, $\sigma_I = 0.75$.

We have studied the observable $\langle\phi^8\rangle$. As expansion points we chose $\sigma_R = -7.5, 10.0^{-6}, 0.5$. The first critical point lies in the region $\sigma_R \ll 0$, the second critical point is located close to 0 but in the region $\sigma_R > 0$, the third critical point is located in the region $\sigma_R > 0$ as well. The top figure shows the weight of $\mathcal{J}_\pm$ in the Gaussian approximation. At $\sigma_R = -7.5$ the contribution from $\mathcal{J}_0$ is already exponentially depressed. At $\sigma_R = 10.0^{-6}, 0.5$, being these positive values, $\mathcal{J}_0$ is the only thimble having a non-zero intersection number. The Taylor coefficients for $\langle\phi^8\rangle$ have been computed respectively up to orders $3, 3, 2$ from simulations on the dominant thimble (which in this case is not the same thimble for all the expansion points). The bottom figure shows the results we have obtained from a Padé interpolation of the Taylor coefficients. These are displayed as blue points and they are found to be in very good agreement with the analytical solution (the black solid line).

All in all the procedure we propose to by-pass the need for multi-thimble simulations amounts to:

1. finding multiple, disjoint regions in the parameters space of the theory where the one-thimble approximation is valid. These can either be regions where only one thimble has a non-zero integer number or they can be regions where more than one thimble have a non-zero integer numbers but only one thimble, out of these, gives a relevant contribution;

2. choosing a given number of points from the abovementioned regions and computing Taylor series expansions for the observables around these points. The Taylor coefficients can be calculated from one-thimble simulations;

3. extrapolating the values of the observables outside of the regions identified at step 1 from the Taylor expansions around different points calculated at step 2. Using a Padé interpolation of the Taylor coefficients, instead of using the Taylor expansions separately, might improve the convergence properties of the series.

Here we are assuming the observables to be continuous so that the region after a Stokes phenomenon can be reached by a Taylor expansion around a point located before the Stokes. The key point to stress out is that Stokes phenomena encode discontinuities in the thimble decomposition, but a discontinuity in the thimble decomposition does not imply a discontinuity in the observable.

While it is true is that in specific cases observables can be discontinuous, for instance in presence of a phase transition, this is unrelated to the discontinuity of the thimble decomposition. Even in such cases the Taylor expansion on thimbles method could in principle be applied separately in the two regions before and after the discontinuity.

In the following we will show that this method can be applied to theories other than the ϕ^4 toy model, specifically we show that it can be applied to the two theories we have considered as use cases in the previous chapter: the one-dimensional Thirring model and heavy-dense QCD.

4.2 Case study 1 - the one-dimensional Thirring model

Let's consider again the one-dimensional Thirring model, whose lattice action can be defined as

$$S = \beta \sum_{n=1...L} (1 - cos(\phi_n)) - log\ detD\ ,$$

$$\text{with } detD = \frac{1}{2^{L-1}} \left(cosh(L\hat{\mu} + i \sum_n \phi_n) + cosh(L\ asinh(\hat{m})) \right)\ .$$

We start by studying the case $L = 8, \beta = 1, m = 2$. As we saw in chapter 3, this case has been studied by one-thimble simulations in ref. [42], where the authors have shown that the one-thimble approximation is valid for low and high chemical potentials, but it fails for intermediate chemical potentials. In this region one-thimble simulations yielded the wrong results. Our goal is to show that by making use of Taylor expansions we can recover the correct results from one-thimble simulations also in this intermediate region.

Firstly we need to identify at least two suitable expansion points where the one-thimble approximation holds. A suitable expansion point close to $\frac{\mu}{m} = 0$ can be singled out by a simple argument. Let's define $S_I(\mathbb{R})$ as the values of the imaginary part of the action attained on the original domain of integration. Up to a threshold value μ_0 of the chemical potential there are only two critical points where the imaginary action takes a value $\in S_I(\mathbb{R})$. Therefore these are the only two critical points, which we denote by σ_0 and $\sigma_{\bar{0}}$, whose unstable thimble can intersect the original domain. The contribution from the thimble $\mathcal{J}_{\bar{0}}$ is depressed with respect to the contribution from the thimble $\mathcal{J}_0$ because the real part of the action on the critical point $\sigma_{\bar{0}}$ is much larger than on the critical point σ_0. The fact that $\mathcal{K}_0$ does indeed intersect the original domain of integration can be verified by inspection in fig. 4.3 (top). The figure shows the thimble structure of the Thirring model at $\frac{\mu}{m} = 0.4$. Critical points are depicted by the green points, while stable and unstable thimbles are depicted by the blue and magenta solid lines. The red points represent the fermion determinant zeros: at these points the real part of the action diverges, thus they are a possible endpoint for the stable thimbles. The critical point σ_0 is the one sitting close to $z = 0$. Note that thimbles are L-dimensional manifolds and what is actually shown in fig. 4.3 is a cross-section of the manifolds within the uniform fields subspace. We conclude that for $\frac{\mu}{m} < \mu_0$, and specifically at $\frac{\mu}{m} = 0.4$, only one thimble gives a relevant contribution, this is the thimble $\mathcal{J}_0$ attached to the critical point σ_0. We chose $\frac{\mu}{m} = 0.4$ as the first expansion point.

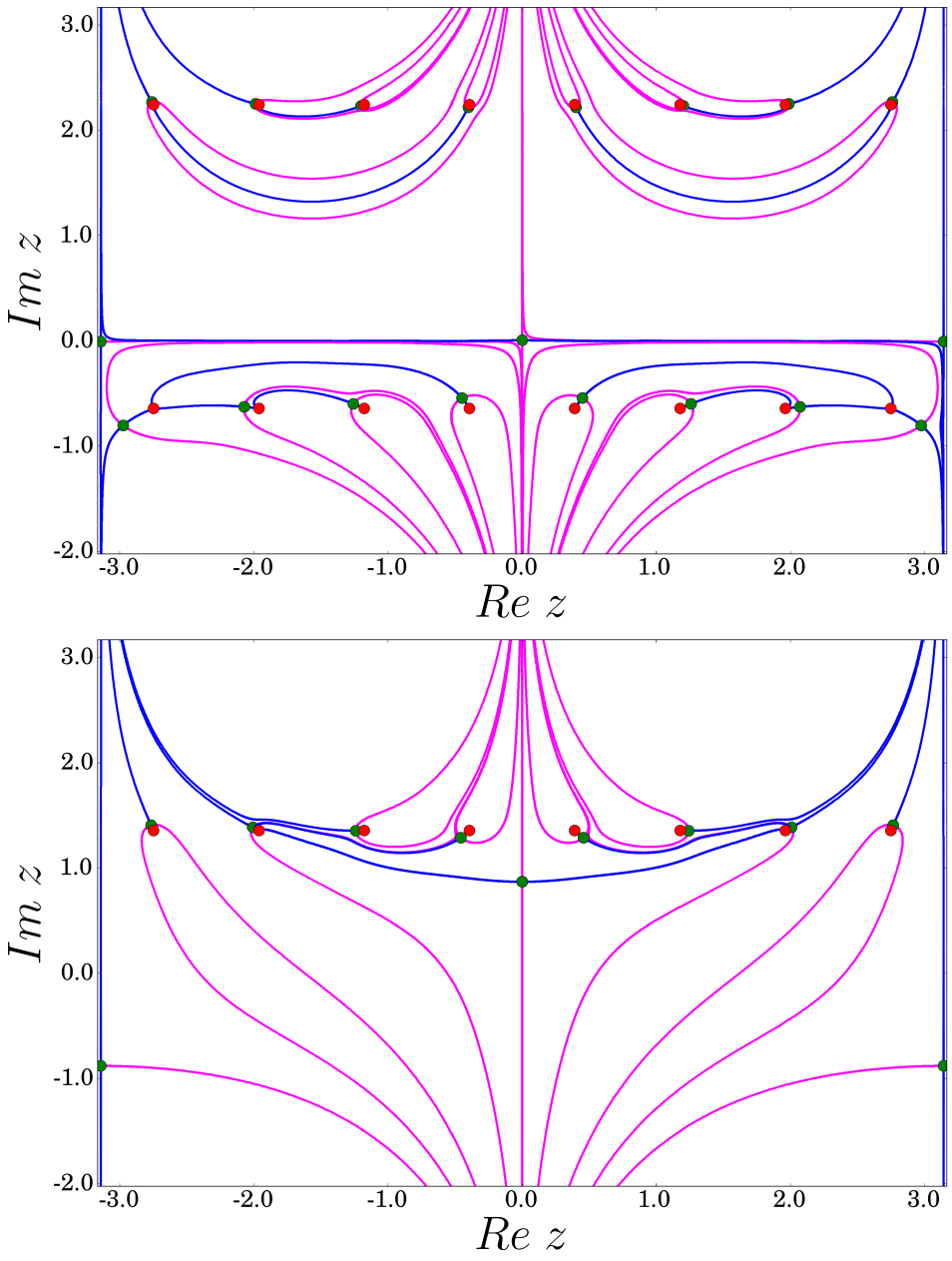

Figure 4.3: Thirring model: thimble structure at $\frac{\mu}{m} = 0.4$ (top) and $\frac{\mu}{m} = 1.4$ (bottom). These figures display the critical points (green points), the stable thimbles (blue solid lines) and the unstable thimbles (magenta solid lines). Also shown are the fermionic determinant zeros (red points). Parameters used are $L = 8, \beta = 1, m = 2$.

As a second expansion point we chose $\frac{\mu}{m} = 1.4$. For this choice of the chemical potential all points but three, which we denote by $\sigma_1, \sigma_{\bar{1}}$ and $\sigma_{\bar{2}}$, have a real part of the action $S_R \gg S_R(\sigma_0)$. Therefore their contributions are depressed. At two out of these three critical points ($\sigma_{\bar{1}}$ and $\sigma_{\bar{2}}$) one has that $S_R < min(S_R(\mathbb{R}))$, where we denoted by $min(S_R(\mathbb{R}))$ the minimum value of the real part of the action attained on the original domain of integration. Therefore the unstable thimbles attached to these critical points cannot intersect the original domain. The unstable thimble attached to the critical point σ_1 does not intersect the original point, as can be checked by inspection in fig. 4.3 (bottom). The critical point σ_0 is the one sitting close to $z = 0$, the critical point σ_1 is the one immediately on the left. The unstable thimble $\mathcal{K}_1$ does not intersect the original domain, while the unstable thimble $\mathcal{K}_0$ does intersect. We conclude that also at $\frac{\mu}{m} = 1.4$ the contribution from the dominant thimble $\mathcal{J}_0$ attached to σ_0 is the only relevant contribution.

The same arguments used for $\frac{\mu}{m} = 0.4, 1.4$ can be used to show that the one-thimble approximation is valid at $\frac{\mu}{m} = 0.0, 1.8$ as well. At $\frac{\mu}{m} = 0.4, 1.4$ we have computed the Taylor coefficients respectively up to order 2 and 5 for the chiral condensate. The coefficients up to order 3 have been computed directly from expectation values of composite operators,

- $c_0 = \langle \bar{\chi}\chi \rangle$
- $c_1 = \frac{\partial \langle \bar{\chi}\chi \rangle}{\partial \hat{\mu}} = -L\langle \bar{\chi}\chi \rangle \langle n \rangle$
- 2! $c_2 = \frac{\partial^2 \langle \bar{\chi}\chi \rangle}{\partial \hat{\mu}^2} = 2L^2 \langle \bar{\chi}\chi \rangle \langle n \rangle^2 - L^2 \langle \bar{\chi}\chi \rangle \langle n^2 \rangle - L\langle \bar{\chi}\chi \rangle \langle n' \rangle$
- 3! $c_3 = \frac{\partial^3 \langle \bar{\chi}\chi \rangle}{\partial \hat{\mu}^3} = -6L^3 \langle \bar{\chi}\chi \rangle \langle n \rangle^3 + 6L^3 \langle \bar{\chi}\chi \rangle \langle n \rangle \langle n^2 \rangle + 6L^2 \langle \bar{\chi}\chi \rangle \langle n \rangle \langle n' \rangle + -3L^2 \langle \bar{\chi}\chi \rangle \langle nn' \rangle - L^3 \langle \bar{\chi}\chi \rangle \langle n^3 \rangle - L\langle \bar{\chi}\chi \rangle \langle n'' \rangle \ ,$

where the operators $n, n', n'', \bar{\chi}\chi$ are defined as

- $n = \frac{sinh(L\hat{\mu} + i\sum_n z_n)}{cosh(L\hat{\mu} + i\sum_n z_n) + cosh(L\ asinh(\hat{m}))}$
- $n' = L\frac{1 + cosh(L\ asinh(\hat{m}))cosh(L\hat{\mu} + i\sum_n z_n)}{(cosh(L\hat{\mu} + i\sum_n z_n) + cosh(L\ asinh(\hat{m})))^2}$
- $n'' = L^2 \frac{sinh(L\hat{\mu} + i\sum_n z_n)[cosh(L\ asinh(\hat{m}))^2 - cosh(L\ asinh(\hat{m}))cosh(L\hat{\mu} + i\sum_n z_n) - 2]}{(cosh(L\hat{\mu} + i\sum_n z_n) + cosh(L\ asinh(\hat{m})))^3}$
- $\bar{\chi}\chi = \frac{1}{cosh(\hat{m})} \frac{sinh(L\ asinh(\hat{m}))}{cosh(L\hat{\mu} + i\sum_n z_n) + cosh(L\ asinh(\hat{m}))}$.

The Taylor coefficients of order 4 and 5, instead, have been computed from c_3 by finite differences,

$$\frac{df(x)}{dx} \approx \frac{f(x + \frac{h}{2}) - f(x - \frac{h}{2})}{h}$$
$$\frac{d^2 f(x)}{dx^2} \approx \frac{f(x + h) - 2f(x) + f(x - h)}{h^2} \ .$$

In fig. 4.4 (top) we illustrate the results from a Padé interpolation of the Taylor coefficients at $\frac{\mu}{m} = 0.4, 1.4$ and the asymptotic conditions for the condensate at $\frac{\mu}{m} = 0.0, 1.8$.

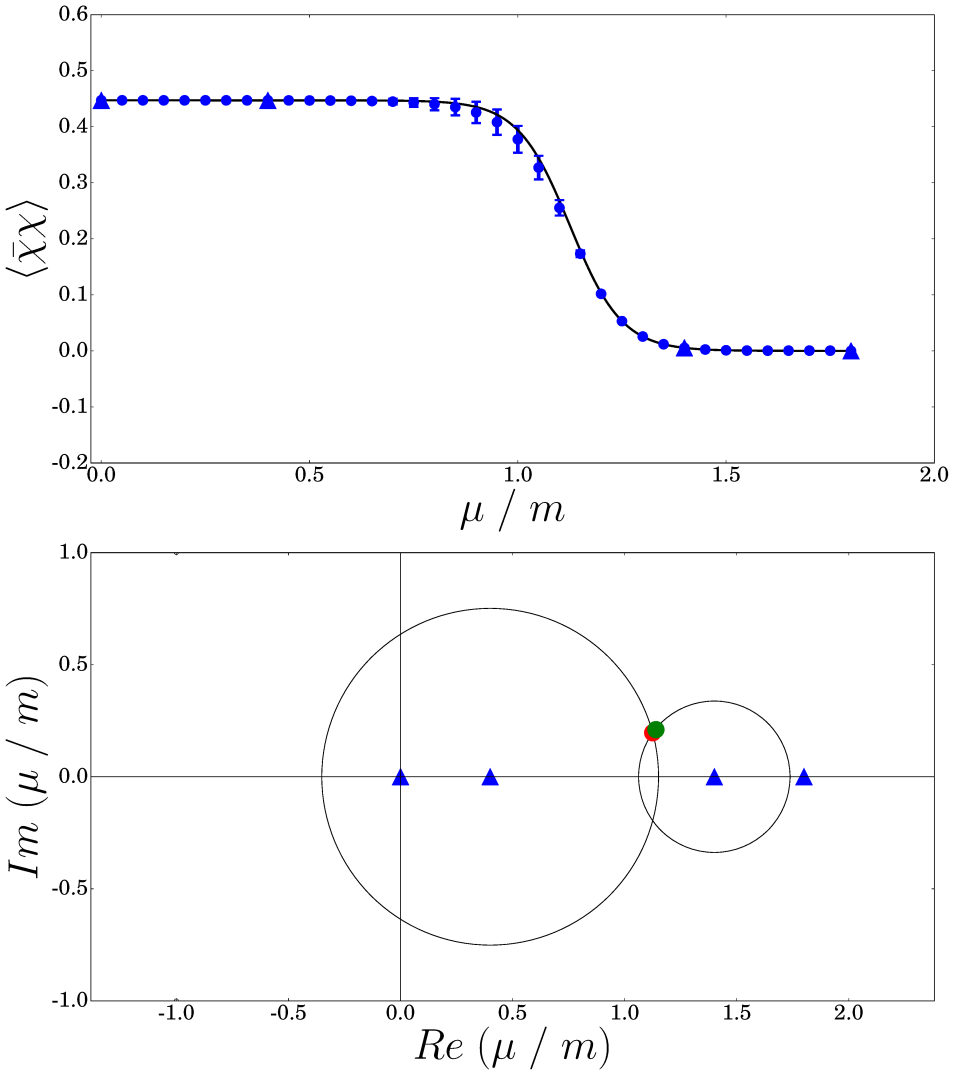

Figure 4.4: Thirring model: the top figure shows the results from the Padé interpolation of the Taylor coefficients computed at $\frac{\mu}{m} = 0.4, 1.4$ by one-thimble simulations. Expansions points are marked as blue triangles, numerical results as blue error bars, analytical results as a black solid line. The bottom figure shows the true singularity of the observable in the complex plane (red point) as well as the pole resulting from the interpolation (green point). Parameters used are $L = 8, \beta = 1, m = 2$.

The expansion points are depicted by blue triangles. The numerical results from the interpolation, shown as blue error bars, match very well the analytical solution, shown as a black solid line. Statistical errors have been estimated by a Jackknife procedure. Note that the error bars obtained for $L = 8$ from Taylor expansions on the dominant thimble are smaller than the ones we have obtained from multi-thimble simulations for $L = 4$.

In fig. 4.4 (bottom) we show both the pole resulting from the interpolation (green point) and the true singularity of the observable (red point) in the complex plane. From the Padé interpolation we could get some information about the analytical structure of the observable. The almost exact location of the true singularity of the observable is recovered. This information is interesting for two reasons. On one hand it shows that by a single Taylor expansion around 0 one could not hope to reach the entire range in μ that we have investigated. The reason is that the series has a finite radius of convergence $r \approx 1$. On the other hand it provides a consistency check for our results: since the radii of convergence of the series at $\frac{\mu}{m} = 0.4, 1.4$ cover the entire range in μ, we have obtained a legitimate analytical continuation of the two Taylor series.

After simulating the theory for $L = 8, \beta = 1, m = 2$, we also carried out a continuum limit analysis. For this theory moving towards the continuum limit means increasing L while keeping constant $L \cdot m$ and $\frac{L}{\beta}$. We varied L from 8 to 64. In particular the parameters we have used for the continuum limit analysis are:

- $L = 8, \beta = 1, m = 2$
- $L = 16, \beta = 2, m = 1$
- $L = 32, \beta = 4, m = 0.5$
- $L = 64, \beta = 8, m = 0.25$.

Numerical results are shown in fig. 4.5. Numerical results are marked by colored error bars, where different colors correspond to different lattice sizes. In all cases they are in good agreement with the analytical results, displayed by the black solid lines. Statistical errors remained under control as we increased the lattice size.

In fig. 4.6 we also show, for each lattice, how the Padé interpolant converges to the correct solutions as we increase the number of constraints we provide as inputs for the interpolation. The pairs of integer numbers $N - M$ displayed in the legends are the maximum order of the Taylor coefficients we have computed respectively for the expansion point on the left (N) and the one on the right (M). The expansion points, as well as the two additional points we have used to constrain the asymptotic value of the observable, are once again marked as triangles. Both the orders N and M have been increased by 1 at each step, except for the highest order interpolations performed for $L = 32, 64$. In these cases M has been increased by 1 but we have provided a third additional point (where we constrained the value of the observable) instead of increasing N.

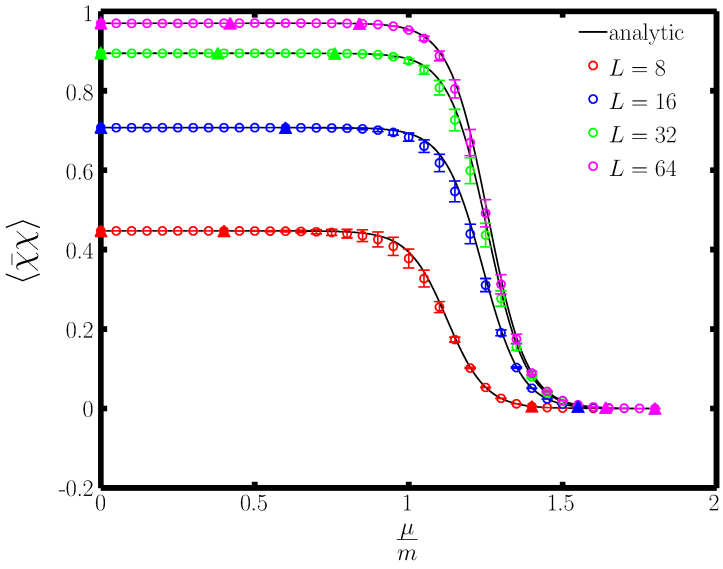

Figure 4.5: Thirring model: results towards the continuum limit. Numerical results are shown as colored points, while analytical solutions are shown as black solid lines. Different colors correspond to different lattices. Parameters used are $L = 8, 16, 32, 64$, $\frac{L}{\beta} = 8$, $L \cdot m = 16$.

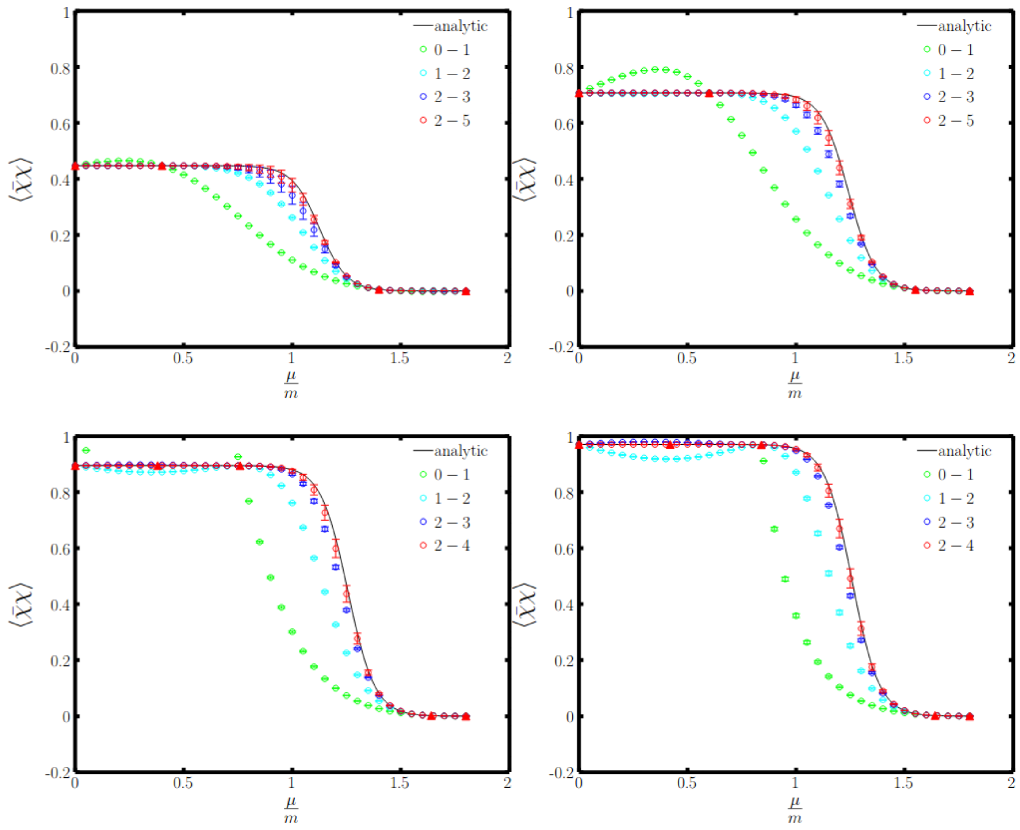

Figure 4.6: Thirring model: convergence of the Padé approximants as the order of the polynomials in the rational functions is increased. Parameters used are $L = 8, 16, 32, 64$, $\frac{L}{\beta} = 8$, $L \cdot m = 16$.

4.3 Case study 2 - heavy-dense QCD

Let's now go back to the simple version of heavy-dense QCD that we discussed previously. The lattice action is

$$S = -2\sum_x ln\left(1 + h_1 TrW_x + h_1^2 TrW_x^\dagger + h_1^3\right) \ ,$$

where $h_1 \approx (2ke^\mu)^{N_t}$, k is the hopping parameters, W_x is the Polyakov loop at the spatial site x. The critical points for this theory are mixtures of center elements of $SU(3)$. The action depends on the chemical potentials through the parameter $h_1 = e^{\frac{\mu - m}{T}}$. This is the natural expansion parameter that we are going to use for the Taylor expansion. We choose as parameters $k = 0.0000887$ and $N_t = 116$ and we use a lattice with $N_{sites} = 2^3$ sites. We want to study the observable quark number density $\langle n \rangle$ as a function of the chemical potential. This is a different situation than the one we've encountered with the Thirring model. In the case of the Thirring model we had two regions at our disposal where the one-thimble approximation works. These were the regions at low and at high chemical potentials. For heavy-dense QCD the one-thimble approximation only works in one region, the region $h_1 \approx 1$ corresponding to $\mu \approx m$. However we know the asymptotic conditions for $\langle n \rangle$, for $\mu \to 0$ ($h_1 \to 0$) the number density vanishes while for $\mu \to \infty$ ($h_1^{-1} \to 0$) the number density saturates to $2N_c$.

We study the branches $h_1 \leq 1$ and $h_1 \geq 1$ separately. For the left branch we choose $\frac{\mu}{m} = 0.9995, 1.0000$ as expansion points and we Taylor expand in h_1. For the right branch we choose $\frac{\mu}{m} = 1.0000, 1.0005$ and we Taylor expand in h_1^{-1}.

At the expansion points the one-thimble approximation is expected to work, because the weights of the thimbles other than the fundamental one are depressed. Consider for instance fig. 4.7 which shows an histogram of the Gaussian weights of the critical points at $\frac{\mu}{m} = 0.9995$. The only appreciable bar is the one associated to the fundamental thimble (the one attached to the critical points where there is an identity matrix at each site of the lattice).

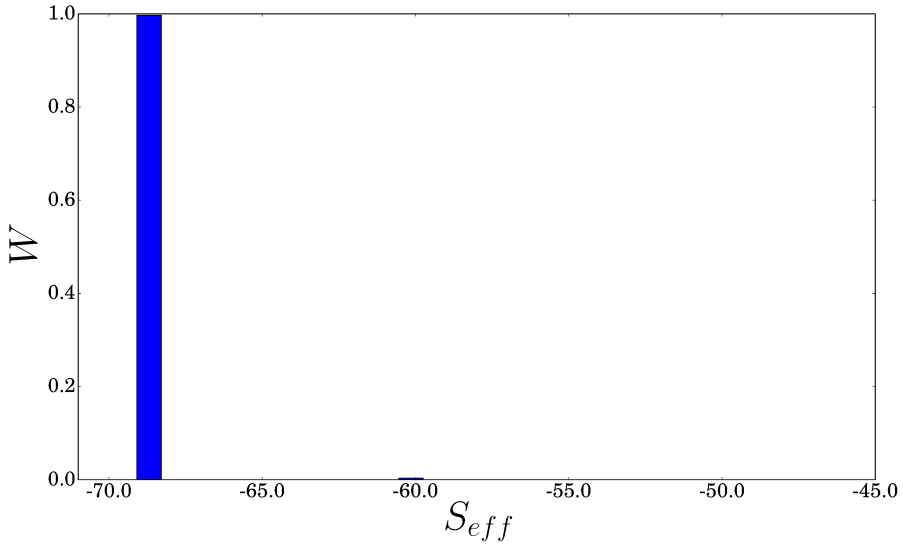

Figure 4.7: Heavy-dense QCD: Gaussian weights for $N_{sites} = 2^3$. Parameters used are $N_t = 116$, $k = 0.0000887$, $\frac{\mu}{m} = 0.9995$.

We computed the Taylor coefficients up to order 2, 1 respectively at $\frac{\mu}{m} = 0.9995$ and 1.0000 for the left branch and at $\frac{\mu}{m} = 1.0005$ and 1.0000 for the right branch. The Taylor coefficients for the left branch can be expressed in terms of the derivatives with respect to the chemical potential in lattice units,

- $c_0 = \langle n \rangle$
- $c_1 = \frac{\partial \langle n \rangle}{\partial h_1} = \frac{1}{N_t h_1} \frac{\partial \langle n \rangle}{\partial \mu}$
- 2! $c_2 = \frac{\partial^2 \langle n \rangle}{\partial h_1^2} = \frac{1}{(N_t h_1)^2} (\frac{\partial^2 \langle n \rangle}{\partial \mu^2} - N_t \frac{\partial \langle n \rangle}{\partial \mu})$.

Similar formulas are obtained for the right branch, where the expansion is done in $y \equiv h_1^{-1}$,

- $c_0 = \langle n \rangle$
- $c_1 = \frac{\partial \langle n \rangle}{\partial y} = -\frac{1}{N_t y} \frac{\partial \langle n \rangle}{\partial \mu}$
- 2! $c_2 = \frac{\partial^2 \langle n \rangle}{\partial y^2} = \frac{1}{(N_t y)^2} (\frac{\partial^2 \langle n \rangle}{\partial \mu^2} + N_t \frac{\partial \langle n \rangle}{\partial \mu})$.

The derivatives with respect to the chemical potential are given by

$$\frac{\partial \langle n \rangle}{\partial \mu} = -N_{sites} N_t \langle n \rangle^2 + N_{sites} N_t \langle n^2 \rangle + \langle n' \rangle$$

$$\frac{\partial^2 \langle n \rangle}{\partial \mu^2} = 2(N_{sites} N_t)^2 \langle n \rangle^3 + (N_{sites} N_t)^2 \langle n^3 \rangle - 3(N_{sites} N_t)^2 \langle n \rangle \langle n^2 \rangle +$$
$$+3(N_{sites} N_t) \langle n n' \rangle - 3(N_{sites} N_t) \langle n \rangle \langle n' \rangle + \langle n'' \rangle \ ,$$

where the operators appearing in the formulas are defined as

- $n = \frac{2}{N_{sites}} \sum_z \frac{\left(h_1 TrU_z + 2h_1^2 TrU_z^{-1} + 3h_1^3\right)}{\left(1 + h_1 TrU_z + h_1^2 TrU_z^{-1} + h_1^3\right)}$
- $n' = \frac{2N_t}{N_{sites}} \sum_z \frac{1}{\left(1 + h_1 TrU_z + h_1^2 TrU_z^{-1} + h_1^3\right)^2} \big[h_1 TrU_z + 4h_1^2 TrU_z^{-1} +$
  $(9 + TrU_z TrU_z^{-1}) h_1^3 + 4h_1^4 TrU_z + h_1^5 TrU_z^{-1} \big]$
- $n'' = \frac{2N_t^2}{N_{sites}} \sum_z \frac{1}{\left(1 + h_1 TrU_z + h_1^2 TrU_z^{-1} + h_1^3\right)^3} \big[h_1 TrU_z + h_1^2 (8TrU_z^{-1} - (TrU_z)^2) +$
  $27h_1^3 + h_1^4 ((TrU_z)^2 TrU_z^{-1} + 20TrU_z - 8(TrU_z^{-1})^2) +$
  $+h_1^5 (8(TrU_z)^2 - TrU_z (TrU_z^{-1})^2 - 20TrU_z^{-1}) +$
  $-27h_1^6 + h_1^7 ((TrU_z^{-1})^2 - 8TrU_z) - h_1^8 TrU_z^{-1} \big]$

Fig. 4.8 (top) shows the results of the Padé interpolation of the Taylor coefficients and the asymptotic constraints (for the observable and for its first derivative).

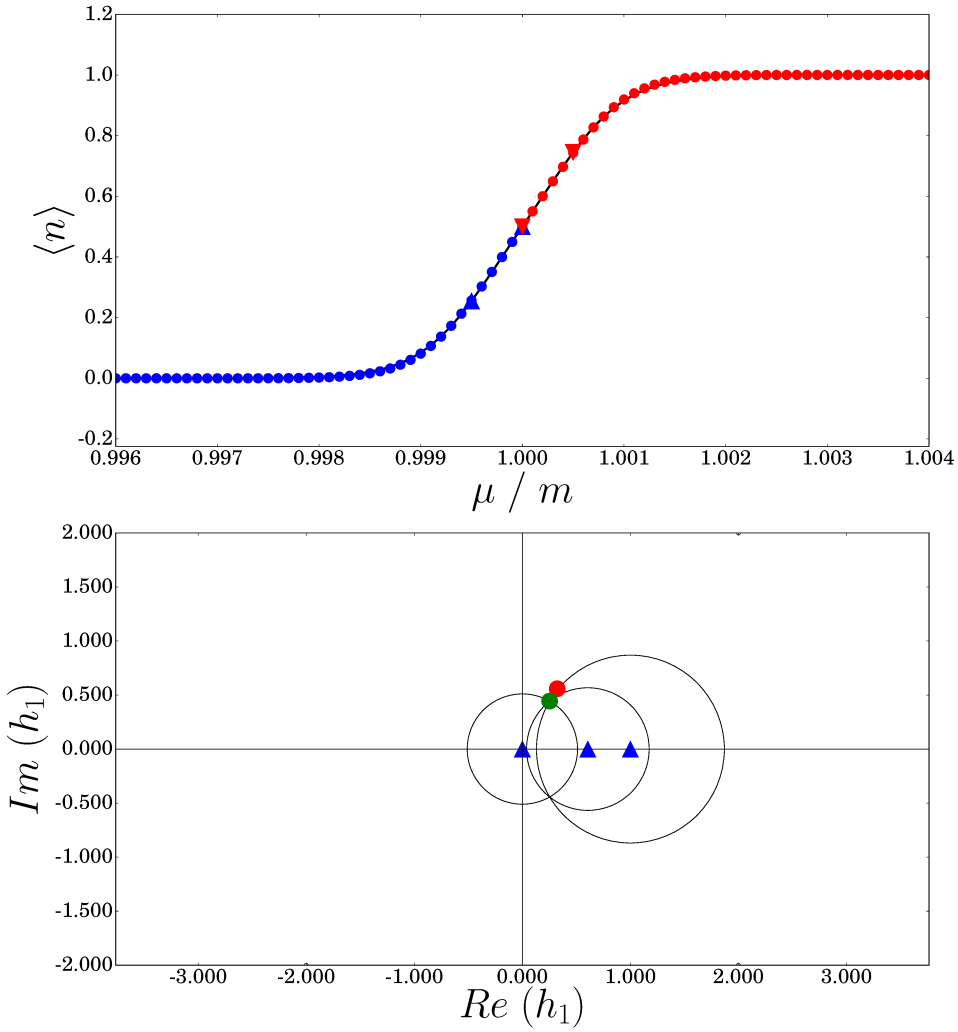

Figure 4.8: Heavy-dense QCD: the top figure illustrates the numerical results from the Padé interpolation (blue points) and the analytical solution (black solid line). Also shown are the expansion points, depicted as triangles. The bottom figure shows the pole resulting from the Padé interpolation for the left branch compared to the true singularity of the observable in the complex plane.

The numerical results are shown as error bars in different colors (blue and red) for the left and right branches. The expansion points are depicted as triangles. Numerical results are found to be in good agreement with the analytical results illustrated by the black solid line.

Fig. 4.8 (bottom) shows the pole resulting from the Padé interpolation for the left branch (green point). The pole approximates reasonably well the true singularity of the observable (red point). Also for this theory the radii of convergence of the series indicate that the analytic continuation resulting from the interpolation is a legitimate one.

4.4 A few comments

The method we discussed is far more powerful than what we saw in the previous chapter. In particular for the case of the Thirring model we saw that we could complete the task of reaching the continuum limit. The case of heavy-dense QCD is a bit more problematic. In particular one cannot enlarge the size of the system indefinitely. The landscape of fig. 3.1 (many critical points providing a significant contribution) is a consequence of combinatorics. There is indeed a handle one can play with and that is the value of $\frac{\mu}{m}$. However the effectiveness of this is limited. This is still a partial success if we compare to what has been done by other methods. Getting so close to $\frac{\mu}{m} = 1$ would enable the use of other tools like reweighting: the combination of "reweighting + Taylor + Padé" would be as good as what we did in this particular case. Notice that this is not the case for Thirring. In that case the procedure relied on a value of $\frac{\mu}{m}$ that would be unaccessible to other methods. All in all one could say: we learned that the combination of "X + Taylor + Padé" can be a fruitful strategy, where "X" is a calculation method which is good enough in a given region, provided the region we have access to is good enough to get an effective description by Padé. In the next chapter we will see an application relying on right this strategy.

Chapter 5

Taylor expansion for QCD at imaginary μ and Padé approximants

In this section we discuss how Padé approximants can be used to investigate the QCD phase diagram by interpolating Taylor coefficients calculated at imaginary chemical potentials.

5.1 Taylor expansion for QCD at imaginary μ

In the previous chapter we proposed to look for different points in the parameters space of a theory where the one-thimble approximation holds and to carry out Taylor expansions around these points. Taylor coefficients can be computed from one-thimble simulations. A Padé interpolation of such coefficients provides an analytic continuation for the Taylor series centered around the different points. We have shown that Padé approximants not only allow to reach by one-thimble simulations regions where the one-thimble approximation does not hold, but they also allow to capture information about the analytic structure of the observables. In the two use cases we have considered, we could reconstruct the true singularities of the observables in the complex plane. A natural question is whether Padé approximants can be a useful tool to hunt for critical points in the QCD phase diagram. In particular an open problem in physics is the determination of the location of the critical endpoint where the deconfinement/chiral restoration phase transition line, which is a crossover at low chemical potentials, becomes first-order.

Taylor coefficients around $\mu = 0$ can be extracted from standard lattice simulations since at zero chemical potential there is no sign problem. Hopefully thimble regularization could be helpful in providing a second expansion point at some $\mu > 0$ where to calculate additional Taylor coefficients that can be used as inputs for the Padé interpolation. Admittedly for now the application of thimble regularization to full QCD is still a work in progress. However we can come back to the strategy we described at the end of the previous chapter. Much in that spirit we can investigate a region of the QCD phase diagram where there is no sign problem (and thimble regularization is not needed), namely the region of the phase diagram at purely imaginary chemical potential. The big question is whether "imaginary μ + Taylor + Padé" is good enough to reconstruct singularities in the QCD phase diagram.

This project has been started in collaboration with the group led by dr. Christian Schmidt in Bielefeld. This has been done in the framework of the EuroPLEx research network [51].

5.2 Case study 1 - thermal singularities

Let's denote by $\mu_{B,I}$ the imaginary part of the baryon chemical potential. A qualitative picture of the $(\frac{\mu_{B,I}}{T}, T)$ phase diagram of QCD is illustrated in fig. 5.1.

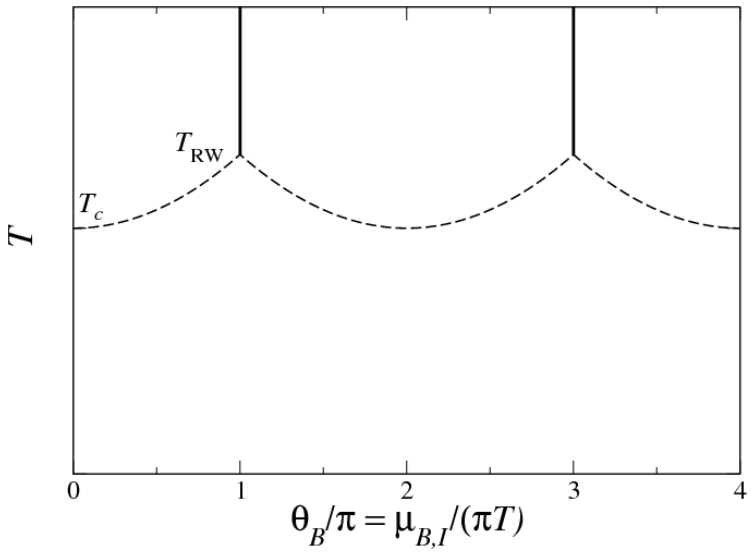

Figure 5.1: QCD at imaginary μ: qualitative picture of the $(\frac{\mu_{B,I}}{T}, T)$ phase diagram. Image from ref. [52].

On the y and x axes we have respectively the temperature T and the imaginary part of the baryon chemical potential divided by πT. The vertical black solid lines are two first order phase transition lines, which separate Z_3 sectors characterized by different phases φ of the Polyakov loop $(L(\vec{x}) = |L(\vec{x})|e^{i\varphi})$. The dashed curve is the analytic continuation of the pseudocritical chiral transition line. The RW transition lines join the chiral crossover line at the RW endpoints. The first RW endpoint is located at $(\frac{\mu_{B,I}}{T}, T) = (\pi, T_{RW})$. We wanted to check whether we were able to find out the location of this critical endpoint by studying the poles resulting from the Padé approximation of a suitable observable.

We used the baryon number density $\langle n_B \rangle$ as a probe to investigate the phase transition. This is an odd function of the chemical potential and it is purely imaginary at purely imaginary μ. At the Roberge-Weiss transition line this observable is expected to be discontinuous.

Simulations have been performed on $24^3 \times 4$ lattices using the HISQ action relying on a slight modification of a GPU-based code developed by the Bielefeld group.

We computed the Taylor coefficients of $\chi_B^1 \equiv \frac{\langle n_B \rangle}{T^3}$ up to second order. We repeated the calculations for $O(10)$ chemical potentials at three different temperatures, $T = 160\ MeV$, $176\ MeV$ and $201\ MeV$. The first temperature is close to the pseudocritical temperature T_c, the third one is close to the current estimate for the Roberge-Weiss temperature T_{RW} for $N_t = 4$ [53], the second one is an intermediate temperature between the other two.

β	m_l	m_s
5.760	0.006024	0.1627
5.850	0.005270	0.1424
5.973	0.004396	0.1187

Table 5.1: Lines of constant physics ($N_t = 4$).

$\mu_{l,I}$ ($\beta = 5.760$)	$\mu_{l,I}$ ($\beta = 5.850$)	$\mu_{l,I}$ ($\beta = 5.973$)
0.00000	0.139626	0.00000
0.03272	0.157080	0.03272
0.06545	0.174533	0.06545
0.09817	0.191986	0.09817
0.13090	0.209440	0.13090
0.16362	0.226893	0.16362
0.19635	0.244346	0.19635
0.22907	0.261799	0.22907
		0.23998
		0.25089
		0.25875
		0.26485
		0.27271
		0.28362

Table 5.2: List of chemical potentials ($N_t = 4$).

The lines of constant physics [54] and the values of the light chemical potentials selected for each temperature are reported respectively in tab. 5.1 and tab. 5.2. The strange chemical potential has been set to $\mu_{s,I} = \mu_{l,I} = \frac{\mu_{B,I}}{3}$. For each temperature and each chemical potential a total of ≈ 5000 gauge configurations have been generated and 260 random vectors were used for the measurements.

5.2.1 Algorithmic approaches to the Padé interpolation

The Taylor coefficients obtained from the simulations have been interpolated by a multipoint Padé procedure that we now briefly discuss. For each temperature we start from a set of Taylor coefficients

$$c_j^{(k)} \equiv \frac{1}{j!} \frac{\partial^j \langle O \rangle}{\partial \hat{\mu}_B^j} (\hat{\mu}_B^{(k)}) \ .$$

The $\{\hat{\mu}_B^{(k)} \ , k = 1 \dots N\}$ are N values of the chemical potential divided by T and at each $\hat{\mu}_B^{(k)}$ we have calculated the derivatives of order $j = 0 \dots N_k$. We have investigated two possible approaches to the interpolaton problem.

1. In the first approach we look for a Padé interpolant of the form

$$P_{n,m}(\hat{\mu}_B) = \frac{a_0 + a_1 \hat{\mu}_B + \dots a_n \hat{\mu}_B^n}{1 + b_1 \hat{\mu}_B + \dots b_m \hat{\mu}_B^m}$$

that matches the Taylor coefficients

$$\frac{1}{j!}(\partial^j_{\hat{\mu}_B^j} P_{n,m})(\hat{\mu}_B^{(k)}) = c_j^{(k)} \text{ for } k = 1 \dots N, j = 0 \dots N_k \ .$$

This is a non-linear system of $n+m = \sum_{k=1\dots N}(1+N_k)$ equations with $n+m$ unknowns. The equation system can be solved by a symbolic software suite. However, as the number of constraints (equations) increases, the equation system becomes increasingly more difficult to solve.

2. In the second approach we decrease the number of coefficients in the rational function, thereby simplifying the problem. In this approach the Taylor coefficients are not strictly speaking interpolated, instead they are fitted by minimizing a generalized chi-square,

$$\tilde{\chi}^2 = \sum_{k,j} \left(\frac{||\frac{1}{j!}(\partial^j_{\hat{\mu}_B^j} P_{n,m})(\hat{\mu}_B^{(k)}) - c_j^{(k)}||^2}{||\Delta c_j^{(k)}||^2} \right) \ ,$$

where $n + m < \sum_{k=1\dots N}(1 + N_k)$ and $\Delta c_j^{(k)}$ are the statistical errors for the Taylor coefficients.

The Padé interpolation problem can also be tackled from a different angle. The rational function ansatz is

$$P_{n,m}(\hat{\mu}_B) = \frac{p_n(\hat{\mu}_B)}{q_m(\hat{\mu}_B)} \ ,$$

where p_n and q_m are polynomials respectively of order n and m. Therefore we can write

$$p_n(\hat{\mu}_B) = P_{n,m}(\hat{\mu}_B) q_m(\hat{\mu}_B) \ .$$

By differentiating the left and right hand-sides multiple times we obtain

$$\begin{cases} p_n(\hat{\mu}_B) = P_{n,m}(\hat{\mu}_B) q_m(\hat{\mu}_B) \\ p'_n(\hat{\mu}_B) = P'_{n,m}(\hat{\mu}_B) q_m(\hat{\mu}_B) + P_{n,m}(\hat{\mu}_B) q'_m(\hat{\mu}_B) \\ p''_n(\hat{\mu}_B) = P''_{n,m}(\hat{\mu}_B) q_m(\hat{\mu}_B) + 2P'_{n,m}(\hat{\mu}_B) q'_m(\hat{\mu}_B) + P_{n,m}(\hat{\mu}_B) q''_m(\hat{\mu}_B) \\ \dots \end{cases}$$

When evaluated at the chemical potentials $\hat{\mu}_B^{(k)}$, this is a set of equations involving the derivatives of $P_{n,m}$ evaluated at the potentials $\hat{\mu}_B^{(k)}$. These can be matched to the Taylor coefficients we have obtained from the simulations. This results in a linear system of equations for the coefficients of the rational function ansatz. Unfortunately this linear system is often very ill-conditioned and the accuracy of the solution is limited. Nonetheless the solution of this linearized problem can be used as a thoughtful initial guess for the minimizer in the fit approach.

5.2.2 Numerical results

The data obtained from the simulations for $\chi_B^1 \equiv \frac{\langle n_B \rangle}{T^3}$ and its first derivative with respect to $\hat{\mu}_{B,I}$, χ_B^2, are shown in fig. 5.2. Different symbols and colors correspond to different temperatures. The data shown for $\hat{\mu}_{B,I} > \pi$ have been obtained by symmetrizing/anti-symmetrizing the data for $\hat{\mu}_{B,I} < \pi$. As the temperature is increased, one can see χ_B^1 becoming discontinuous. Accordingly, its first derivative χ_B^2 diverges as we approach $\hat{\mu}_{B,I} = \pi$.

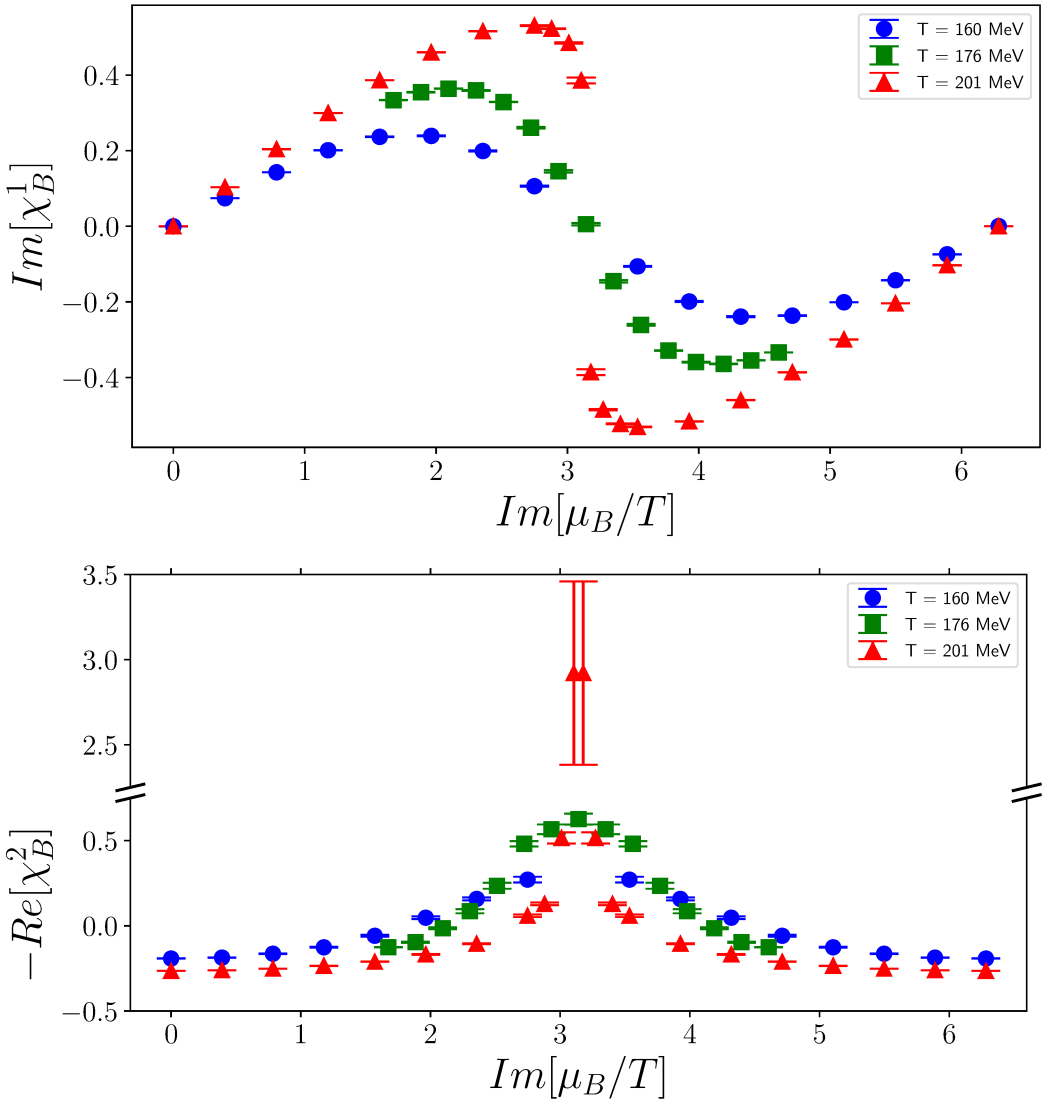

Figure 5.2: QCD at imaginary μ: imaginary part of χ_B^1 (top figure) and real part of its first derivative χ_B^2 (bottom figure) as a function of the chemical potential. Different symbols and colors correspond to different temperatures, $T = 160, 176$ and $201\ MeV$. Parameters used are $N_s^3 \times N_t = 24^3 \times 4$, light and strange quark masses as summarized in tab. 5.1.

The results obtained from the Padé procedure for the lowest temperature $T = 160\ MeV$ are shown in fig. 5.3. The figure shows the imaginary part of χ_B^1 as a function of the imaginary part of the baryon chemical potential. The blue error bars are the results from the simulations. The solid blue line is the result obtained from a Padé fit using the $P_{5,5}$ rational function as ansatz.

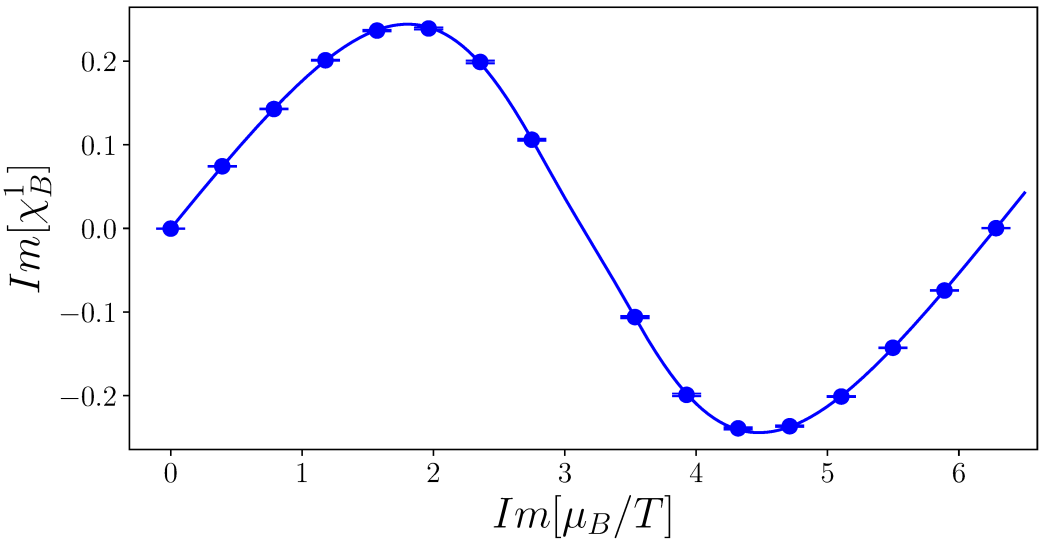

Figure 5.3: QCD at imaginary μ: imaginary part of χ_B^1 as a function of the chemical potential. Parameters used are $N_s^3 \times N_t = 24^3 \times 4$, $\beta = 5.760$ (which corresponds to $T = 160\ MeV$), light and strange quark masses as summarized in tab. 5.1.

Fig. 5.4 (top) shows the zeros of the numerator (red diamonds) and the zeros of the denominator (blue points) in the complex plane resulting from the fit. The chemical potentials used in the simulations are displayed as well (green triangles). A dashed line is drawn at $\hat{\mu}_B = i\pi$.

We observe an almost perfect cancelation for many of the zeros of the numerator with corresponding zeros of the denominator. A pair of stable isolated zeros of the denominator survives at $\hat{\mu}_B \approx i\pi \pm 2.1$. These are genuine poles of the Padé approximant. Two stable isolated zeros of the numerator are found as expected at $\hat{\mu}_B \approx 0, i\pi$, where the baryon density vanishes.

Fig. 5.4 (bottom) illustrates a comparison between the results from the two Padé procedures, the fit and the interpolation approaches. The zeros of the numerator and denominator are marked by different colors. Different symbols are used for the different approaches. Specifically, blue points + red diamonds and cyan asterisks + orange crosshairs are used respectively for the fit and interpolation approaches.

One can see that, while the canceling zero-zero pairs are representation dependent (actually the Padé approximants were of different order), the determination of the expected zeros and of the poles at $\hat{\mu}_B \approx i\pi \pm 2.1$ is quite stable. The small difference in the determinations can be used as an estimate for the systematic uncertainty in the Padé procedure.

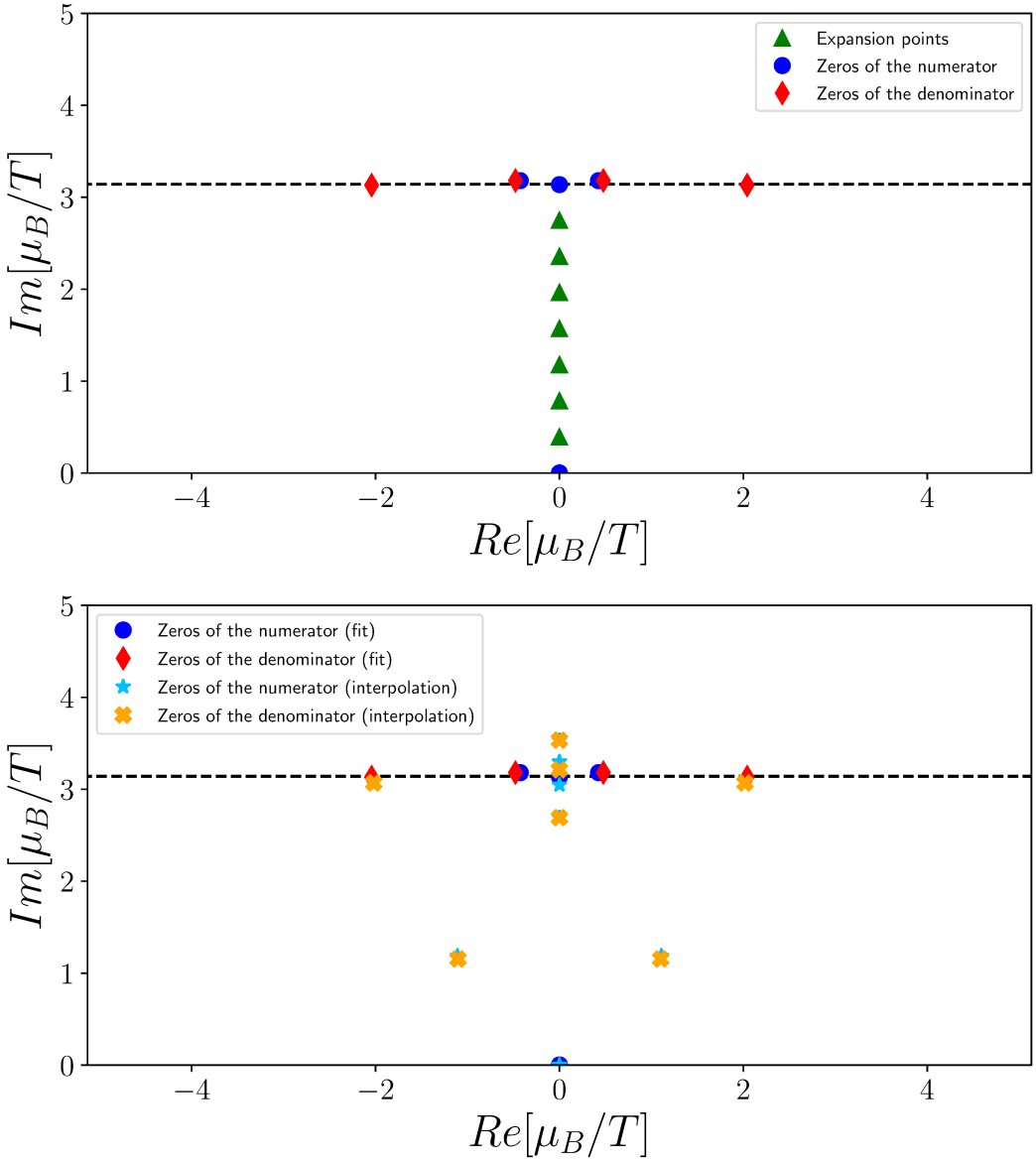

Figure 5.4: QCD at imaginary μ: zeros of the numerator and zeros of the denominator resulting from the Padé procedure applied to the Taylor coefficients of the baryon number density. The zeros of the numerator and denominator are marked respectively by symbols drawn in cold and warm colors. In the bottom picture different symbols are used for the different approaches. Specifically, blue points + red diamonds and cyan asterisks + orange crosshairs are used respectively for the fit and interpolation approaches. The relevant information is the one surviving cancelations (see main text). A dashed line is drawn at $\hat{\mu}_B = i\pi$. The chemical potentials used for the simulations are shown as green triangles in the top figure.

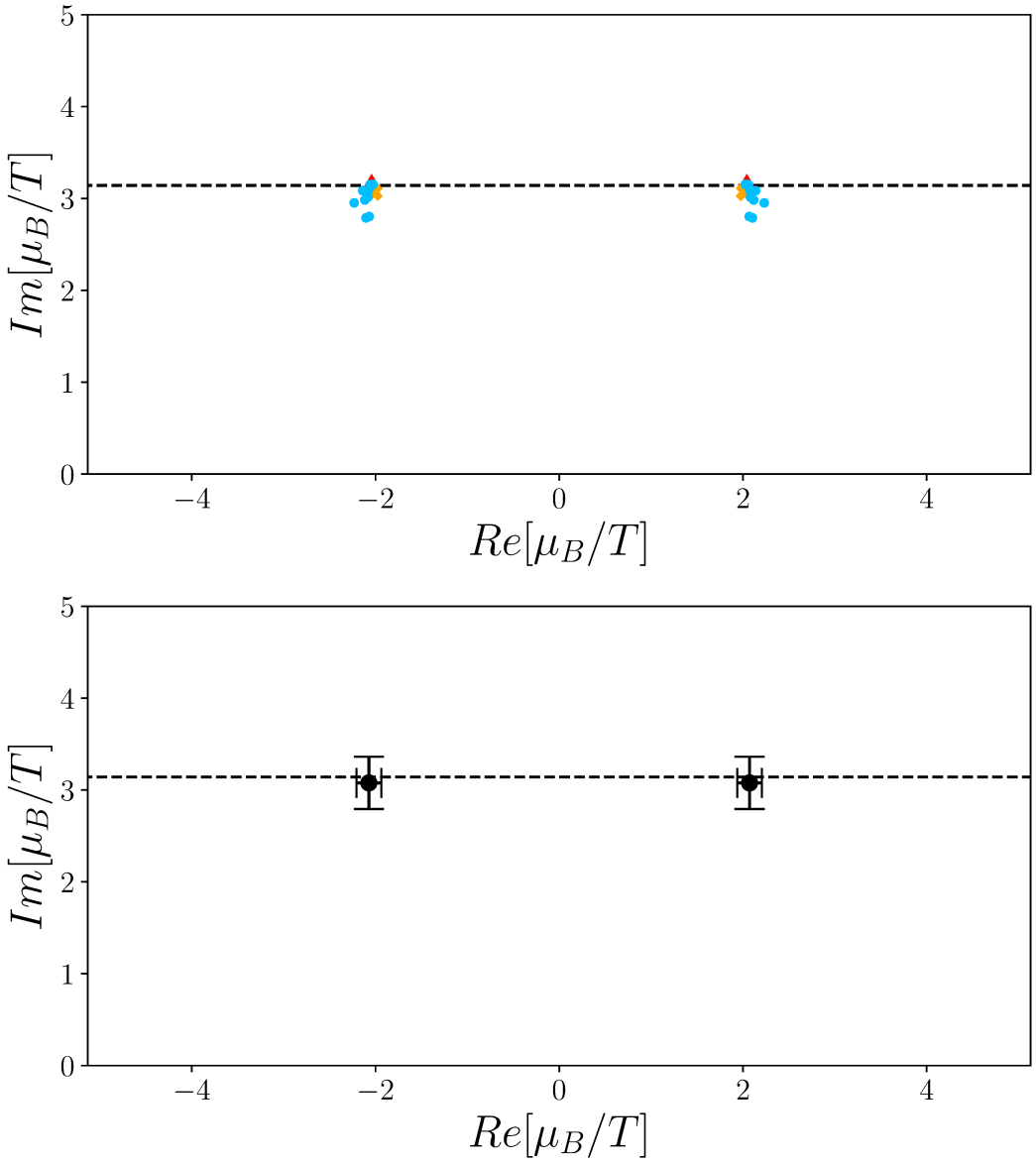

Figure 5.5: QCD at imaginary μ: the top picture shows the genuine poles of the Padé approximants from the fit (red diamonds) and interpolation (orange crosshairs) approaches. On top of these are also shown the poles resulting from a Padé fit of data sampled from a normal distribution having mean equal to the central values of the Taylor coefficients and standard deviation equal to the statistical errors (cyan points). The spread of the results is used to give an estimate for the uncertainty on the determinations (see bottom picture). A dashed line is drawn at $\hat{\mu}_B = i\pi$.

Finally fig. 5.5 (top) shows the genuine poles of the Padé approximants already shown in the bottom picture of fig. 5.4. On top of those are also drawn the determinations obtained by fitting data sampled from a normal distribution having mean equal to the central values of the Taylor coefficients and standard deviation equal to the statistical errors (cyan points). The spread of these results gives an estimate for the combined systematic and statistical uncertainty on the determination of the singularity (see bottom picture of fig. 5.5).

The same analysis has been repeated for the other two temperatures. The stable singularities resulting from the analyses are displayed in fig. 5.6. Different colors correspond to different temperatures. In particular the yellow, orange and red points correspond respectively to the temperatures $T = 160\ MeV$, $176\ MeV$ and $201\ MeV$. Notice that the singularity on the imaginary axis was found not to be a pole, but a branch cut, as expected. This is recognized in the Padé approximants formalism by an accumulation of zeros and poles on a line intersecting the imaginary axis orthogonally (see top picture of fig. 5.7, which depicts the zeros and poles of the Padé approximant for $T = 201\ MeV$).

What we observe is exactly the behaviour that has been conjectured for the so-called thermal singularities[1] of QCD (see refs. [55, 56]): they lie on $\hat{\mu}_B = i\pi$ and they move towards the imaginary axis as the temperature is increased, pinching the imaginary axis at $T = T_{RW}$, where the singularity is no longer a pole, but rather it is a branch cut. Actually by integrating the Padé approximant for the number density we obtain the profile of the free energy whose shape at $\hat{\mu}_B = i\pi$ resembles the expected cusp at the Roberge-Weiss temperature (see bottom picture of fig. 5.7).

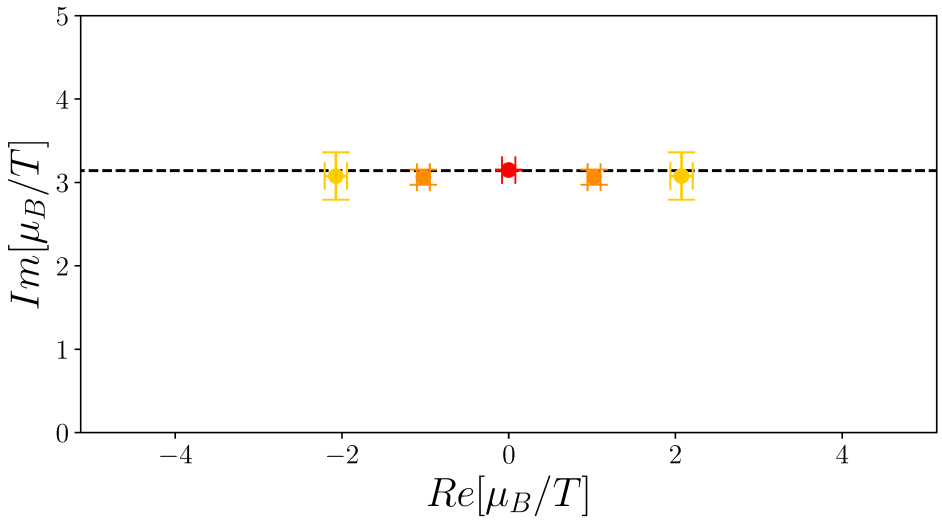

Figure 5.6: QCD at imaginary μ: singularities resulting from the Padé procedure performed at different temperatures. The yellow, orange and red colors correspond respectively to the results obtained at $T = 160\ MeV$, $176\ MeV$ and $201\ MeV$. Singularities show up where they are expected (see the dashed line drawn at $\hat{\mu}_B = i\pi$) [55, 56].

[1] Above the pseudocritical temperature T_c, quarks can be thought as behaving like free particles and their thermodynamics can be reasonably well described by the Fermi-Dirac distribution. The latter features singularities in the complex plane which are known as themal singularities.

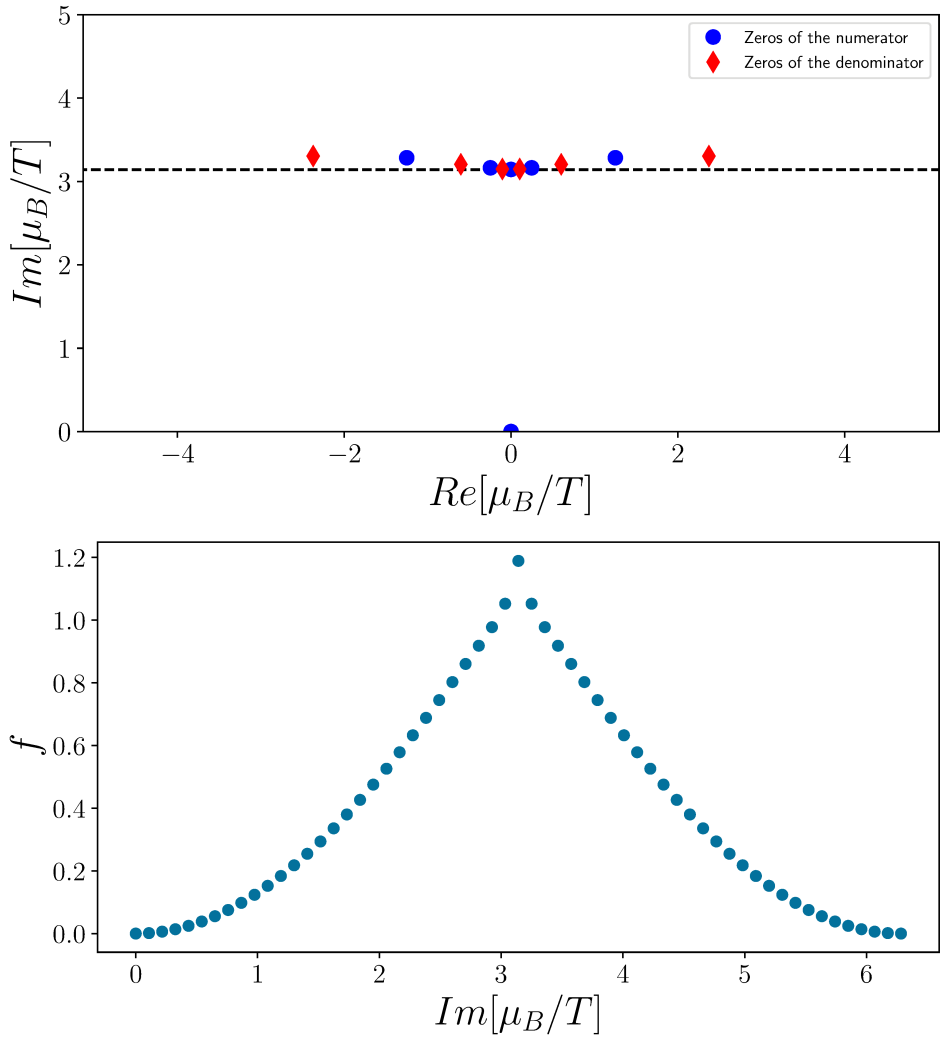

Figure 5.7: QCD at imaginary μ: the top picture shows the accumulation of zeros and poles of the Padé approximant of the baryon number density at $T = 201\ MeV$, signaling the presence of a branch cut. The bottom picture shows the free energy at $T = 201\ MeV$ as a function of $\hat{\mu}_{B,I}$, computed by integrating the Padé approximant of the number density.

5.3 Case study 2 - chiral singularities

By lowering the temperature we also have found a preliminary signal of a so-called chiral singularity [57, 58]. For small light quark masses, the critical behaviour of the order parameter M is described by the magnetic equation

$$M = h^{\frac{1}{\beta\delta}}\ f_G(z)\ .$$

The expression is given in terms of the scaling variable $z = t\ h^{-\frac{1}{\beta\delta}}$, where

$$\begin{cases} t = \frac{1}{t_0}\left(\frac{T-T_c}{T_c} + k_B\hat{\mu}_B^2\right) \\ h = \frac{1}{h_0}\frac{m_l}{m_s}\ . \end{cases}$$

Here T_c and k_B are the chiral pseudocritical temperature and the curvature coefficient of the pseudocritical transition line, t_0 and h_0 are normalization constants, while $f_G(z)$, β and δ are respectively the univeral scaling function and the critical exponents of the $O(N)$ universality class. The function $f_G(z)$ has a pole z_c in the complex plane. This is known as Lee-Yang edge singularity and can be mapped to the $(T, \hat{\mu}_B)$ plane by

$$z_c = z \equiv z_0 \left(\frac{T - T_c}{T_c} + k_B \hat{\mu}_B^2 \right) \left(\frac{m_l}{m_s} \right)^{-\frac{1}{\beta\delta}} \quad .$$

The mapping requires the knowledge of both the universal parameters β, δ and the non-universal parameters z_0, T_c, k_B. The parameter z_c was determined by ref. [58] as $z_c = |z_c| e^{\frac{i\pi}{\beta\delta}}$ with $|z_c| = 2.032(21)$. Using the determinations carried out by the HotQCD collaboration for the non-universal parameters, one can estimate the location of the Lee-Yang edge singularity (which we refer to as chiral singularity). This is illustrated in fig. 5.8.

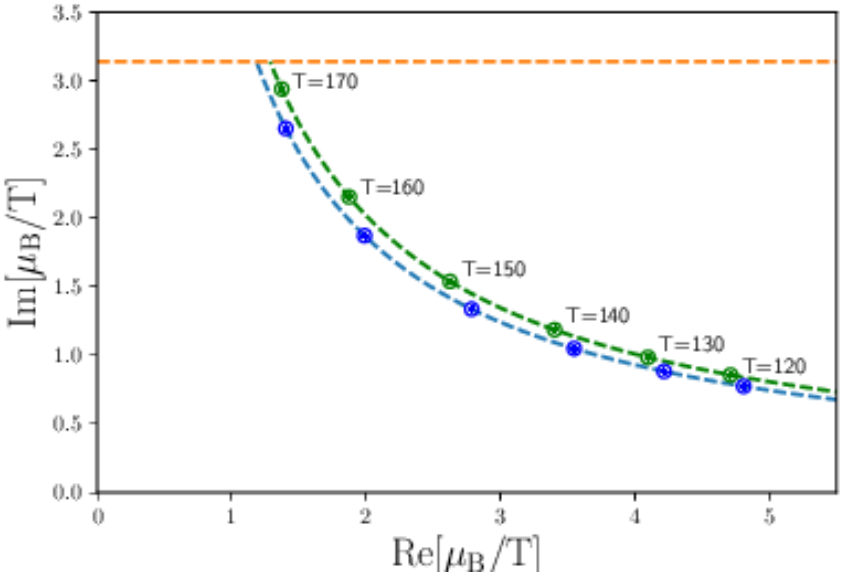

Figure 5.8: QCD at imaginary μ: Lee-Yang edge (chiral) singularity as a function of T. The blue and green data are given respectively for $N_t = 4, 6$. Image from ref. [59].

The figure shows the location of the Lee-Yang edge (chiral) singularity as a function of the temperature. The green and blue data correspond respectively to the estimates for $N_t = 4, 6$.

We explored the temperature $T = 145\ MeV$ using $N_s^3 \times N_t = 36^3 \times 6$ lattices. We performed lattice simulations at $O(10)$ imaginary chemical potentials. The lines of constant physics and the list of chemical potentials used in the simulations are summarized in tab. 5.4 and tab. 5.3. A total of ≈ 5000 gauge configurations have been generated and 520 random vectors were used for the measurements.

$\mu_{l,I}$ ($\beta = 6.038$)
0.00000
0.02182
0.04363
0.06545
0.08727
0.10908
0.13090
0.15272
0.16362
0.17453

Table 5.3: List of chemical potentials ($N_t = 6$).

β	m_l	m_s
6.038	0.0040	0.1082

Table 5.4: Lines of constant physics ($N_t = 6$).

5.3.1 Numerical results

We have proceeded in pretty much the same way we did to study thermal singularities. We have computed the Taylor coefficients of the baryon number density (up to $1st$ order, due to limited statistics) by lattice simulations at imaginary μ. Afterwards, we fitted these data using rational function ansatze.

The numerical results obtained for χ_B^1 are displayed in fig. 5.9 (top). The blue error bars denote the data from the simulations, while the blue solid line is the result from the Padé fit. The singularities we have determined from the fits are shown as blue error bars in fig. 5.10 (top). Their location is found to be consistent with the estimate illustrated in fig. 5.8. The thermal singularities already shown in fig. 5.6 are also drawn as error bars using warm colors. All in all the top picture of fig. 5.10 summarizes our current knowledge of the singularities (both thermal and chiral) of QCD in the complex μ_B plane.

Of course Padé interpolants are not only useful in locating the singularities in the complex plane. They also provide access to an analytic continuation for the observable. In fig. 5.9 (bottom) we show the analytic continuation of χ_B^1 to real chemical potentials. The real and imaginary parts of χ_B^1 are drawn respectively in blue and red. Up to $\hat{\mu}_B \approx 1.00 \div 1.25$ the analytical continuation appears to be under control and we get a vanishing imaginary part.

From the analytic continuation of χ_B^1 one can also calculate the cumulants ratio

$$R_B^{12} \equiv \frac{\chi_B^1}{\chi_B^2} \ .$$

This allows a comparison with some results previously obtained by the Taylor expansion (at $\mu_B = 0$) approach. In this latter approach the ratio R_B^{12} is expressed as a Taylor series $R_B^{12} = a_0\hat{\mu}_B + b_0\hat{\mu}_B^3 + c_0\hat{\mu}_B^5 + \ldots$, where the coefficients $a_0, b_0, c_0, \ldots$ are calculated by lattice simulations at zero chemical potential. The result for R_B^{12} obtained from the Padé interpolant is shown in fig. 5.10 (bottom) as a blue band.

This is to be compared with the results obtained by Taylor expansion at leading (cyan band), next-to-leading (green band) and next-to-next-to-leading (purple band) orders [60]. The results from the two approaches become progressively more in agreement as more terms are added to the Taylor series.

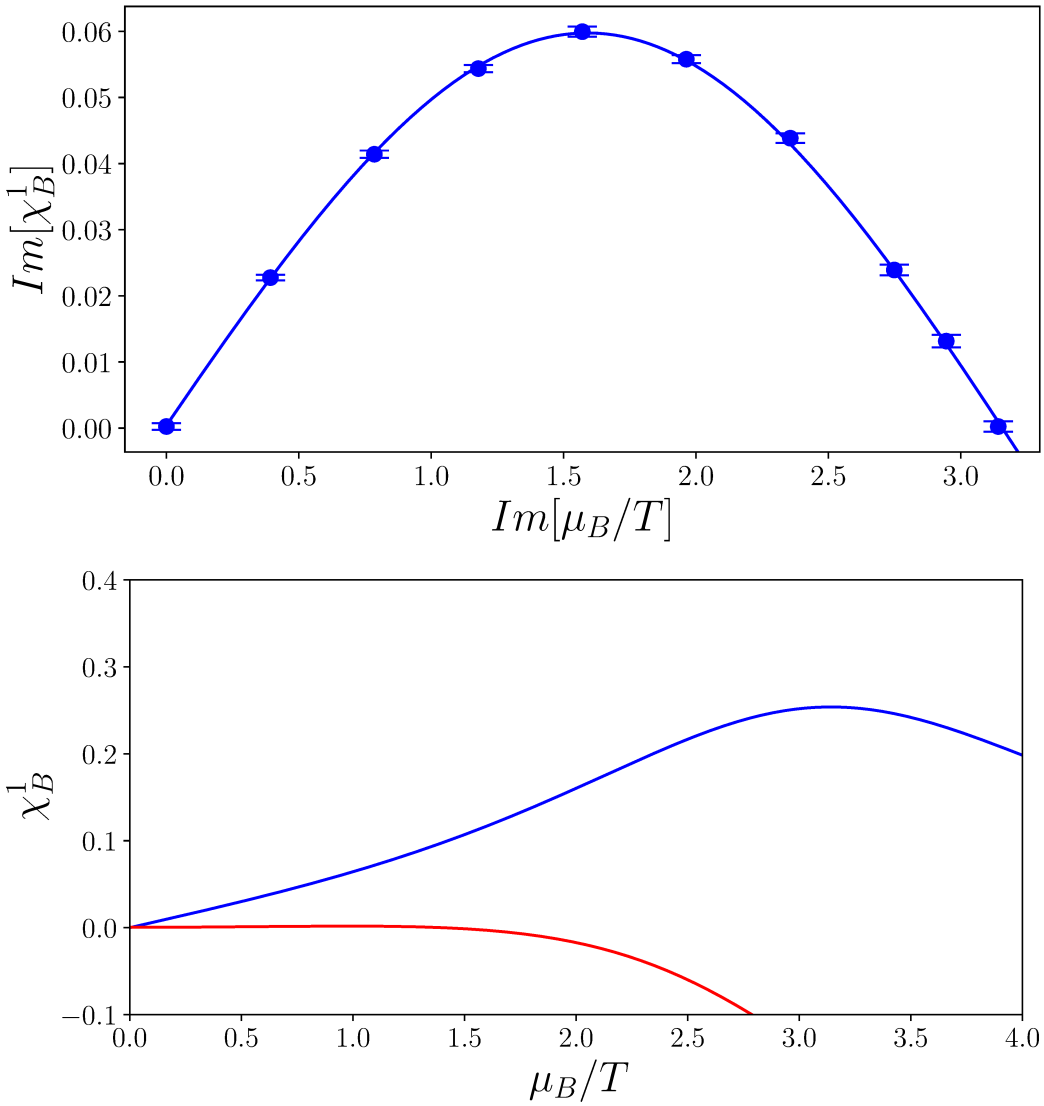

Figure 5.9: QCD at imaginary μ: imaginary part of χ_B^1 as a function of the chemical potential (top figure) and analytic continuation of χ_B^1 to real chemical potentials (bottom figure, real and imaginary parts drawn respectively in blue and red). Parameters used are $N_s^3 \times N_t = 36^3 \times 6$, $\beta = 6.038$ (which corresponds to $T = 145\ MeV$), light and strange quark masses as summarized in tab. 5.4.

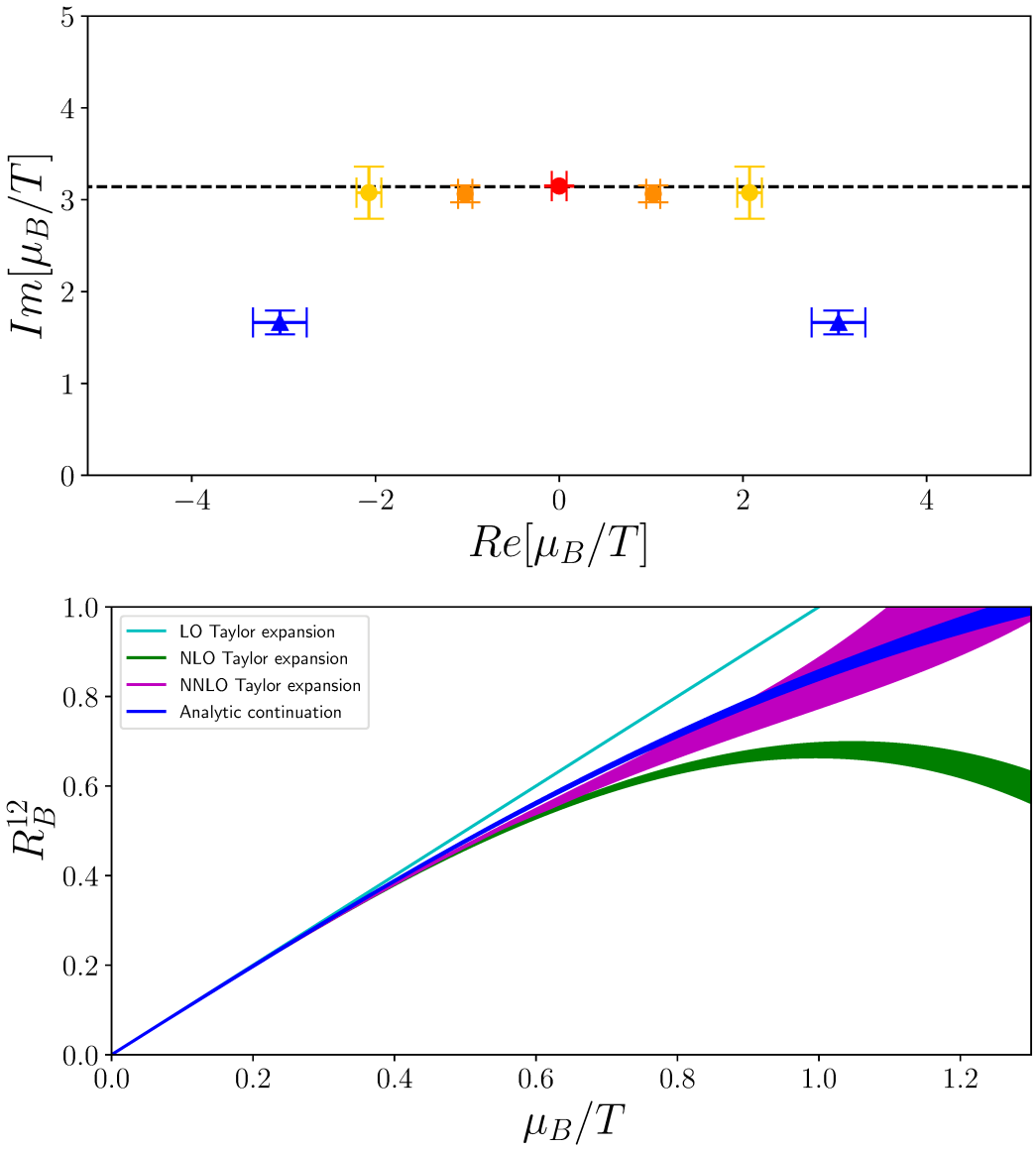

Figure 5.10: QCD at imaginary μ: singularities in the complex plane resulting from the Padé fit of the Taylor coefficients for χ_B^1 (top figure). The blue error bars denote the chiral singularity seen at $T = 145\ MeV$. Drawn in warm colors are the error bars denoting the thermal singularities seen at $T = 160\ MeV$, $176\ MeV$ and $201\ MeV$. The bottom figure shows the cumulants ratio R_B^{12} resulting from the analytic continuation of the Padé interpolant (blue) compared with the results obtained from the Taylor expansion (at $\mu_B = 0$) approach at leading (cyan), next-to-leading (green), next-to-next-to-leading (purple) orders.

5.4 Future prospects

In this chapter we have seen that Padé approximants are a powerful tool that can be used to investigate the phase diagram of QCD at imaginary chemical potentials. Specifically, they can be instrumental in determining the location of critical points. At $160\ MeV \leq T \leq 201\ MeV$ we have recognized the so-called thermal singularities. We have located the RW critical point (for $N_t = 4$) and we have been able to track how the singularity moves in the complex plane as the temperature is varied.

Moreover, by lowering the temperature we have also found a very preliminary signal of other singularities in the complex plane. At $T = 145\ MeV$ we have identified what appears to be an example of a so-called chiral singularity. While we only have a very rough estimate for it, the region where this is found is consistent with a result coming from a completely different approach [57, 58].

As one keeps lowering the temperature, this singularity is expected to eventually pinch the real axis signaling the location of the critical endpoint of the transition line in the $(T, \hat{\mu}_B)$ phase diagram of QCD. Of course this is true provided that the critical endpoint does exist. Validating this scenario is an exciting task; we have no guarantee of a success but we are confident our approach can prove to be an effective one.

It goes without saying that this method gives a natural access to analytic continuation: the Padé approximants can be evaluated for real values of the chemical potential. Preliminary work has shown that we have a quite good control of systematics. Not only the parity properties of the signal are correct, but we also find a vanishing imaginary part. We stress that the latter property is not trivial. In particular the region where the analytic continuation is reliable is recognized as that in which the imaginary part is zero to a good accuracy (where good means as low as 10^{-2} relative to the real part).

Chapter 6

Conclusions

A detailed knowledge of the QCD phase diagram is key to understand a wide range of physical phenomena, from heavy-ion collisions to neutron stars or even the evolution of the early Universe. As such investigating the QCD phase diagram is one of the major goals of lattice QCD. Despite this, large part of the phase diagram remains elusive because of the infamous sign problem.

A few years ago thimble regularization was proposed as a possible solution to the sign problem. After complexifying the degrees of freedom of a theory, one can define a set of manifolds attached to the critical points of the theory which are called Lefschetz thimbles. Lefschetz thimbles are a basis for the original domain of integration, in the sense that the original integrals can be decomposed into a linear combination of integrals over the thimbles. Most importantly the imaginary part of the action stays constant on each thimble, therefore each integral in the decomposition is free of the sign problem.

Indeed the approach is elegant, but it's fair to say that we have to confront challenges. We know from many counter-examples that in general more than one thimble is expected to give a relevant contribution in the thimble decomposition. The main challenge in multi-thimble simulations remains the calculation of the relative weights of the thimble contributions appearing in the decomposition.

In this work we explored two ways to calculate such weights. In the first method the weights are determined by computing the corrections to the Gaussian weights. We applied this method to the simplest version of heavy-dense QCD. We have shown that this theory is yet another example of a theory where the one-thimble approximation does not hold and we have shown that the method allows to take into account the sub-dominant thimble. In the second method one uses a few selected observables as normalization points. Specifically, the weights are calculated by imposing that the sum of the contributions from the relevant thimbles gives the correct results for these observables. The correct results can be known, for instance, from experimental measurements or from analytical solutions. Though predictive power is lost for these observables, it remains intact for any other observable. We applied this method to the one-dimensional Thirring model: while it has been known for a while that in this theory the one-thimble approximation fails in some regimes, how to collect the contribution from thimbles other than the dominant one was still an open question.

In this work we also explored a different, possibly more powerful approach to multi-thimble simulations. We have shown that it is possible to by-pass the need for them by exploiting the richness of the thimble structure. If multiple *good* regions in the parameters space of the theory can be found where the one-thimble approxima-

tion works, observables can be Taylor expanded around different points. The Taylor coefficients of these expansions can be calculated by one-thimble simulations. The Taylor expansions calculated at different points can then be used to bridge the *good* regions and reach other regions. Padé approximants are a powerful tool to carry out this procedure. We applied this method to both the one-dimensional Thirring model and to heavy-dense QCD. In both cases this approach not only allowed to reach by one-thimble simulations regions where the one-thimble approximation does not hold, but it also allowed to extract some information about the analytical structure of the observables. Specifically, the location of the true singularities of the observables are well matched by the poles of the Padé approximants.

Inspired by this success, we carried out some preliminary work on the QCD phase diagram at imaginary μ_B. By a Padé interpolation of the Taylor coefficients calculated at different values of the imaginary chemical potential, we were able to determine, at different temperatures, a few singularities in the complex μ_B plane. First of all, we were able to recognise the so called thermal singularities. Not only we located the RW singularity; we could also follow how the singularity moves around in the complex plane as the temperature is decreased: we found results which are fully consistent with the theoretical expectations. We also found a very preliminary signal of a so-called chiral singularity, which is roughly consistent with what has been estimated in a completely different approach. Hopefully, as we lower the temperature, we should be able to see these singularities eventually pinching the real axis, giving an estimate for the location of the critical endpoint of QCD.

A maybe less exciting but very important feature of the method is the capability of performing an analytic continuation of results coming from imaginary chemical potential simulations directly from the Padé approximants. Preliminary results indicate that the quality of this analytical continuation can be quite good (correct parity properties and vanishing imaginary part are obtained).

Bibliography

[1] I. M. Barbour, S. E. Morrison, E. G. Klepfish, J. B. Kogut and M. P. Lombardo, "Results on finite density QCD," Nucl. Phys. B Proc. Suppl. **60** (1998), 220-234 doi:10.1016/S0920-5632(97)00484-2 [arXiv:hep-lat/9705042 [hep-lat]].

[2] Z. Fodor and S. D. Katz, "A New method to study lattice QCD at finite temperature and chemical potential," Phys. Lett. B **534** (2002), 87-92 doi:10.1016/S0370-2693(02)01583-6 [arXiv:hep-lat/0104001 [hep-lat]].

[3] C. R. Allton, S. Ejiri, S. J. Hands, O. Kaczmarek, F. Karsch, E. Laermann, C. Schmidt and L. Scorzato, "The QCD thermal phase transition in the presence of a small chemical potential," Phys. Rev. D **66** (2002), 074507 doi:10.1103/PhysRevD.66.074507 [arXiv:hep-lat/0204010 [hep-lat]].

[4] S. Ejiri, C. R. Allton, S. J. Hands, O. Kaczmarek, F. Karsch, E. Laermann and C. Schmidt, "Study of QCD thermodynamics at finite density by Taylor expansion," Prog. Theor. Phys. Suppl. **153** (2004), 118-126 doi:10.1143/PTPS.153.118 [arXiv:hep-lat/0312006 [hep-lat]].

[5] P. de Forcrand and O. Philipsen, "The QCD phase diagram for small densities from imaginary chemical potential," Nucl. Phys. B **642** (2002), 290-306 doi:10.1016/S0550-3213(02)00626-0 [arXiv:hep-lat/0205016 [hep-lat]].

[6] M. D'Elia and M. P. Lombardo, "Finite density QCD via imaginary chemical potential," Phys. Rev. D **67** (2003), 014505 doi:10.1103/PhysRevD.67.014505 [arXiv:hep-lat/0209146 [hep-lat]].

[7] C. Ratti, "QCD at non-zero density and phenomenology," PoS **LATTICE2018** (2019), 004 doi:10.22323/1.334.0004

[8] Z. Fodor, S. D. Katz and C. Schmidt, "The Density of states method at non-zero chemical potential," JHEP **03** (2007), 121 doi:10.1088/1126-6708/2007/03/121 [arXiv:hep-lat/0701022 [hep-lat]].

[9] A. Alexandru, M. Faber, I. Horvath and K. F. Liu, "Lattice QCD at finite density via a new canonical approach," Phys. Rev. D **72** (2005), 114513 doi:10.1103/PhysRevD.72.114513 [arXiv:hep-lat/0507020 [hep-lat]].

[10] G. Aarts and I. O. Stamatescu, "Stochastic quantization at finite chemical potential," JHEP **09** (2008), 018 doi:10.1088/1126-6708/2008/09/018 [arXiv:0807.1597 [hep-lat]].

[11] A. Alexandru, G. Basar, P. F. Bedaque and N. C. Warrington, "Complex Paths Around The Sign Problem," [arXiv:2007.05436 [hep-lat]].

[12] M. Cristoforetti *et al.* [AuroraScience], "New approach to the sign problem in quantum field theories: High density QCD on a Lefschetz thimble, Phys. Rev. D **86** (2012), 074506 doi:10.1103/PhysRevD.86.074506 [arXiv:1205.3996 [hep-lat]].

[13] H. Fujii, D. Honda, M. Kato, Y. Kikukawa, S. Komatsu and T. Sano, "Hybrid Monte Carlo on Lefschetz thimbles - A study of the residual sign problem," JHEP **10** (2013), 147 doi:10.1007/JHEP10(2013)147 [arXiv:1309.4371 [hep-lat]].

[14] E. Witten, "A New Look At The Path Integral Of Quantum Mechanics," [arXiv:1009.6032 [hep-th]].

[15] E. Witten, "Analytic Continuation Of Chern-Simons Theory," AMS/IP Stud. Adv. Math. **50** (2011), 347-446 [arXiv:1001.2933 [hep-th]].

[16] T. Aoyama, M. Hayakawa, T. Kinoshita and M. Nio, "Tenth-Order QED Contribution to the Electron g-2 and an Improved Value of the Fine Structure Constant," Phys. Rev. Lett. **109** (2012), 111807 doi:10.1103/PhysRevLett.109.111807 [arXiv:1205.5368 [hep-ph]].

[17] D. Hanneke, S. F. Hoogerheide and G. Gabrielse, "Cavity Control of a Single-Electron Quantum Cyclotron: Measuring the Electron Magnetic Moment," Phys. Rev. A **83** (2011), 052122 doi:10.1103/PhysRevA.83.052122 [arXiv:1009.4831 [physics.atom-ph]].

[18] K. G. Wilson, "Confinement of Quarks," doi:10.1103/PhysRevD.10.2445

[19] S. Durr, Z. Fodor, J. Frison, C. Hoelbling, R. Hoffmann, S. D. Katz, S. Krieg, T. Kurth, L. Lellouch and T. Lippert, *et al.* "Ab-Initio Determination of Light Hadron Masses," Science **322** (2008), 1224-1227 doi:10.1126/science.1163233 [arXiv:0906.3599 [hep-lat]].

[20] P. Cea, L. Cosmai and A. Papa, "Critical line of 2+1 flavor QCD: Toward the continuum limit," Phys. Rev. D **93** (2016) no.1, 014507 doi:10.1103/PhysRevD.93.014507 [arXiv:1508.07599 [hep-lat]].

[21] C. Bonati, M. D'Elia, M. Mariti, M. Mesiti, F. Negro and F. Sanfilippo, "Curvature of the chiral pseudocritical line in QCD: Continuum extrapolated results," Phys. Rev. D **92** (2015) no.5, 054503 doi:10.1103/PhysRevD.92.054503 [arXiv:1507.03571 [hep-lat]].

[22] C. Bonati, M. D'Elia, F. Negro, F. Sanfilippo and K. Zambello, "Curvature of the pseudocritical line in QCD: Taylor expansion matches analytic continuation," Phys. Rev. D **98** (2018) no.5, 054510 doi:10.1103/PhysRevD.98.054510 [arXiv:1805.02960 [hep-lat]].

[23] A. Bazavov *et al.* [HotQCD], "Chiral crossover in QCD at zero and non-zero chemical potentials," Phys. Lett. B **795** (2019), 15-21 doi:10.1016/j.physletb.2019.05.013 [arXiv:1812.08235 [hep-lat]].

[24] S. Borsanyi, Z. Fodor, J. N. Guenther, R. Kara, S. D. Katz, P. Parotto, A. Pasztor, C. Ratti and K. K. Szabo, "QCD Crossover at Finite Chemical Potential from Lattice Simulations," Phys. Rev. Lett. **125** (2020) no.5, 052001 doi:10.1103/PhysRevLett.125.052001 [arXiv:2002.02821 [hep-lat]].

[25] H. B. Nielsen and M. Ninomiya, "No Go Theorem for Regularizing Chiral Fermions," Phys. Lett. B **105** (1981), 219-223 doi:10.1016/0370-2693(81)91026-1

[26] L. Susskind, "Lattice Fermions," Phys. Rev. D **16** (1977), 3031-3039 doi:10.1103/PhysRevD.16.3031

[27] R. Frezzotti *et al.* [Alpha], "Lattice QCD with a chirally twisted mass term," JHEP **08** (2001), 058 [arXiv:hep-lat/0101001 [hep-lat]].

[28] D. B. Kaplan, "A Method for simulating chiral fermions on the lattice," Phys. Lett. B **288** (1992), 342-347 doi:10.1016/0370-2693(92)91112-M [arXiv:hep-lat/9206013 [hep-lat]].

[29] Y. Shamir, "Chiral fermions from lattice boundaries," Nucl. Phys. B **406** (1993), 90-106 doi:10.1016/0550-3213(93)90162-I [arXiv:hep-lat/9303005 [hep-lat]].

[30] C. Gattringer and C. Lang, "Quantum chromodynamics on the lattice: an introductory presentation", Springer, 2010.

[31] H. J. Rothe, "Lattice gauge theories: an introduction", World Scientific Publishing, 2005.

[32] C. Bernard, M. Golterman and Y. Shamir, "Observations on staggered fermions at non-zero lattice spacing", Phys. Rev. D **73**, 114511 (2006) [hep-lat/0604017].

[33] P. Hasenfratz and F. Karsch, "Chemical Potential on the Lattice," Phys. Lett. B **125** (1983), 308-310 doi:10.1016/0370-2693(83)91290-X

[34] J. M. Pawlowski, I. O. Stamatescu and C. Zielinski, "Simple QED- and QCD-like Models at Finite Density," Phys. Rev. D **92** (2015) no.1, 014508 doi:10.1103/PhysRevD.92.014508 [arXiv:1402.6042 [hep-lat]].

[35] M. Luscher, "Trivializing maps, the Wilson flow and the HMC algorithm," Commun. Math. Phys. **293** (2010), 899-919 doi:10.1007/s00220-009-0953-7 [arXiv:0907.5491 [hep-lat]].

[36] Y. Tanizaki, H. Nishimura and K. Kashiwa, "Evading the sign problem in the mean-field approximation through Lefschetz-thimble path integral," Phys. Rev. D **91** (2015) no.10, 101701 doi:10.1103/PhysRevD.91.101701 [arXiv:1504.02979 [hep-th]].

[37] F. Di Renzo and G. Eruzzi, "Thimble regularization at work: from toy models to chiral random matrix theories," Phys. Rev. D **92** (2015) no.8, 085030 doi:10.1103/PhysRevD.92.085030 [arXiv:1507.03858 [hep-lat]].

[38] W. H. Press, S. A. Teukolsky, W. T. Vetterling and B. P. Flannery, "Numerical Recipes in C: The Art of Scientific Computing. Second Edition," 1992.

[39] P. Bogacki and L. F. Shampine, "A 3(2) pair of RungeKutta formula", Applied Mathematics Letters, 2 (4): 321325 (1989) doi:10.1016/0893-9659(89)90079-7.

[40] M. Cè, C. Consonni, G. P. Engel and L. Giusti, "Testing the Witten-Veneziano mechanism with the Yang-Mills gradient flow on the lattice," PoS **LATTICE2014** (2014), 353 doi:10.22323/1.214.0353 [arXiv:1410.8358 [hep-lat]].

[41] F. Di Renzo and G. Eruzzi, "One-dimensional QCD in thimble regularization," Phys. Rev. D **97** (2018) no.1, 014503 doi:10.1103/PhysRevD.97.014503 [arXiv:1709.10468 [hep-lat]].

[42] H. Fujii, S. Kamata and Y. Kikukawa, "Monte Carlo study of Lefschetz thimble structure in one-dimensional Thirring model at finite density," JHEP **12** (2015), 125 [erratum: JHEP **09** (2016), 172] doi:10.1007/JHEP12(2015)125 [arXiv:1509.09141 [hep-lat]].

[43] H. Fujii, S. Kamata and Y. Kikukawa, "Lefschetz thimble structure in one-dimensional lattice Thirring model at finite density," JHEP **11** (2015), 078 [erratum: JHEP **02** (2016), 036] doi:10.1007/JHEP02(2016)036 [arXiv:1509.08176 [hep-lat]].

[44] A. Alexandru, G. Basar and P. Bedaque, "Monte Carlo algorithm for simulating fermions on Lefschetz thimbles," Phys. Rev. D **93** (2016) no.1, 014504 doi:10.1103/PhysRevD.93.014504 [arXiv:1510.03258 [hep-lat]].

[45] A. Alexandru, G. Basar, P. F. Bedaque, G. W. Ridgway and N. C. Warrington, "Sign problem and Monte Carlo calculations beyond Lefschetz thimbles," JHEP **05** (2016), 053 doi:10.1007/JHEP05(2016)053 [arXiv:1512.08764 [hep-lat]].

[46] S. Bluecher, J. M. Pawlowski, M. Scherzer, M. Schlosser, I. O. Stamatescu, S. Syrkowski and F. P. G. Ziegler, "Reweighting Lefschetz Thimbles," SciPost Phys. **5** (2018) no.5, 044 doi:10.21468/SciPostPhys.5.5.044 [arXiv:1803.08418 [hep-lat]].

[47] J. Langelage, M. Neuman and O. Philipsen, "Heavy dense QCD and nuclear matter from an effective lattice theory," JHEP **09** (2014), 131 doi:10.1007/JHEP09(2014)131 [arXiv:1403.4162 [hep-lat]].

[48] M. Fromm, J. Langelage, S. Lottini, M. Neuman and O. Philipsen, "Onset Transition to Cold Nuclear Matter from Lattice QCD with Heavy Quarks," Phys. Rev. Lett. **110** (2013) no.12, 122001 doi:10.1103/PhysRevLett.110.122001 [arXiv:1207.3005 [hep-lat]].

[49] M. Fromm, J. Langelage, S. Lottini and O. Philipsen, "The QCD deconfinement transition for heavy quarks and all baryon chemical potentials," JHEP **01** (2012), 042 doi:10.1007/JHEP01(2012)042 [arXiv:1111.4953 [hep-lat]].

[50] J. M. Pawlowski and C. Zielinski, "Thirring model at finite density in 0+1 dimensions with stochastic quantization: Crosscheck with an exact solution," Phys. Rev. D **87** (2013) no.9, 094503 doi:10.1103/PhysRevD.87.094503 [arXiv:1302.1622 [hep-lat]].

[51] EuroPLEx (European network for Particle physics, Lattice field theory and Extreme computing). `http://europlex.unipr.it`

[52] C. Bonati, M. D'Elia, M. Mariti, M. Mesiti, F. Negro and F. Sanfilippo, "Roberge-Weiss endpoint at the physical point of $N_f = 2 + 1$ QCD," Phys. Rev. D **93** (2016) no.7, 074504 doi:10.1103/PhysRevD.93.074504 [arXiv:1602.01426 [hep-lat]].

[53] J. Goswami, F. Karsch, A. Lahiri and C. Schmidt, "QCD phase diagram for finite imaginary chemical potential with HISQ fermions," PoS **LATTICE2018** (2018), 162 doi:10.22323/1.334.0162 [arXiv:1811.02494 [hep-lat]].

[54] A. Bazavov *et al.* [HotQCD], "Equation of state in (2+1)-flavor QCD," Phys. Rev. D **90** (2014), 094503 doi:10.1103/PhysRevD.90.094503 [arXiv:1407.6387 [hep-lat]].

[55] G. A. Almasi, B. Friman, K. Morita, P. M. Lo and K. Redlich, "Fourier coefficients of the net-baryon number density and chiral criticality," Phys. Rev. D **100** (2019) no.1, 016016 doi:10.1103/PhysRevD.100.016016 [arXiv:1805.04441 [hep-ph]].

[56] V. Skokov, K. Morita and B. Friman, "Mapping the phase diagram of strongly interacting matter," Phys. Rev. D **83** (2011), 071502 doi:10.1103/PhysRevD.83.071502 [arXiv:1008.4549 [hep-ph]].

[57] S. Mukherjee and V. Skokov, "Universality driven analytic structure of QCD crossover: radius of convergence in baryon chemical potential," [arXiv:1909.04639 [hep-ph]].

[58] A. Connelly, G. Johnson, F. Rennecke and V. Skokov, "Universal Location of the Yang-Lee Edge Singularity in $O(N)$ Theories," Phys. Rev. Lett. **125** (2020) no.19, 191602 doi:10.1103/PhysRevLett.125.191602 [arXiv:2006.12541 [cond-mat.stat-mech]].

[59] C. Schmidt, J. Goswami, G. Nicotra, F. Ziesché, P. Dimopoulos, F. Di Renzo, S. Singh and K. Zambello, "Net-baryon number fluctuations," [arXiv:2101.02254 [hep-lat]].

[60] A. Bazavov *et al.* [HotQCD], "Skewness and kurtosis of net baryon-number distributions at small values of the baryon chemical potential," Phys. Rev. D **96** (2017) no.7, 074510 doi:10.1103/PhysRevD.96.074510 [arXiv:1708.04897 [hep-lat]].